11

Betatrons

The betatron [D.W. Kerst, Phys. Rev. **58**, 841 (1940)] is a circular induction accelerator used for electron acceleration. The word betatron derives from the fact that high-energy electrons are often called β-particles. Like the linear induction accelerator, the betatron is the circuit equivalent of a step-up transformer. The main difference from the linear induction accelerator is that magnetic bending and focusing fields are added to confine electrons to circular orbits around the isolation core. The beam acts as a multi-turn secondary. A single-pulsed power modulator operating at a few kilovolts drives the input; the output beam energy may exceed 100 MeV. The maximum electron kinetic energy achieved by betatrons is about 300 MeV. The energy limit is determined in part by the practical size of pulsed magnets and in part by synchrotron radiation.

General principles of the betatron are introduced in Section 11.1. The similarities between the power circuits of the linear induction accelerator, the recirculating induction linear accelerator, and the betatron are emphasized. An expression is derived for the maximum energy from a betatron; neglecting radiation, the limit depends only on the properties of the ferromagnetic core.

Two areas of accelerator physics must be studied in detail in order to understand the betatron; the theory of particle orbits in a gradient-type magnetic field and properties of magnetic circuits. Regarding orbits, the simple theory of betatron oscillations introduced in Section 7.3 must be extended. The amplitude of transverse-orbit oscillations and conditions for constant main-orbit radius must be determined for highly relativistic particles in a slowly changing magnetic field. Section 11.2 treats main orbit equilibria. The main orbit in the betatron has a constant radius

during the acceleration cycle. The orbit exists when the well-known *betatron condition* is satisfied. The confinement properties of the system for nonideal orbits are subsequently discussed.

The derivations demonstrate two properties of orbits: (1) particles injected on a circular orbit inside or outside the main orbit approach the main orbit during acceleration and (2) the amplitude of transverse oscillations decreases during the acceleration cycle. Section 11.3 addresses the first effect, motion of the instantaneous circle. Section 11.5 discusses damping of relativistic betatron oscillations during acceleration. As an introduction, Section 11.4 reviews the properties of periodic particle motions under the influence of slowly changing forces. The laws governing reversible compressions, both for nonrelativistic and relativistic particles, are discussed. The results are applicable to a wide variety of accelerators and particle confinement devices. Section 11.6 covers injection and extraction of electrons from the machine.

Section 11.7 surveys betatron magnet circuits, proceeding from simple low-energy devices to high-energy accelerators with optimal use of the core. The betatron magnet provides fields for particle acceleration, beam bending, and particle confinement. The magnet must be carefully designed in order to fulfill these functions simultaneously. Ferromagnetic materials are an integral part of all betatrons except the smallest laboratory devices. Thus, the available flux change is limited by the saturation properties of iron. Within these limits, the magnet circuit is designed to achieve the highest beam kinetic energy for a given stored modulator energy.

Even with good magnet design, existing betatrons are inefficient. Conventional betatrons rely on gradients of the bending field for focusing and utilize low-energy electron injection. The self-electric field of the beam limits the amount of charge that can be contained during the low-energy phase of the acceleration cycle. Usually, the beam current is much smaller than the driving circuit leakage current. Consequently, energy losses from hysteresis and eddy currents in the core are much larger than the net beam energy. Efficiency is increased by high beam current. Some strategies for high-current transport are discussed in Section 11.6. The two most promising options are (1) addition of supplemental focusing that is effective at low energy and (2) high-energy electron injection using a linear induction accelerator as a preaccelerator. In principle, betatrons can produce beam powers comparable to linear induction accelerators with a considerable reduction in isolation core mass.

11.1 PRINCIPLES OF THE BETATRON

Figure 11.1 illustrates the basic betatron geometry. A toroidal vacuum chamber encircles the core of a large magnet. The magnetic field is produced by pulsed coils; the magnetic flux inside the radius of the vacuum chamber changes with time. Increasing flux generates an azimuthal

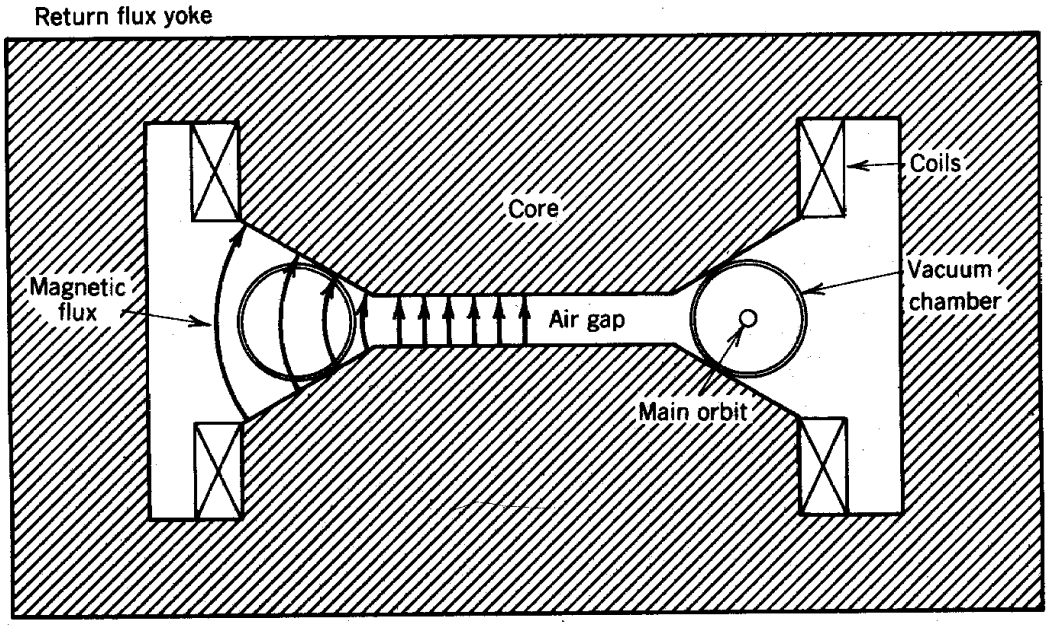

Figure 11.1 Schematic diagram of betatron with air gap.

electric field which accelerates electrons in the chamber.

In the absence of an air gap, there is little magnetic flux outside the core. An air gap is included to divert some of the magnetic flux into the vacuum chamber. By the proper choice of gap width, the vertical magnetic field can be adjusted to confine electrons to a circular orbit in the vacuum chamber. As shown in Figure 11.1, the confining field lines are curved. The resultant field has a positive field index. As we found in Section 7.3, the field can focus in both the horizontal and vertical directions.

In summary, the simple betatron of Figure 11.1 has the following elements:

1. A pulsed magnet circuit to accelerate electrons by inductive fields.

2. An air gap to force magnetic field into the beam transport region; electrons follow circular orbits in the bending field.

3. Shaped magnetic fields for beam focusing.

At first glance, the betatron appears quite different from the linear induction accelerator. Nonetheless, we can show that the power circuits of the two devices are similar. To begin, consider the induction accelerator illustrated in Figure 11.2a. The geometry is often called a *recirculating induction linac*. The transport tube is bent so that the beam passes through the same cavity a number of times. This allows higher beam kinetic energy for a given volt-second

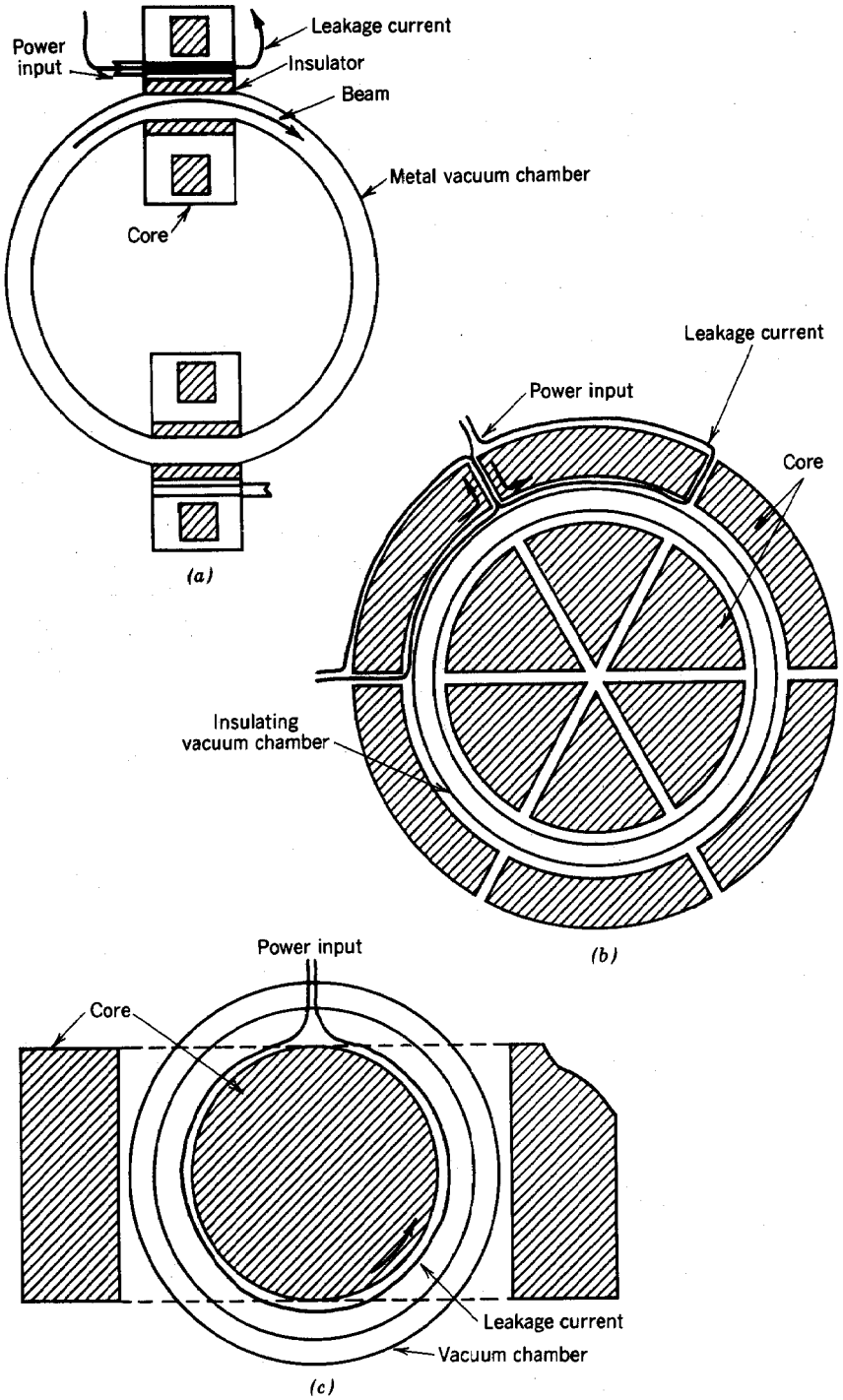

Figure 11.2 Equivalence between betatrons and linear induction accelerators. (*a*) Recirculating induction linac with two acceleration cavities. (*b*) Recirculating induction linac with isolation cores that fill the available area inside beam orbit. (*c*) Betatron with single core and single power feed point.

product of the isolation cores. The transport. tubes are made of metal; each cavity has separate vacuum insulators and high-voltage feeds. There are supplemental magnetic or electric forces to bend the orbits and keep particles confined in the tube.

To begin, we calculate the maximum electron kinetic energy possible in a recirculating induction linac with the following assumptions:

1. The beam tube has circumference $2\pi R$.
2. There are N cavities around the circumference; each cavity has an isolation core with cross-sectional area A_c.
3.The accelerating waveform in a cavity is a square pulse with voltage V_0 and the pulselength t_p.
4.Over most of the acceleration cycle, electrons travel near the velocity of light.

During the acceleration cycle, the electrons make $ct_p/2\pi R$ revolutions and travel through $Nct_p/2\pi R$ cavities. The final kinetic energy is therefore

$$E_b = V_o t_p Nc/2\pi R \ (eV). \tag{11.1}$$

Equation (11.1) can be rewritten by expressing the volt-second product in terms of the core properties [Eq. (10.1)]:

$$E_b \leq 2B_s NA_c c/2\pi R. \tag{11.2}$$

For a given circumference, the highest energy is attained with the tightest packing of isolation cores around the beam tube. The packing limit is reached when the cores fill the area inside the beam, $NA_c = \pi R^2$. Making this substitution, we find that

$$E_b \leq 2B_s Rc/2. \tag{11.3}$$

An optimized recirculating induction accelerator with pie-shaped cores is shown in Figure 11.2b. In the figure, much of the structure has been removed and the vacuum insulators have been extended to produce a single nonconducting toroidal vacuum chamber. The final step is to recognize that the radial currents of the individual power feeds cancel out; we can replace the multiple voltage feeds with a single line that encircles the core. Power is supplied from a single-pulse modulator. The resulting geometry, the power circuit of the betatron, is shown in Figure 11.2c.

In summary, the main differences between the betatron and the linear induction accelerator are as follows:

1. The betatron has one pulse modulator; the induction accelerator has many.

2. The beam in an induction accelerator makes a single pass through the machine. The equivalent circuit is a transformer with a single-turn secondary and multiple parallel primary windings. In the betatron, the beam makes many revolutions around the core. The circuit representing this machine is a single primary with a multi-turn secondary.

3. Because of recirculation, average gradient is not a concern in the betatron. Therefore, low accelerating voltages and relatively long pulselengths (matched to the available volt-second product of the core) are used. The circuit of Figure 11.2c requires a slow voltage pulse because it has significantly higher inductance than the driving circuits of Fi re 11.2b.

4. Shaping of the voltage pulse shape is not important in the betatron. The beam is distributed uniformly around the transport tube; there is no need for longitudinal confinement. The betatron magnet is usually driven by a bipolar, harmonic voltage waveform that cycles the core between $-B_s$ and $+B_s$.

The slow acceleration cycle and small circuital voltage allow a number of options for construction of the transport tube. The tube may be composed of metal interrupted azimuthally by one or more insulating rings. It is also possible to use a metal chamber constructed of thin stainless steel; the wall resistance must be high enough to keep inductively driven return currents small.

Equation 11.3 is also applicable to the betatron. As an example of kinetic energy limits, take R = 1 m and B_s = 1.5 T. The maximum kinetic energy is less than 450 MeV. Equation (11.3) has an important implication for the scaling of betatron output energy. The beam energy increases linearly with the radius of the central core, while the volume of core and flux return yoke increase as R^3. Cost escalates rapidly with energy; this is one of the main reasons why betatrons are limited to moderate beam energy.

As a final topic, we shall consider why betatrons have little potential for ion acceleration. In the discussion, ion dynamics is treated nonrelativistically. Assume an ion of mass m_i is contained in a betatron with radius R; the emf around the core is V_0. The energy ions gain in a time interval Δt is eV_0 multiplied by the number of revolutions, or

$$dE_b' = (eV_0/2\pi R)\sqrt{2E_b'/m_i}\,\Delta t. \tag{11.4}$$

Equation (11.4) can be rearranged to give

$$dE_b'/E_b'^{1/2} = (V_0/2\pi R)\sqrt{2e^2/m_i}\,\Delta t. \tag{11.5}$$

Integrating Eq. (11.5) (with the assumption that the final ion energy E_b is much larger than the injection energy), we find that

$$\sqrt{E_b} \leq \sqrt{e/2m_i}\ (V_0 t_p/2\pi R)\ (eV). \tag{11.6}$$

Substituting for the volt-second product and assuming a core area πR^2, Eq. (11.6) can be rewritten

$$E_b \leq (2e/m_i)\ (B_s R/2)^2. \tag{11.7}$$

With the same magnet parameters as above (R = 1 m, B_s = 1.5 T), Eq. (11.7) implies that the maximum energy for deuterons is only 54 MeV. Comparing Eq. (11.7) to Eq. (11.3), we find that the ratio of maximum obtainable energies for ions compared to electrons is

$$E_b\ (ions)\ /\ E_b\ (electrons) = v_{if}\ /\ c, \tag{11/8}$$

where v_{if} is the final ion velocity. Equation (11.8) has a simple interpretation. During the same acceleration cycle, the nonrelativistic ions make fewer revolutions around the core than electrons and gain a correspondingly smaller energy.

11.2 EQUILIBRIUM OF THE MAIN BETATRON ORBIT

The magnitude of the magnetic field at the orbit radius of electrons in a betatron is determined by the shape of the magnet poles. The equilibrium orbit has the following properties: (1) the orbit is circular with a radius equal to that of the major radius R of the vacuum chamber and (2) the orbit is centered in the symmetry plane of the field with no vertical oscillations. This trajectory is called the *main orbit*. We will consider other possible orbits in terms of perturbations about the main orbit.

The vertical field at R is designated $B_z(R)$. Equation (3.38) implies that $B_z(R)$ and R are related by

$$R = \gamma m_e v_0/eB_z(R) = p_0/eB_z(R). \tag{11.9}$$

The quantity p_0 is the total momentum of particles on the main orbit. The magnetic field varies with time. The azimuthal electric field acting on electrons is

$$\int \boldsymbol{E}\cdot\boldsymbol{dl} = d\Phi/dt = 2\pi R E_0, \tag{11.10}$$

where Φ is the magnetic flux enclosed within the particle orbit. Particle motion on the main orbit is described by the following equations:

$$v_r = 0, \qquad dp_r/dt = 0,$$

$$v_z = 0, \qquad dp_z/dt = 0, \tag{11.11}$$

$$dp_\theta/dt = eE_\theta = (e/2\pi R)\, d\Phi/dt.$$

Equation (11.11) is obtained from Eq. (3.34) by setting $v_r = 0$. We assume that R does not vary in time; consequently, Eq. (11.11) can be integrated directly to give

$$p_\theta = e\,[\Phi(t) - \Phi(0)]/2\pi R = (e/2\pi R)\,\Delta\Phi. \tag{11.12}$$

Combining Eqs. (11.9) and (11.12),

$$B_z(R) = \Delta\Phi/2\pi R^2. \tag{11.13}$$

Equation (11.13) is the well-known *betatron condition*. The betatron pole piece is designed so that vertical field at the average beam radius is equal to one-half the flux change in the core divided by the area inside the particle orbit. The betatron condition has a simple interpretation for the machine illustrated in Figure 11.1. Electrons are injected at low energy when the orbital field and the flux in the core are near zero. The bending field and accelerating field are produced by the same coils, so that they are always proportional if there is no local saturation of the core iron. The main orbit has radius R throughout the acceleration cycle if the vertical field at R is

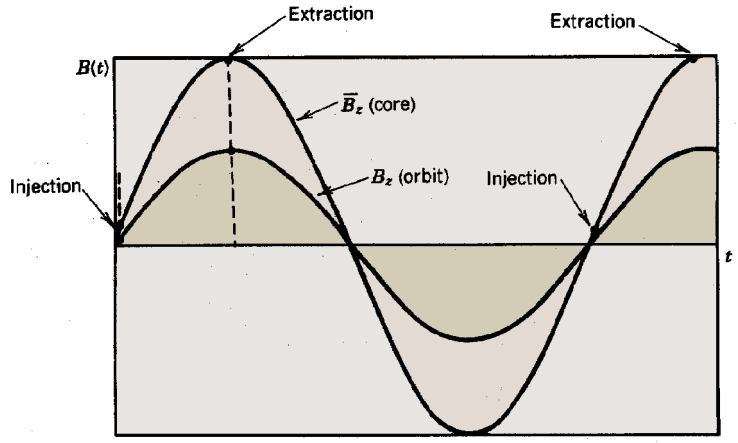

Figure 11.3 Acceleration cycle of air gap betatron; average magnetic field inside electron orbit and vertical magnetic field at main orbit as a function of time.

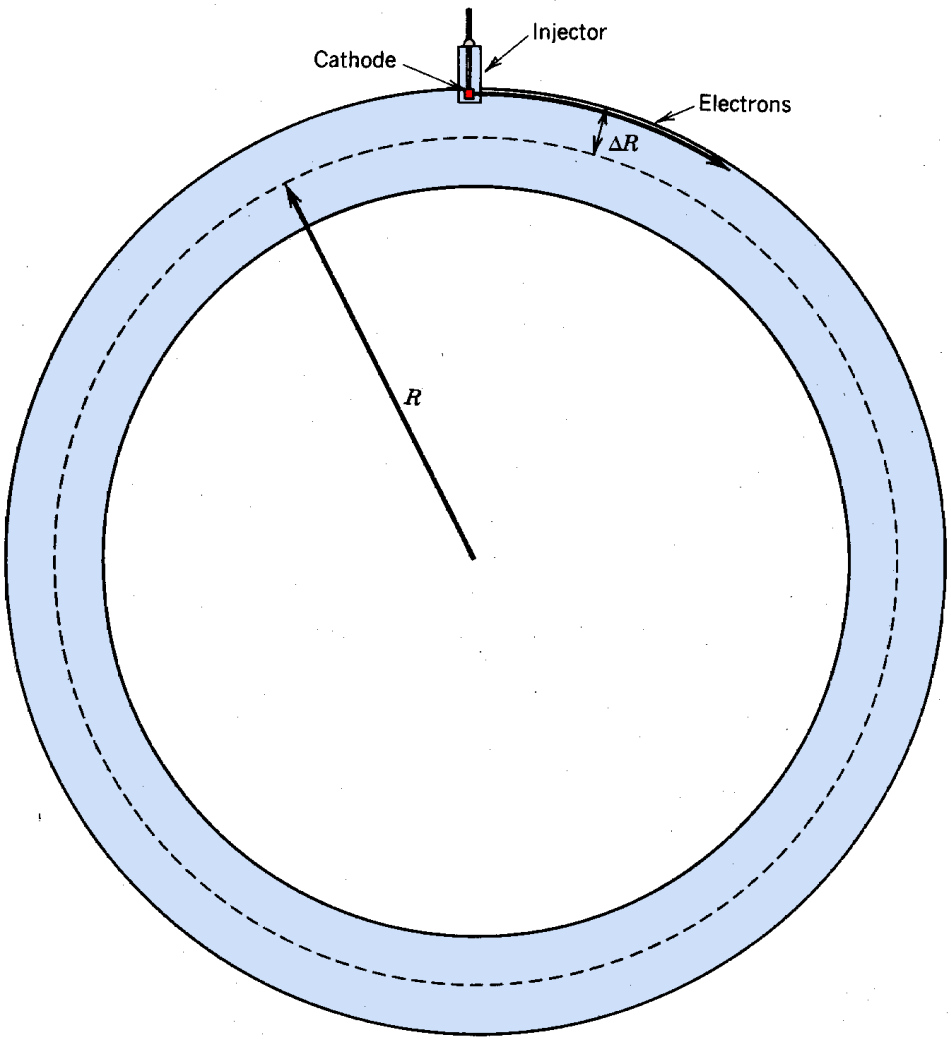

Figure 11.4 Injector geometry for low-current betatron.

equal to one-half the average field enclosed by the orbit. This condition holds both in the nonrelativistic and relativistic regimes. The acceleration cycle is illustrated in Figure 11.3.

11.3 MOTION OF THE INSTANTANEOUS CIRCLE

The standard electron injector of a betatron consists of a thermionic source at high dc voltage (20-120 kV) with extractor electrodes (Fig. 11.4). It is clear that such a device cannot extend to the main orbit. The injector is located at a radius inside or outside the main orbit and is displaced vertically from the symmetry plane. The extractor voltage is set so that the electrons have a circular orbit of radius $R+\Delta R$ in the magnetic field at injection. The betatron condition is not

satisfied on this orbit; therefore, the orbit radius changes during the acceleration cycle. We shall see that the orbit asymptotically approaches the main orbit as the electron energy increases. The circular orbit with slowly varying radius is referred to as the *instantaneous circle.*

Let p_0 be the momentum of a particle on the main orbit and p_1 be the momentum of a particle injected a distance ΔR from the main orbit on the instantaneous circle. At injection, the momenta and magnetic fields are related by

$$p_0(0) = eB_z(R)R, \qquad (11.14)$$

$$p_1(0) = p_0(0) + \delta p(0) = eB_z\,(R+\Delta R)\,(R+\Delta R). \qquad (11.15)$$

The time variation of flux enclosed within the instantaneous circle is

$$d\Phi_1/dt = 2\pi R^2\,[dB_z(R)/dt] + \int_R^{R+\Delta R} 2\pi r dr\,[dB_z(r)/dt]. \qquad (11.16)$$

Equation (11.13) has been used in the first term to express the magnetic flux in the region $0 < r < R$. Assume that field variations are small over the region near the main orbit so that $B_z(r) \cong B_z(R)$. To first order in Δr, Eq. (11.16) can be rewritten

$$d\Phi_1/dt \cong 2\pi R^2\,[dB_z(R)/dt] + 2\pi R\,\Delta R\,(dB_z/dt) = 2\pi Rr\,[dB_z(R)/dt]. \qquad (11.17)$$

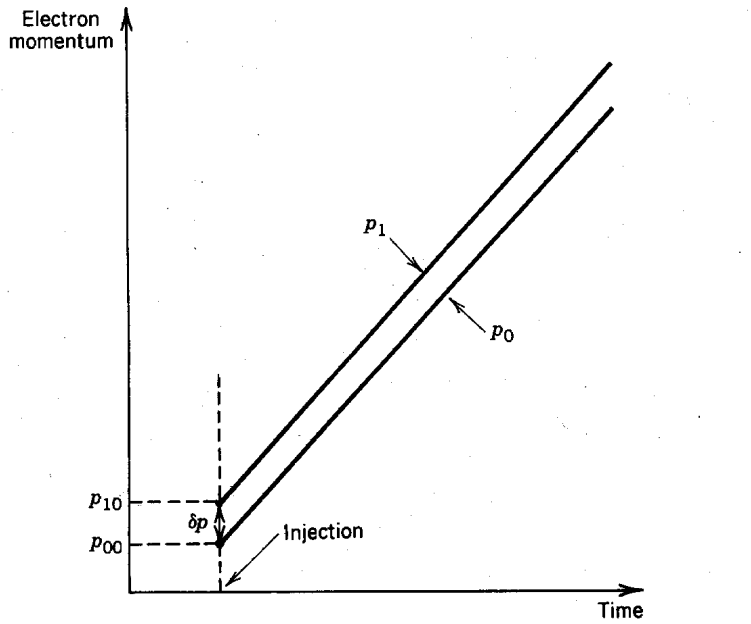

Figure 11.5 Time variation of momentum of electron on main orbit (p_0) and electron injected on instantaneous circle outside main orbit (p_1).

The equation of motion for an electron on the instantaneous circle is

$$dp_1/dt = (e/2\pi r)\ (d\Phi_1/dt) \cong eR\ [dB_z(R)/dt)]. \tag{11.18}$$

We recognize that the expression on the right-hand side is equal to dp_o/dt [Eq. (11.14)].

The main conclusion is that particles on the instantaneous circle gain momentum at the same rate as particles on the main orbit, as illustrated in Figure 11.5. The ratio of the radius of the instantaneous circle to that of the main orbit is equal to the relative momentum difference, or

$$\delta p/p_o \cong \Delta R/R. \tag{11.19}$$

The radius difference is proportional, to $1/p_o$ because δp is constant by Eq. (11.18). Therefore, the instantaneous circle approaches the main orbit as the electron energy increases.

11.4 REVERSIBLE COMPRESSION OF TRANSVERSE PARTICLE ORBITS

As we saw in Section 7.3, the focusing strength of magnetic field gradients is proportional to the magnitude of the bending field. In order to describe the betatron, the derivations of particle transport in continuous focusing systems must be extended to include time-varying focusing forces. As an introduction, we will consider the general properties of periodic orbits when the confining force varies slowly compared to the period of particle oscillations. The approximation of slow field variation is justified for the betatron; the transverse oscillation period is typically 10-20 ns while the acceleration cycle is on the order of 1 ms. The results are applicable to many beam transport systems.

To begin, consider the nonrelativistic transverse motion of a particle under the action of a force with a linear spatial variation. The magnitude of the force may change with time. The equation of motion is

$$d^2x/dt^2 = -\ [F(t)/mx_o]\ x = -\omega(t)^2\ x. \tag{11.20}$$

If the time scale for the force to change, ΔT, is long compared to $1/\omega$, then the solution of Eq. (11.20) looks like the graph of Figure 11.6. The relative change in ω over one period, $\Delta\omega$, is small:

$$\Delta\omega/\omega \ll 1. \tag{11.21}$$

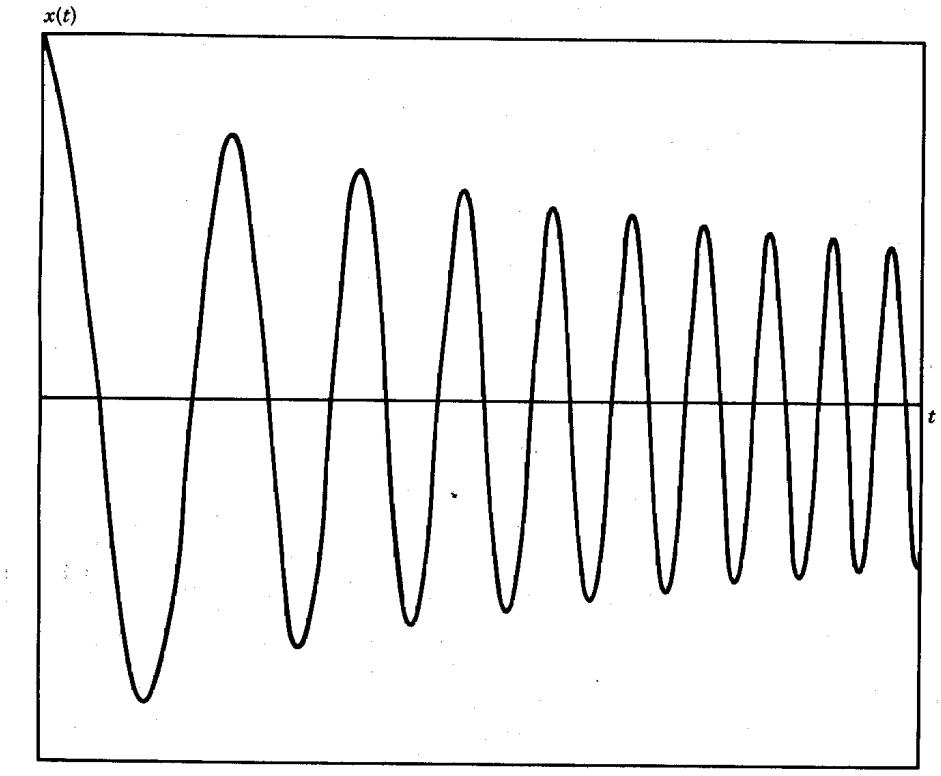

Figure 11.6 Time-dependent displacement of particle acted on by a focusing force that increases with time. Force varies linearly with x and increases a factor of 5 over time interval shown.

The condition of Eq. (11.21) can be rewritten in two alternate forms:

$$\frac{(d\omega/dt)\ (1/\omega)}{\omega} = \frac{d\omega/dt}{\omega^2} \ll 1, \qquad (11.12)$$

$$\frac{1}{\omega\ \Delta T} \ll 1. \qquad (11.23)$$

Equations (11.21)-(11.23) give the condition for a *reversible compression* (or *reversible expansion*). The meaning of reversible will be evident when we consider properties of the particle orbits.

Following Figure 11.6, an approximate solution to Eq. (11.20) should be oscillatory with a slow variation of amplitude. We assume a form

$$x(t) = A(t)\ \sin[\Phi(t)]. \qquad (11.24)$$

The quantities $A(t)$ and $\Phi(t)$ are determined by substituting Eq. (11.24) into Eq. (11.20) and dropping terms of order $(1/\omega\Delta T)^2$ or higher.

Calculating the derivatives and substituting,

$$x = (d^2A/dt^2)\sin\Phi + 2(dA/dt)(d\Phi/dt)\cos\Phi - A\sin\Phi(d\Phi/dt)^2 + A(d^\Phi/dt^2)\cos\Phi = -\omega^2\sin\Phi.$$

The solution must hold at all values of Φ. Therefore, the $\sin\Phi$ and $\cos\Phi$ terms must be individually equal, or

$$(d^2A/dt^2) - A\,(d\Phi/dt)^2 = -\omega^2\,A, \qquad (11.25)$$

$$2\,(dA/dt)\,(d\Phi/dt) + A\,(d^2\Phi/dt^2) = 0. \qquad (11.26)$$

The first term in Eq. (11.25) is of order $A/\Delta T^2$. This term is less than the expression on the right-hand side by a factor $(1/\omega\Delta T)^2$, so it can be neglected. Equation (11.25) becomes $d\Phi/dt = \omega$; therefore,

$$\Phi = \int \omega\, dt + \Phi_o. \qquad (11.27)$$

Substituting this expression in Eq. (11.26) gives

$$2\,(dA/dt)/A = -\,(d^2\Phi/dt^2)/(d\Phi/dt) \cong -\,(d\omega/dt)/\omega. \qquad (11.28)$$

Integrating both sides of Eq. (11.28),

$$\ln(\omega) = -2\,\ln(A) + const.$$

or

$$\omega\,A^2 = const. \qquad (11.29)$$

The approximate solution of Eq. (11.20) is

$$x(t) \cong A_o\,\sqrt{\omega_o/\omega}\,\sin\left(\int \omega\, dt + \Phi_o\right). \qquad (11.30)$$

Taking the derivative of Eq. (11.30), the particle velocity is

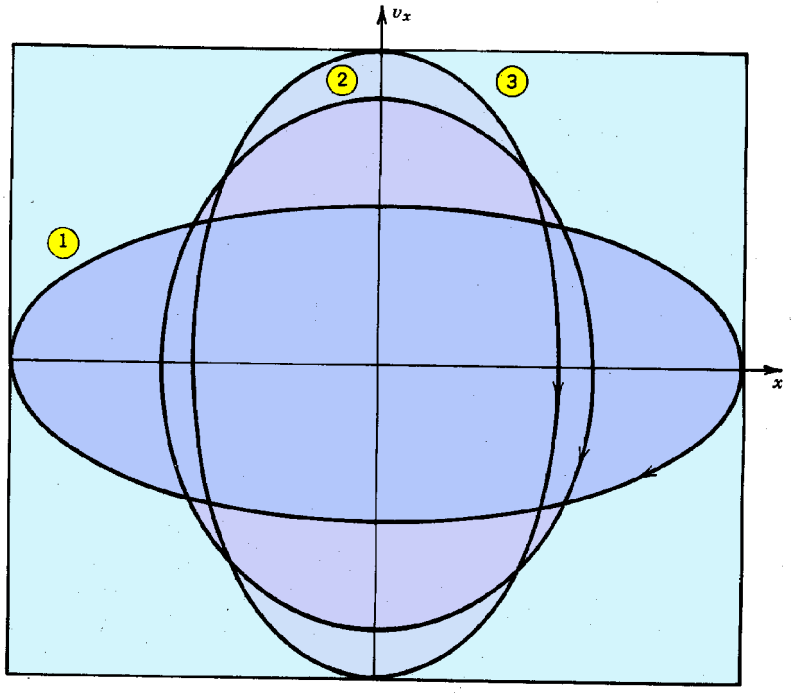

Figure 11.7 Variation of particle phase space orbits during reversible compression. (1) Initial orbit influenced by force that varies linearly with x. (2) Magnitude of force increased by a factor of 8. (3) Magnitude of force increased by a factor of 16.

$$x(t) \cong A_o \sqrt{\omega_o/\omega} \left[\cos\left(\int \omega \, dt + \Phi_o \right) - ((d\omega/dt)/2\omega^2) \sin\left(\int \omega \, dt + \Phi_o \right) \right] \cong A_o \sqrt{\omega_o/\omega} \cos\left(\int \omega \, dt + \Phi_o \right). \tag{11.31}$$

Hving solved the problem mathematically, let us consider the physical implications of the results.

1. At a particular time, the particle orbits approximate harmonic orbits with an angular frequency ω determined by the magnitude of the force. The amplitude and angular frequency of the oscillations changes slowly with time.

2. As the force increases, the amplitude of particle oscillations decreases, $x_{\max} \sim 1/\sqrt{\omega}$. This process is called compression of the orbit.

3. The particle velocity is approximately 90° out of phase with the displacement.

4. The magnitudes of the velocity and displacement are related by

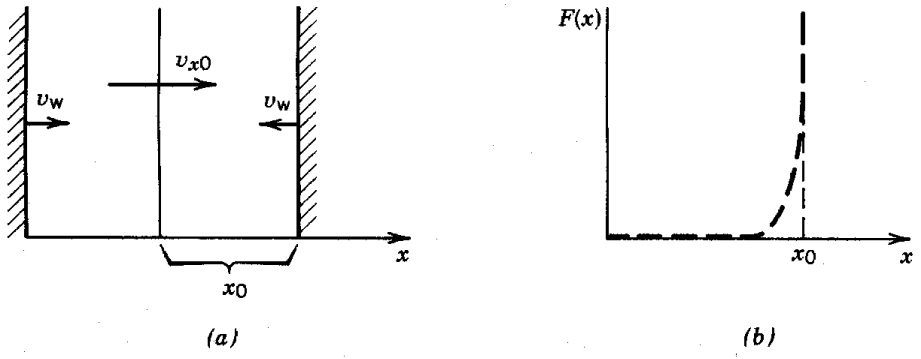

Figure 11.8 Particle confinement in a square well. (*a*) Geometry and coordinates, particle reflected elastically between two walls. (*b*) Variation of force with x.

5. The product of the displacement and velocity is conserved in a reversible process, or

$$x_{max}\ v_{x,max} \cong const. \tag{11.33}$$

Figure 11.7 gives a graphical interpretation of the above conclusions. Particle orbits are plotted in phase space with x and v_x as axes. Inspection of Eqs. (11.30) and (11.31) shows that particle

orbits acted on by a linear force are ellipses in phase space. Orbits are plotted in Figure 11.7 for a slow increase in focusing force (reversible compression). Although the oscillation amplitude changes, the net phase space area included within the orbit is constant. If the force slowly returns to its initial value, the particle orbit is restored to its original parameters; hence, the term reversible.

The properties of reversible compressions are not limited to linear forces but hold for confinement forces with any spatial variation. Consider, for instance, a particle contained by the square-well potential illustrated in Figure 11.8. The force is infinite at $x = x_o$ and $x = -x_o$. The particle has constant velocity v_{xo} except at the reflection points. The walls move inward or outward slowly compared to the time scale $x_o(t)/v_{xo}(t)$. In other words, the constant wall velocity v_w is small compared to $v_{xo}(t)$ at all times.

Particles reflect from the wall elastically. Conservation of momentum implies that the magnitude of v_{xo} is constant if the wall is stationary. If the wall moves inward at velocity v_w, the particle velocity after a collision is increased by an amount

$$\Delta v_{xo} = 2v_w. \tag{11.34}$$

In a time interval Δt, a particle collides with the walls $v_{xo}(t)\Delta t/2x_o(t)$ times. Averaging over many collisions, we can write the following differential equation:

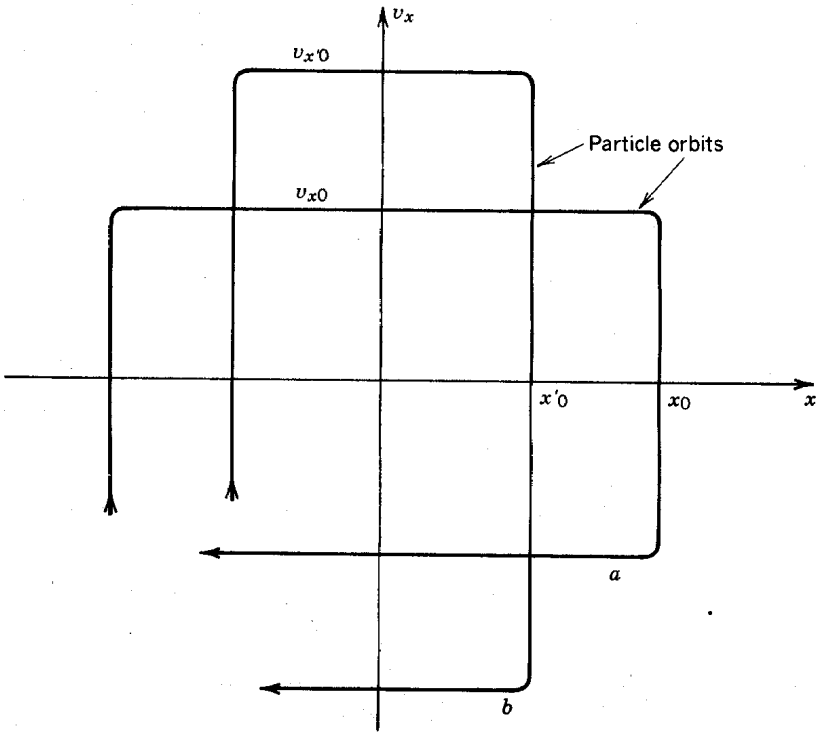

Figure 11.9 Phase space orbits of particles confined between two reflecting walls that move inward slowly. (*a*) Initial orbit. (*b*) Orbit with distance between walls decreased by a factor of 2.

$$dv_{xo}/dt \cong 2v_w v_{xo}(t)/2x_o(t). \tag{11.35}$$

The equation of the wall position is $x_o(t) = x_o(0) - v_x(t)t$, or

$$dx_o = -v_w dt. \tag{11.36}$$

Substituting into Eq. (11.35), we find $dv_{xo}/v_{xo} = -dx_o/x_o$, or

$$x_o(t)\ v_{xo}(t) \cong const. \tag{11.37}$$

This is the same result that we found for the harmonic potential. Similarly, defining the periodic frequency $\omega = v_{xo}(t)/x_o(t)$, Eq. (11.37) implies that

$$x_o \sim 1/\sqrt{\omega},$$

or

$$x_o^2\ \omega\ =\ const. \tag{11.38}$$

as before. A phase space plot of particle orbits in a highly nonlinear focusing system during a reversible compression is given in Figure 11.9.

11.5 BETATRON OSCILLATIONS

Reviewing the conclusions of Section 7.3, particles in a gradient magnetic field perform harmonic oscillations about the main orbit in the radial and vertical directions. The frequencies of oscillation are

$$\omega_r\ =\ \omega_g\ \sqrt{1-n}, \tag{11.39}$$

$$\omega_z\ =\ \omega_g\ \sqrt{n}, \tag{11.40}$$

where n is the field index and $\omega_g\ =\ eB_z(R)/\gamma m_e$. In the betatron, the magnitude of the magnetic field increases (ω_g is a function of time) while the relative shape remains constant (n is constant). The focusing force increases; therefore, the amplitude of oscillations in the radial and vertical directions decreases and particles move closer to the main orbit. This process is often called damping of betatron oscillations, although this is a misnomer. The process is reversible and no dissipation is involved.

The mathematical description of betatron oscillations is similar to that of Section 11.4 except that the variation of electron mass with energy must be taken into account for relativistically correct results. We shall consider motion in the vertical direction; the derivation for radial motion is a straightforward extension. With the assumption that $v_z\ \ll\ v_\theta$, the transverse approximation (Section 2.10) can be applied. This means that vertical motions do not influence the value of γ.

The vertical equation of motion for a linear force can be written

$$dp_z(t)/dt\ =\ d[m(t)v_z(t)]/dt\ =\ -m(t)\ \omega_z(t)^2\ z. \tag{11.41}$$

Expanding the time derivative, Eq. (11.41) becomes

$$(d^2z/dt)\ +\ (dm/dt)(dz/dt)/m\ +\ \omega_z^2\ z\ =\ 0. \tag{11.42}$$

Again, we seek a solution of the form

$$z = A(t)\ \sin\Phi_z(t). \tag{11.43}$$

Substituting in Eq. 11.42,

$$\begin{aligned}(\omega_z^2 - \Phi_z^2)\ A\ \sin\Phi_z + [A(d^2\Phi_z/dt^2) + 2(dA/dt)(d\Phi_z/dt) + A(dm/dt)(d\Phi_z/dt)/m]\ \cos\Phi_z \\ + [(d^2A/dt^2) + (dA/dt)(dm/dt)/m]\ \sin\Phi_z = 0.\end{aligned} \tag{11.44}$$

We can show by dimensional arguments that the third term of Eq. (11.44) is smaller than the first term by a factor of $(1/\omega\Delta T)^2$, where ΔT is the time scale of the acceleration cycle. Therefore, to first order, the first term is approximately equal to zero:

$$\omega_z^2 = (d\Phi_z/dt)^2. \tag{11.45}$$

Equation (11.45) gives the same result as the nonrelativistic derivation [Eq. (11.27)]:

$$\Phi_z = \int \omega_z dt + \phi_O. \tag{11.46}$$

Setting the second term equal to zero gives

$$A\ (d^2\Phi_z/dt^2) + 2\ (dA/dt)\ (d\Phi_z/dt) + A\ [(dm/dt)/m]\ \Phi_z = 0. \tag{11.47}$$

We can show that Eq. (11.47) is equivalent to

$$d(A^2 m\omega_z)/dt = 0,$$

or

$$A^2 m\omega_z = const. \tag{11.48}$$

There are some interesting implications associated with the above derivation. As before, the vertical displacements and velocity are 90° out of phase with magnitudes related by

$$v_{z,\max} \cong z_{\max}\ \omega_z = A\ \omega_z. \tag{11.49}$$

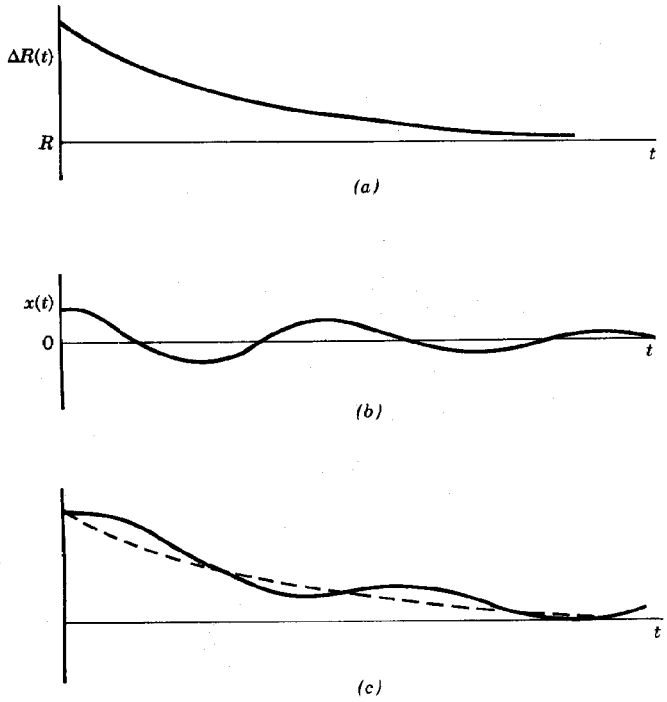

Figure 11.10 Schematic view of orbit of electron injected into low-current betatron. (*a*) Motion of instantaneous circle toward main orbit. (*b*) Reversibly compressed betatron oscillations. (*c*) Composite orbit.

The conservation law for a relativistic reversible compression is

$$m\ v_{z,\max}\ z_{\max} = z_{\max}\ p_{z,\max} = const. \tag{11.50}$$

For relativistic particles, the area circumscribed by an orbit is constant if it is plotted in phase space axes of displacement and momentum rather than displacement and velocity.

11.6 ELECTRON INJECTION AND EXTRACTION

Particle injection into linear accelerators is not difficult. In contrast, injection is a significant problem for circular accelerators, particularly those with constant beam radius such as the betatron. This is one of the reasons why high current electron beams have not yet been accelerated in betatrons. The conventional betatron electron source consists of a thermionic cathode located in the vacuum chamber (Fig. 11.4) capable of emitting 1-2 A current. The cathode is biased to high negative potential and electrons are extracted and focused by shaped electrodes. The emerging beam has a large spread in particle direction. The source is pulsed on for a few microseconds at the time when electrons will travel on an instantaneous circle orbit in

the rising bending magnetic field.

Following injection, the combined effects of inward motion of the instantaneous circle and damping of betatron oscillations carries electrons away from the injector so that some are trapped. The process is illustrated in Figure 11.10. Without such effects, the electrons would eventually strike the back of the injector. The fraction of electrons trapped is increased if the injector is
displaced vertically from the main orbit. Because of the vertical oscillations, particles may travel many revolutions before striking the injector, even in the absence of radial motion.

As an example, consider a 300-MeV betatron with main orbit radius of 1 m operating at 180 Hz. The rate of energy gain is about 7 keV/turn. If the injection energy is 100 keV and the initial instantaneous circle has radius 1.05 m, then Eq. (11.19) implies that the orbit moves radially inward a distance 0.24 cm in a single turn. If vertical oscillations allow the particles 5-10 turns,
this radial motion is sufficient to trap a substantial number of electrons.

The main limit on trapping in a high-energy betatron appears to result from beam space charge effects. Focusing is weak at injection because of the low applied magnetic field. In the example above, the injection field is only 10^{-3} T. Estimating the space charge force and specifying a balance with the vertical focusing force leads to a predicted equilibrium current of less than 1 A for a
beam with 4 cm vertical extent. This figure is consistent with the maximum current observed in betatrons. The dominant role of space charge in limiting injection current is consistent with the fact the trapped current increases significantly with increased injector voltage. The injection efficiency for high-energy betatrons with an internal, electrostatic injector is typically only a few percent.

Trapping mechanisms are not as easily explained in small, low-energy betatrons. In a machine with output energy of 20 MeV, motion of the instantaneous circle is predicted to be on the order of only 2×10^{-3} cm. Nonetheless, the trapped current is observed to be much higher than that predicted from single-particle orbit dynamics combined with the probability of missing the injector. The most widely accepted explanation is that collective particle effects are responsible for the enhanced trapping. There is a substantial inductance associated with the changes of beam

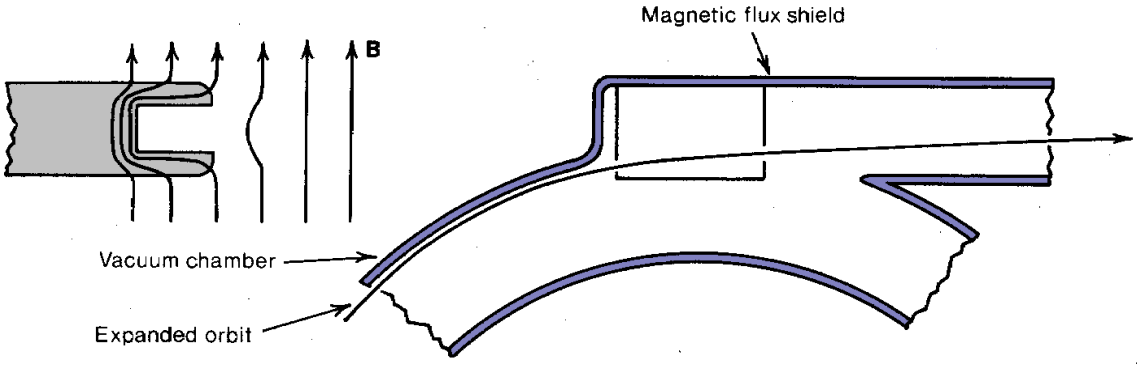

Figure 11.11 Extraction of low-current electron beam from betatron.

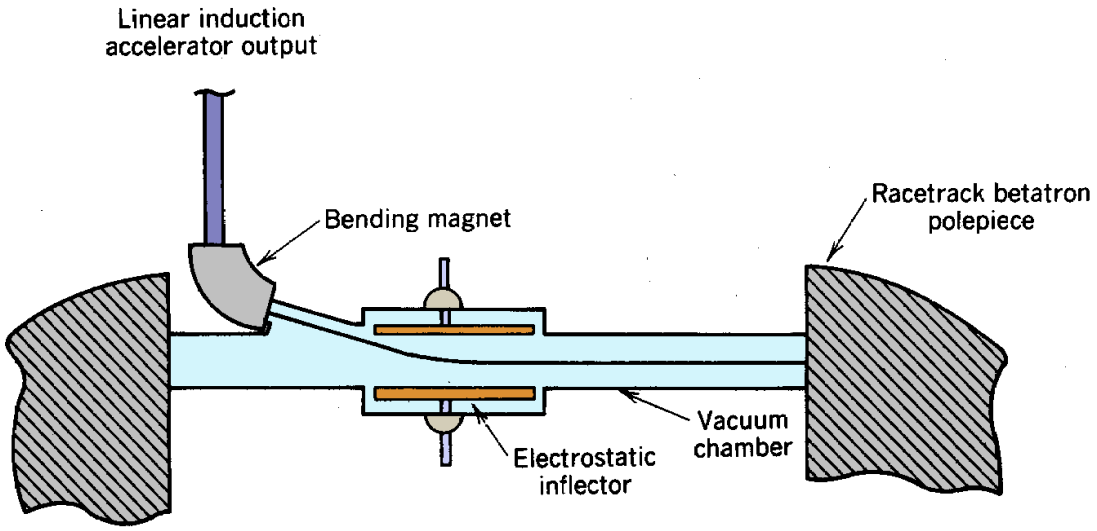

Figure 11.12 Injection of high-current electron beam from linear induction accelerator into racetrack betatron.

current around the ferromagnetic core. The increasing beam current during the injection pulses induces a back emf that is larger than the accelerating emf of the core. The inductive electric field decelerates electrons. The effect is almost independent of radius, so that particle orbits shrink toward the main orbit much more rapidly than predicted by the arguments of Section 11.3. This explanation is supported by the fact that trapping in low-energy betatrons is improved considerably when orbit contraction coils are incorporated in the machine. These rapidly pulsed coils enhance the self-field effects by inducing a back emf.

Extraction of electron beams from betatrons is accomplished with a magnetic peeler, illustrated in Figure 11.11. This device is a magnetic field shunt located on an azimuth outside the radius where $n = 1$. It cannot be located too close to the main orbit because the associated magnetic field perturbation would cause particle loss during the low-energy phase of the acceleration cycle. If particles are forced past the $n = 1$ radius, radial focusing is lost and they spiral outward into the peeler. There are a number of options for inducing radial motion of the betatron beam. One possibility is an orbit expander coil. The expander coil is activated at the peak of the electron energy. It subtracts from the bending field in the beam chamber, causing the beam radius to expand. Another method of moving electrons out in radius is to induce betatron oscillations by resonant fields. Electric or magnetic fields oscillating at $\sqrt{1-n}\ \omega_g$ are generated by coils or plates at particular azimuthal positions. If the growth of betatron oscillations is rapid, the beam spills out at a specific azimuth.

The maximum current that can be contained in a betatron is determined by a balance between the mutual repulsion between electrons and the focusing forces. In terms of space-charge equilibrium, the gradient focusing strength in a betatron at peak field (~ 1 T) is sufficient to contain a high-energy (- 300 MeV) electron beam with current in excess of 10 kA. A high-energy electron beam is stiff and largely confined by its own magnetic fields; therefore, an extension of conventional betatron extraction techniques would be sufficient to extract the beam from the machine. Containing the beam during the low-energy portion of the acceleration phase

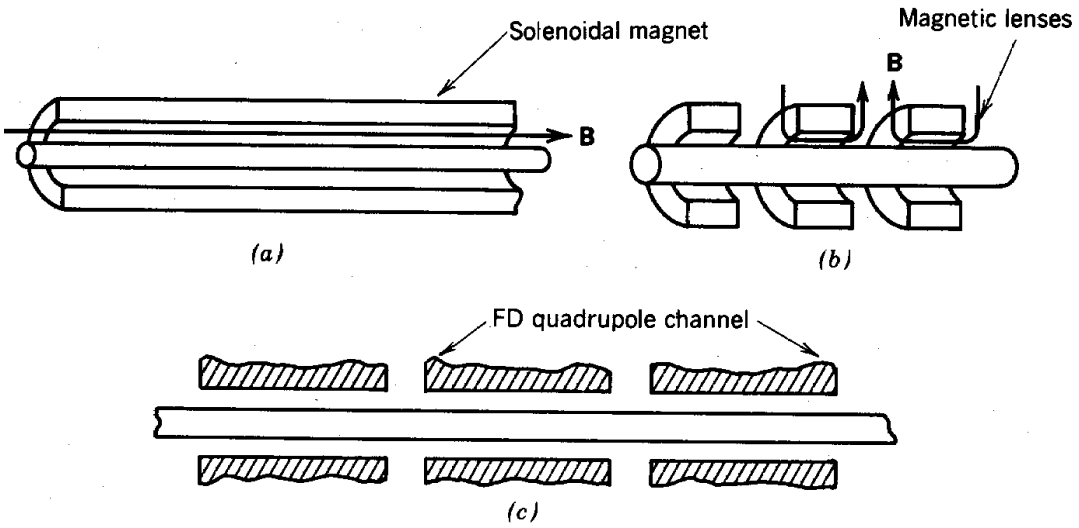

Figure 11.13 Methods to supplement focusing of low-energy electrons in betatron. (*a*) Magnet winding around vacuum chamber to produce uniform toroidal magnetic field. (*b*) Periodic array of magnetic lenses (with alternating field polarity) displaced around vacuum torus. (*c*) FD (or FODO) quadrupole lens array.

is the major impediment to a high-current, high-efficiency betatrons. Two methods appear feasible to improve the operation of betatrons: (1) high-energy injection and (2) addition of supplemental focusing devices.

In the first method, illustrated in Figure 11.12, a high-current, high-energy beam from a linear induction accelerator is injected in a single turn into the betatron. To facilitate injection, the betatron could be constructed in a racetrack configuration. The circular machine is split into two parts connected by straight sections. Injection and extraction are performed in the straight sections, which are free of bending fields. The betatron performs the final portion of the acceleration cycle (for example, from 100 to 300 MeV). The current limit in the betatron is high for two reasons: (1) the bending field and its gradients are large and (2) the self-magnetic field force of the relativistic beam almost balances the self-electric field repulsion so that space charge effects are of reduced importance. The beam is directed along the main orbit by a pulsed electrostatic inflector. The radial inflector field is activated only during a single transit of the beam around the accelerator; otherwise, it would deflect the trapped beam onto an exit orbit similar to the extrance orbit. The combination of induction linear accelerator and betatron is a good symbiosis for high-flux electron beams. The induction accelerator, with its strong solenoidal focusing magnets, solves the problem of injection and low-energy transport. The betatron provides the bulk of the particle acceleration. The combined accelerator would have a size and core volume much smaller than that of a 300-MeV linear induction accelerator.

A second approach to high-flux betatrons is to supplement gradient focusing with axi-centered focusing lenses arrayed around the toroidal vacuum chamber. Some options, illustrated in Figure 11.13, include (1) a bent solenoidal field (toroidal field), (2) discrete solenoidal magnetic lenses with reversing applied field direction, and (3) an array of magnetic quadrupole lenses in an

FD configuration. The study of alternate focusing methods in betatrons is an active area of research. There are some difficult technological problems to be solved. For instance, injection into a betatron with a strong toroidal field is considerably more difficult than injection into a standard geometry, even at low current. The main problem in any strong focusing betatron is the fact that
the beam must pass through the $\upsilon = 1$ condition (see Section 7.2). When the low-energy beam is injected, the strong space charge forces require strong supplementary focusing. Strong focusing implies that the betatron wavelength is less than the circumference of the machine; thus, $\upsilon > 1$ in both the radial and vertical directions. At the end of the acceleration cycle, gradient field focusing dominates. The orbits resemble those in a conventional betatron with $\upsilon < 1$. Passage through the resonance condition could be avoided by increasing the supplementary focusing fields with the bending fields and keeping $\upsilon > 1$. This is not technologically practical since the focusing system would require high energy input. Passage through the $\upsilon = 1$ condition may result in complete loss of the beam. There is a possibility that the severity of resonance instabilities could be reduced by a nonlinear focusing system, a fast acceleration cycle, or tuned electrostatic lenses that sweep the focusing system rapidly through the resonance condition.

11.7 BETATRON MAGNETS AND ACCELERATION CYCLES

The kinetic energy limit of betatrons is tied closely to the saturation properties of iron. Although air core betatrons have been operated successfully, they are impractical except for small research devices because of the large circulating energy and power losses involved. The volume of magnetic field outside the iron core should be minimized for the highest accelerator efficiency and lowest cost. With these factors in mind, we will review some of the types of betatron magnets that have been developed. The order will be roughly historical, proceeding from the simplest circuits at low energy to the highest energy attained.

An early betatron for electrons at 20 MeV is illustrated in Figure 11.1. The acceleration cycle is illustrated in Figure 11.3. The core flux and bending field are part of the same magnetic circuit; therefore, they are proportional to one another. A betatron driving circuit is illustrated in Figure 11.14. The inductance represents the betatron core and windings; a resistor has been included
to represent energy loss through winding resistivity, hysteresis, and eddy currents. The beam load is also indicated; at current typical of conventional betatrons, the impedance of the beam load is high. The beam current is much smaller than the leakage current. In order to keep the power consumed by the betatron at a reasonable level, the core inductor is often combined with a capacitor bank to form a resonant circuit. The leakage current is supported as reactive current in the resonant circuit; a fraction of the energy of the underdamped *LC* circuit is lost on each cycle to resistive losses and beam acceleration. The stored energy of the capacitor bank is topped up on each cycle by a driving circuit with high-power vacuum tubes.

The components of the resonant circuit fulfill the following conditions:

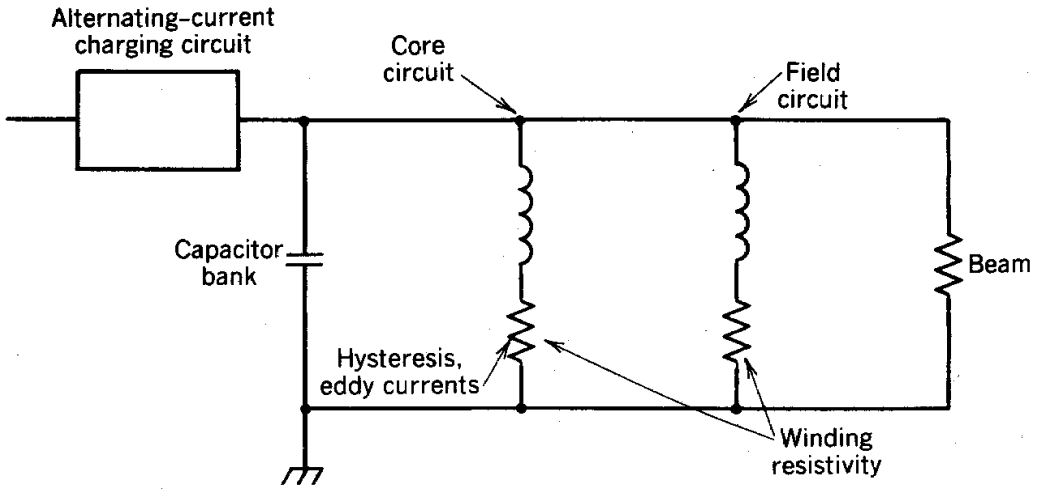

Figure 11.14 Alternating-current power circuit for a low-current betatron operated without core saturation.

1.The circuit has the desired resonant frequency, or

$$f = 2\pi / \sqrt{LC}.$$

Typically, betatrons operate at 180 Hz.

2.The stored energy in the capacitor bank, $\frac{1}{2}CV_0^2$, equals the total magnetic field energy at the peak of the acceleration cycle,

$$U_m = \int dx^3 \, (B^2/2\mu).$$

3. The ampere turns in the coil box are sufficient to produce the field in the air gap.

The above conditions can be combined to determine the capacitor bank voltage and number of turns in the coil box given the operating parameters of the betatron.

The betatron of Figure 11.1 has a major drawback for application to high-energy beams. Most of the energy in the drive circuit is utilized to produce magnetic flux in the central air gap. This translates into a large capacitor bank to store energy and increased resistive losses because of the high *NI* product of the coil. In order to extend the betatron to higher energy and keep power consumption low enough to run on a continuous basis, it is clearly advantageous to eliminate the air gap. One solution is illustrated in Figure 11.15a. The magnetic flux at the electron orbit is produced by a separate magnet circuit. The beam transport circuit has its own flux-guiding core and magnet windings. The size of the capacitor bank is reduced considerably, and power losses

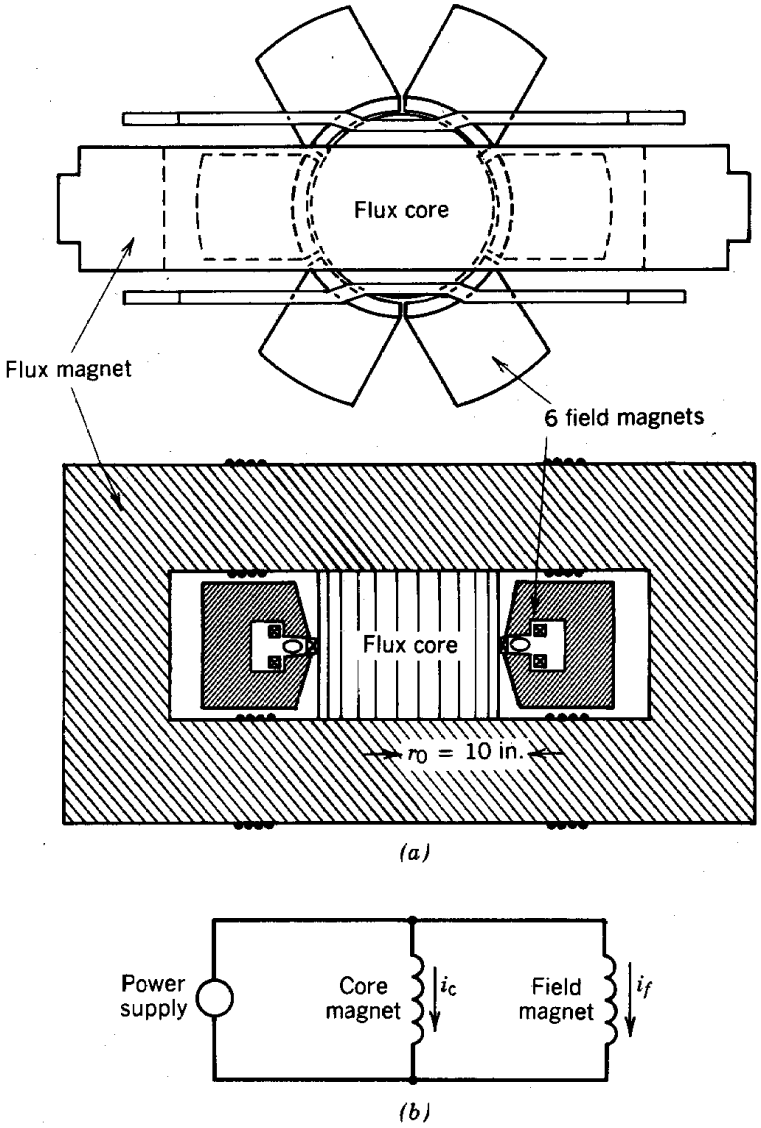

Figure 11.15 High-energy (80-MeV) betatron with no air gap. (*a*) Geometry of device, showing separate magnet circuits for accelerating flux and bending field. (*b*) Parallel drive of magnetic circuits guarantees proportionality of magnetic flux. (M. S. Livingston and J. P. Blewett, *Particle Accelerators*, used by permission, McGraw-Hill Book Co.)

are typically only one-third those that would occur with a single-magnet circuit. The disadvantage of the design is the increased complexity of assembly and increased volume of the main circuit core in order to accommodate the bending field circuit.

An interesting problem associated with the betatron of Figure 11.15a is how to drive the two magnetic circuits with close tracking between the transport fields and acceleration flux. An effective solution is to connect both magnets to the same power supply in parallel, as shown in Figure 11.15b. Because the voltage across the windings must be the same, the flux change

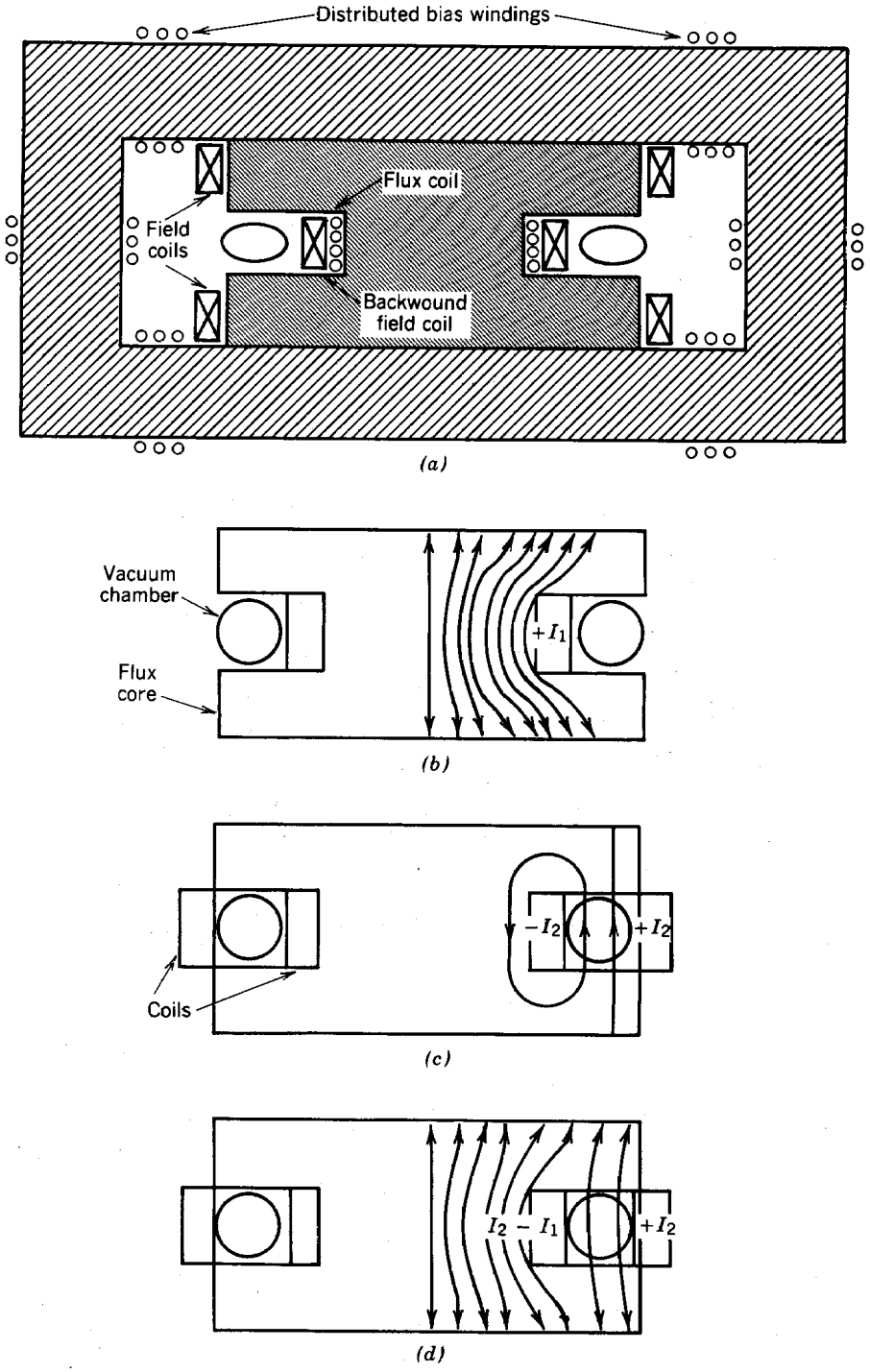

Figure 11.16 Betatron with single magnetic circuit, bias windings, and no air gap. (*b*) Magnetic field lines in flux core produced by flux winding. (*c*) Magnetic field lines in flux core and vacuum torus produced by combination of external field coil and backwound field coil. (*d*) Composite field lines showing accelerating flux and bending field.

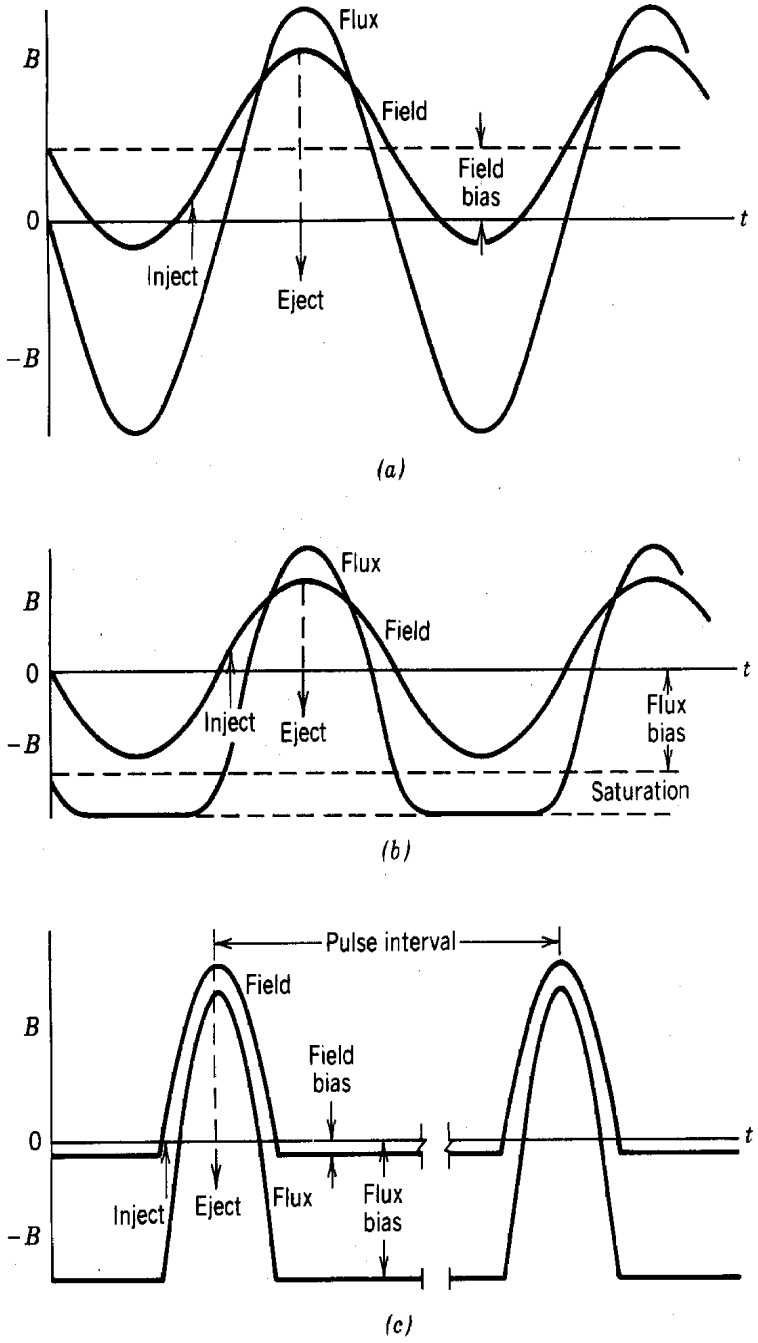

Figure 11.17 Acceleration cycles for high-energy betatrons. Average field inside main orbit and bending field at main orbit plotted versus time. (*a*) Cycle with field biasing, dc component added to bending field. (*b*) Cycle with flux biasing and ac power drive; flux core saturated half the time. (*c*) Cycle of betatron with flux biasing and pulsed power drive from a switched capacitor bank; core must be reset by a separate circuit between each pulse.

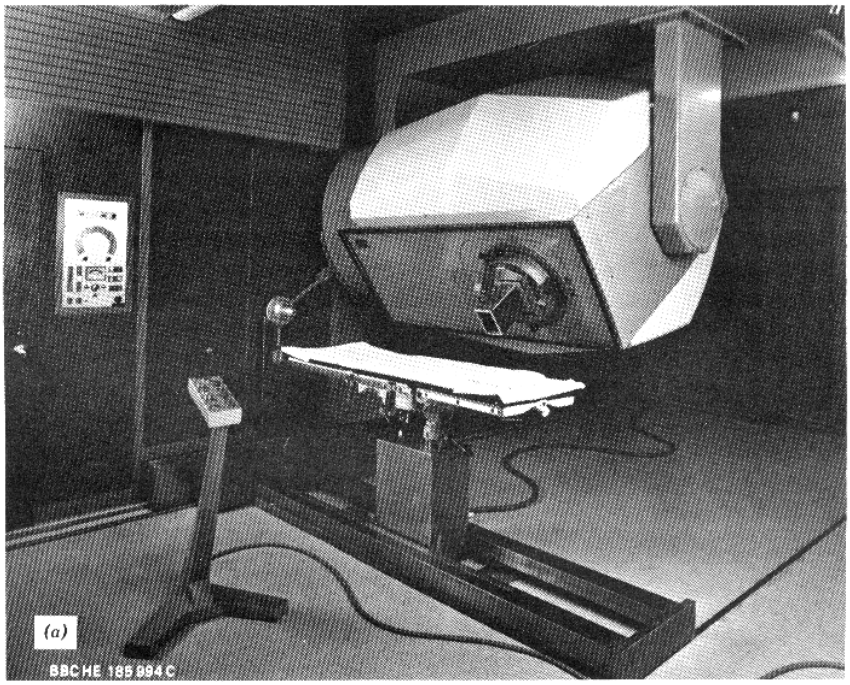

Figure 11.18 Betatron for radiation therapy (45 MeV). (*a*) Photograph of system: accelerator and treatment table. (*b*) Cross section of accelerator: gamma ray mode (top) and electron beam mode (bottom). (1) Lead shielding. (2) Transformer yokes. (3) Suspension and rotation mechanisms. (4) X-ray target. (5) Central magnet core. (6) Electron guns. (7) X-ray equalizers. (8) Lead shutter. (9) X-ray monitoring system. (10) Collimator. (11) Movable yoke for servicing. (12) Ten scatterer system for electron beam. (13) Electron radiation monitoring system. (14) Variable localizer. (Courtesy BBC Brown, Boveri and Company.)

through both windings is the same. Thus, if the number of turns and geometry of the windings are chosen properly, the ratio of bending field and core flux will be correct throughout the acceleration cycle, independent of the effective μ values in the two cores. This is another application of *flux forcing* (see Section 10.4).

The magnet design of Figure 11.16a represents another stage of improvement. It is much simpler than the magnet of Figure 11.15a and still produces a bending field without an air gap. In order to understand how this configuration works, we shall approach the circuit in parts and then determine the total magnetic field by superposition. First, consider a single coil inside the radius of the vacuum chamber, as shown in Figure 11.16b. All the magnetic flux flows through the central core as shown. In the second stage (Fig. 11.16c), we consider the field produced by a winding inside the vacuum chamber carrying current -*NI* and a windings outside the chamber carrying current +*NI*. This produces a bending field at the main orbit, and flux returns through the core as shown. In the final configuration, Figure 11.16d, the external windings are present and the windings on the flux coil are reduced by -*NI* ampere turns to generate the net field. Proper choice of the number of turns on the flux coil versus the field coils plus shunting of the bending field gap assures that the betatron condition is satisfied.

A further improvement to the magnet of Figure 11.16 to reach higher beam energy is to utilize the full available flux swing of the central core during acceleration. In the previous acceleration

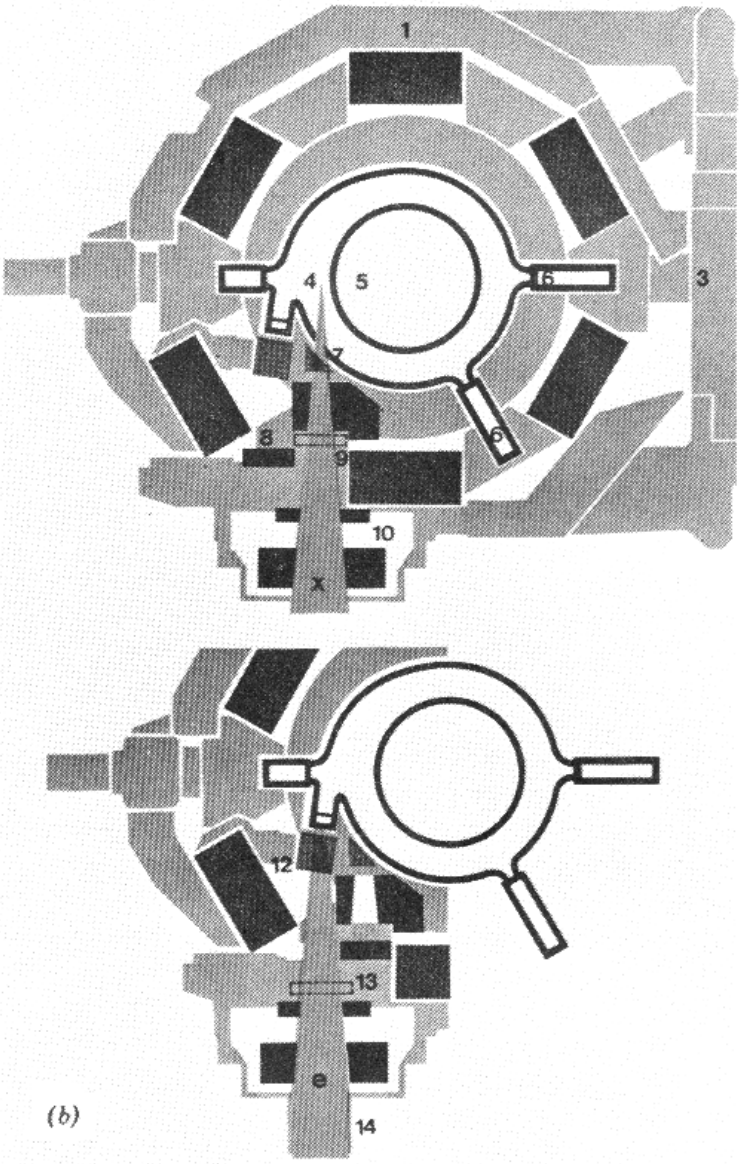

Figure 11.18 (*Continued*).

cycles we have discussed, the core field changes from 0 to $+B_s$ while the bending field changes from 0 to $+\frac{1}{2}B_s$. Inspection of Eq. (11.13) shows that the betatron condition is expressed in terms of the change of included flux, not the absolute value. An acceleration cycle in which the core magnetic field changes from $-B_s$ to $+B_s$, while the bending field changes from 0 to $+B_s$ satisfies the betatron condition and doubles the final electron energy for a given core size. There are two methods to achieve an acceleration cycle with full flux swing, *field biasing* and *flux biasing*. Field biasing is illustrated in Figure 11.17a. A dc component of magnitude $+\frac{1}{2}B_s$ is added to the bending field. Acceleration takes place over a half-cycle of the ac waveform. For

flux biasing, dc bias windings are added to the core circuit to maintain the core at $-B_s$. Bias windings are illustrated in Figure 11.16. The field and flux coils are energized in parallel to produce the accelerating waveform illustrated in Figure 11.17b. Acceleration takes place over one quarter-cycle. The main technological difficulty associated with flux biasing is that the core is driven to saturation, resulting in increased hystersis and eddy current losses. Also, during the negative half-cycle, the core has $\mu = \mu_o$ so that the circuit inductance varies considerably. Betatrons with flux biasing are usually driven by pulse power modulators rather than resonant circuits. A pulsed acceleration cycle is shown in Figure 11.17c.

A modern commercial betatron for radiation therapy is illustrated in Figure 11.18a. The machine accelerates electrons to a maximum kinetic energy of 45 MeV to generate deeply penetrating radiation. Electrons can be extracted directly or used to generate forward-directed gamma rays on an internal target. The 12,000-kG machine and the treatment table can be moved to a variety of positions to achieve precise dose profiles. A cross section of the betatron (Fig. 11.18b) illustrates operation in the gamma ray and electron modes.

12

Resonant Cavities and Waveguides

This chapter initiates our study of resonant accelerators., The category includes rf (radio-frequency) linear accelerators, cyclotrons, microtrons, and synchrotrons. Resonant accelerators have the following features in common:

1. Applied electric fields are harmonic. The continuous wave (CW) approximation is valid; a frequency-domain analysis is the most convenient to use. In some accelerators, the frequency of the accelerating field changes over the acceleration cycle; these changes are always slow compared to the oscillation period.

2. The longitudinal motion of accelerated particles is closely coupled to accelerating field variations.

3. The frequency of electromagnetic oscillations is often in the microwave regime. This implies that the wavelength of field variations is comparable to the scale length of accelerator structures. The full set of the Maxwell equations must be used.

Microwave theory relevant to accelerators is reviewed in this chapter. Chapter 13 describes the coupling of longitudinal particle dynamics to electromagnetic waves and introduces the concept of phase stability. The theoretical tools of this chapter and Chapter 13 will facilitate the study of specific resonant accelerators in Chapters 14 and 15.

As an introduction to frequency-domain analysis, Section 12.1 reviews complex exponential representation of harmonic functions. The concept of complex impedance for the analysis of passive element circuits is emphasized. Section 12.2 concentrates on a lumped element model for

the fundamental mode of a resonant cavity. The Maxwell equations are solved directly in Section 12.3 to determine the characteristics of electromagnetic oscillations in resonant cavities. Attention is centered on the TM_{010} mode because it is the most useful mode for particle acceleration. Physical properties of resonators are discussed in Section 12.4. Subjects include the Q value of a cavity and effects of competing modes. Methods of extracting energy from and coupling energy to resonant cavities are discussed in Section 12.5.

Section 12.6 develops the frequency-domain analysis of transmission lines. There are three reasons to extend the analysis of transmission lines. First, an understanding of transmission lines helps to illuminate properties of resonant cavities and waveguides. Second, transmission lines are often used to transmit power to accelerator cavities. Finally, the transmission line equations illustrate methods to match power sources to loads with reactive components, such as resonant cavities. In this application, a transmission line acts to transform the impedance of a single-frequency input. Section 12.7 treats the cylindrical resonant cavity as a radial transmission line with an open-circuit termination at the inner radius and a short-circuit termination at the outer radius.

Section 12.8 reviews the theory of the cylindrical waveguide. Waveguides are extended hollow metal structures of uniform cross section. Traveling waves are contained and transported in a waveguide; the frequency and field distribution is determined by the shape and dimensions of the guide. A lumped circuit element model is used to demonstrate approximate characteristics of guided wave propagation, such as dispersion and cutoff. The waveguide equations are then solved exactly.

The final two sections treat the topic of slow-wave structures, waveguides with boundaries that vary periodically in the longitudinal direction. They transport waves with phase velocity equal to or less than the speed of light. The waves are therefore useful for continuous acceleration of synchronized charged particles. A variety of models are used to illustrate the physics of the iris-loaded waveguide, a structure incorporated in many traveling wave accelerators. The interpretation of dispersion relationships is discussed in Section 12.10. Plots of frequency versus wavenumber yield the phase velocity and group velocity of traveling waves. It is essential to determine these quantities in order to design high-energy resonant accelerators. As an example, the dispersion relationship of the iris-loaded waveguide is derived.

12.1 COMPLEX EXPONENTIAL NOTATION AND IMPEDANCE

Circuits consisting of a harmonic voltage source driving resistors, capacitors, and inductors, are described by an equation of the form

$$\alpha\ (di/dt) + \beta\ i + \gamma \int idt = V_0 \cos\omega t. \tag{12.1}$$

The solution of Eq. (12.1) has homogeneous and particular parts. Transitory behavior must

include the homogenous part. Only the particular part need be included if we restrict our attention to CW (continuous wave) excitation. The particular solution has the form

$$i(t) = I_0 \cos(\omega t + \varphi). \tag{12.2}$$

I_0 and φ depend on the magnitude of the driving voltage, the elements of the circuit, and ω. Because Eq. (12.1) describes a physical system, the solution must reflect a physical answer. Therefore, I_0 and φ are real numbers. They can be determined by direct substitution of Eq. (12.2) into Eq. (12.1). In most cases, this procedure entails considerable manipulation of trigonometric identities.

The mathematics to determine the particular solution of Eq. (12.1) and other circuit equations with a single driving frequency can be simplified considerably through the use of the complex exponential notation for trigonometric functions. In using complex exponential notation, we must remember the following facts:

1. All physical problems must have an answer that is a real number. Complex numbers have no physical meaning.

2. Complex numbers are a convenient mathematical method for handling trigonometric functions. In the solution of a physical problem, complex numbers can always be grouped to form real numbers.

3. The answers to physical problems are often written in terms of complex numbers. This convention is used because the results can be written more compactly and because there are well-defined rules for extracting the real-number solution.

The following equations relate complex exponential functions to trigonometric functions:

$$\cos\omega t = [\exp(j\omega t) + \exp(-j\omega t)]/2, \tag{12.3}$$

$$\sin\omega t = [\exp(j\omega t) - \exp(-j\omega t)]/2j. \tag{12.4}$$

where $j = \sqrt{-1}$. The symbol j is used to avoid confusion with the current, i. The inverse relationship is

$$\exp(j\omega t) = \cos\omega t + j\sin\omega t. \tag{12.4}$$

In Eq. (12.1), the expression $V_0[\exp(j\omega t) + \exp(-j\omega t)]/2$ is substituted for the voltage, and the current is assumed to have the form

$$i(t) = A \exp(j\omega t) + B \exp(-j\omega t). \tag{12.5}$$

The coefficients A and B may be complex numbers if there is a phase difference between the voltage and the current. They are determined by substituting Eq. (12.6) into Eq. (12.1) and recognizing that the terms involving exp(jωt) and exp(-jωt) must be separately equal if the solution is to hold at all times. This procedure yields

$$A = (j\omega V_0/2) / (-\alpha\omega^2 + j\omega\beta + \gamma), \qquad (12.7)$$

$$B = (-j\omega V_0/2) / (-\alpha\omega^2 - j\omega\beta + \gamma). \qquad (12.8)$$

The complex conjugate of a complex number is the number with -j substituted for j. Note that B is the complex conjugate of A. The relationship is denoted $B = A^*$.

Equations (12.7) and (12.8) represent a formal mathematical solution of the problem; we must rewrite the solution in terms of real numbers to understand the physical behavior of the system described by Eq. (12.1). Expressing Eq. (12.2)in complex notation and setting the result equal to Eq. (12.6), we find that

$$A\exp(j\omega t) + A^*\exp(-j\omega t) = I_0\,[\exp(j\omega t)\exp(\varphi) + \exp(-j\omega t)\exp(-\varphi)]/2. \qquad (12.9)$$

Terms involving exp(jωt) and exp(-jωt) must be separately equal. This implies that

$$A = I_0\,\exp(j\varphi)/2 = I_0\,(\cos\varphi + j\sin\varphi)/2 \qquad (12.10)$$

by Eq. (12.5). The magnitude of the real solution is determined by multiplying Eq. (12.10) by its complex conjugate:

$$A \cdot A^* = I_0^2\,(\cos\varphi + j\sin\varphi)/2,$$

or

$$I_0 = 2\sqrt{A \cdot A^*}. \qquad (12.11)$$

Inspection of Eq. (12.10) shows that the phase shift is given by

$$\varphi = \tan^{-1}\left[Im(A)/Re(A)\right]. \qquad (12.12)$$

Returning to Eq. (12.1), the solution is

$$I_0 = V_0\omega / \sqrt{(\gamma - \alpha\omega^2)^2 + \omega^2\beta^2},$$

$$\varphi = \tan^{-1}(\gamma - \alpha\omega^2) / \omega\beta.$$

This is the familiar resonance solution for a driven, damped harmonic oscillator.

Part of the effort in solving the above problem was redundant. Because the coefficient of the second part of the solution must equal the complex conjugate of the first, we could have used a trial solution of the form

$$i(t) = A \exp(j\omega t). \tag{12.13}$$

We arrive at the correct answer if we remember that Eq. (12.13) represents only half of a valid solution. Once A is determined, the real solution can be extracted by applying the rules of Eq. (12.11) and (12.12). Similarly, in describing an electromagnetic wave traveling in the $+z$ direction, we will use the form $E \sim E_0 \exp[j(\omega t - kz)]$. The form is a shortened notation for the function $E \sim E_0 \exp[j(\omega t - kz)] + E_0^* \exp[-j(\omega t - kz)] \sim E_0 \cos(\omega t - kz + \varphi)$ where E_0 is a real number. The function for a wave traveling in the negative z direction is abbreviated $E \sim E_0 \exp[j(\omega t + kz)]$. Complex exponential notation is useful for solving lumped element circuits with CW excitation. In this circumstance, voltages and currents in the circuit vary harmonically at the driving frequency and differ only in amplitude and phase. In complex exponential notation, the voltage and current in a section of a circuit are related by

$$V/I = Z. \tag{12.14}$$

The quantity Z, the impedance, is a complex number that contains information on amplitude and phase. Impedance is a function of frequency.

The impedance of a resistor R is simply

$$Z_R = R. \tag{12.15}$$

A real impedance implies that the voltage and current are in phase as shown in Figure 12.1a. The time-averaged value of VI through a resistor is nonzero; a resistor absorbs energy.

The impedance of a capacitor can be calculated from Eq. (9.5). If the voltage across the capacitor is

$$V(t) = V_0 \cos\omega t, \tag{12.16}$$

then the current is

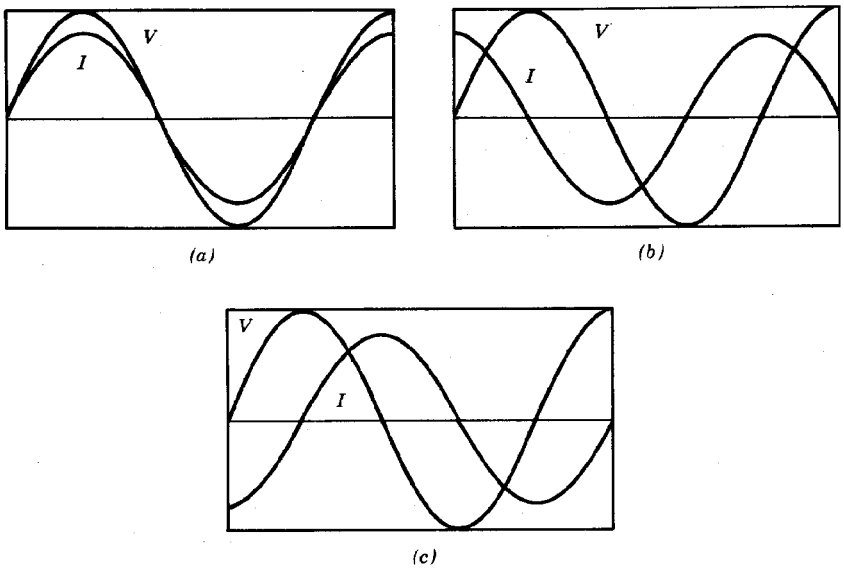

Figure 12.1 Variations of voltage and current in simple circuit elements driven at single frequency. (*a*) Resistor. (*b*) Capacitor. (*c*) Inductor.

$$i(t) = C\, dV/dt = -\omega C V_0 \sin\omega t = \omega C V_0 \cos(\omega t + \pi/2). \tag{12.17}$$

Equation (12.17) specifies the magnitude and amplitude of voltage across versus current through a capacitor. There is a 90° phase shift between the voltage and current; the current leads the voltage, as shown in Figure 12.1b. The capacitor is a reactive element; the time average of $V(t)i(t)$ is zero. In complex exponential notation, the impedance can be expressed as a single complex number

$$Z_C = (1/\omega C)\, \exp(j\pi/2) = -j/\omega C \tag{12.18}$$

if the convention of Eq. (12.13) is adopted. The impedance of a capacitor has negative imaginary part. This implies that the current leads the voltage. The impedance is inversely proportional to frequency; a capacitor acts like a short circuit at high frequency.

The impedance of an inductor can be extracted from the equation $V(t) = L\, di(t)/dt$. Again, taking voltage in the form of Eq. (12.16), the current is

$$i(t) = \frac{V_0 \sin\omega t}{\omega L} = \frac{V_0 \cos(\omega t - \pi/2}{\omega L}.$$

The current lags the voltage, as shown in Figure 12.1c. The complex impedance of an inductor is

$$Z_l = j\omega L. \tag{12.19}$$

The impedance of an inductor is proportional to frequency; inductors act like open circuits at high frequency.

12.2 LUMPED CIRCUIT ELEMENT ANALOGY FOR A RESONANT CAVITY

A resonant cavity is a volume enclosed by metal walls that supports an electromagnetic oscillation. In accelerator applications, the oscillating electric fields accelerate charged particles while the oscillating magnetic fields provide inductive isolation. To initiate the study of electromagnetic oscillations, we shall use the concepts developed in the previous section to solve a number of lumped element circuits. The first, shown in Figure 12.2, illustrates the process of inductive isolation in a resonant circuit. A harmonic voltage generator with output $V(t) = V_0 \exp(j\omega t)$ drives a parallel combination of a resistor, capacitor, and inductor. Combinations of impedances are governed by the same rules that apply to parallel and series combinations of resistors. The total circuit impedance at the voltage generator is

$$Z(\omega) = V_0 \exp(j\omega t) / I_0 \exp(j\omega t) = (1/Z_r + 1/Z_C + 1/Z_L)^{-1}. \tag{12.20}$$

The quantity I_0 is generally a complex number.

Consider the part of the circuit of Figure 12.2 enclosed in dashed lines: a capacitor in parallel with an inductor. The impedance is

$$Z(\omega) = (j\omega C + 1/j\omega L)^{-1} = j\omega L/(1-\omega^2 LC). \tag{12.21}$$

The impedance is purely imaginary; therefore, the load is reactive. At low frequency ($(\omega < 1/\sqrt{LC})$ the impedance is positive, implying that the circuit is inductive. In other words, current flow through the inductor dominates the behavior of the circuit. At high frequency, the

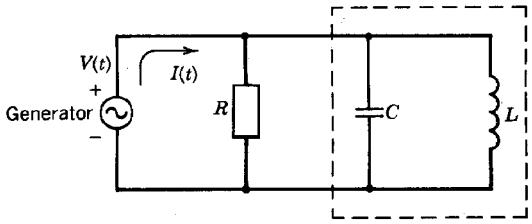

Figure 12.2 Driven *RLC* circuit with shunt resistance. Reactive section of circuit indicated by dashed line.

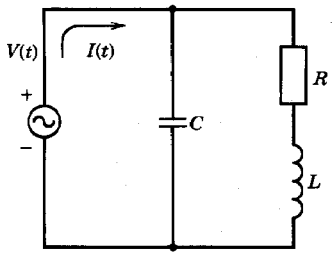

Figure 12.3 Driven *RLC* circuit; inductor with series resistance.

impedance is negative and the circuit acts as a capacitive load. When $\omega = \omega_0 = 1/\sqrt{LC}$, the impedance of the combined capacitor and inductor becomes infinite. This condition is called *resonance*; the quantity ω_0 is the resonant frequency. In this circumstance, the reactive part of the total circuit of Figure 12.2 draws no current when a voltage is applied across the resistor. All current from the generator flows into the resistive load. The reactive part of the circuit draws no current at $\omega = \omega_0$ because current through the inductor is supplied completely by displacement current through the capacitor. At resonance, the net current from the generator is minimized for a given voltage. This is the optimum condition for energy transfer if the generator has nonzero output impedance.

The circuit of Figure 12.3 illustrates power losses in resonant circuits. Again, an inductor and capacitor are combined in parallel. The difference is that the inductor is imperfect. There are resistive losses associated with current flow. The losses are represented by a series resistor. The impedance of the circuit is

$$Z(\omega) = [j\omega C + 1/(j\omega L + R)]^{-1} = [j\omega L + R] \,/\, [(1 - \omega^2 LC) + j\omega RC].$$

Converting the denominator in the above equation to a real number, we find that the magnitude of the impedance is proportional to

$$Z(\omega) \sim 1/[(1 - \omega^2/\omega_0^2)^2 + (\omega RC)^2]. \qquad (12.22)$$

Figure 12.4 shows a plot of total current flowing in the reactive part of the circuit versus current input from the generator. Two cases are plotted: resonant circuits with low damping and high damping. Note that the impedance is no longer infinite at $\omega = 1/\sqrt{LC}$. For a cavity with resistive losses, power must be supplied continuously to support oscillations. A circuit is in resonance when large reactive currents flow in response to input from a harmonic power generator. In other words, the amplitude of electromagnetic oscillations is high. Inspection of Figure 12.4 and Eq. (12.22) shows that there is a finite response width for a driven damped resonant circuit. The frequency width, $\Delta\omega = \omega - \omega_0$, to reduce the peak impedance by a factor of 5 is

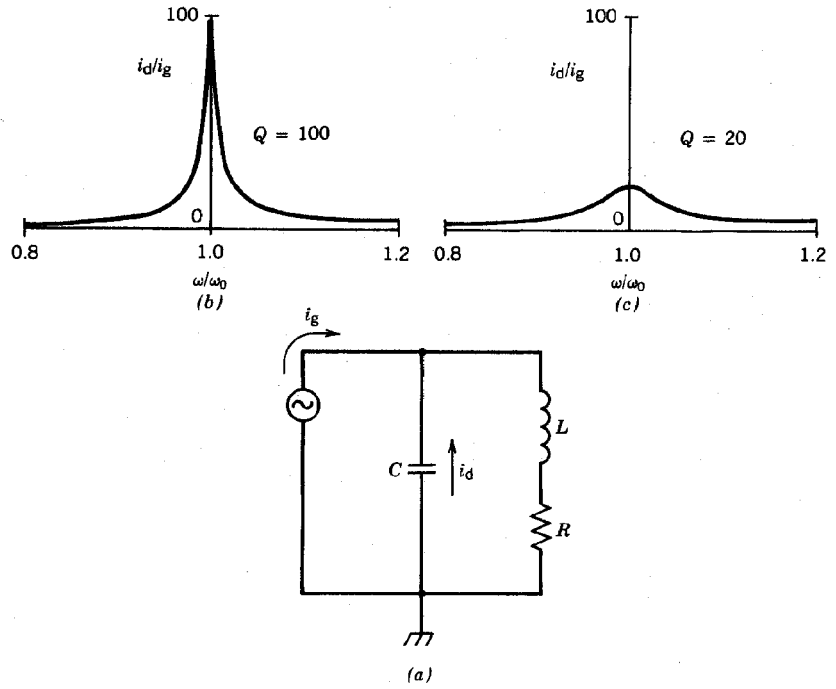

Figure 12.4 Resonant drive of *RLC* circuit. (*a*) Circuit diagram; circle represents ac generator. (*b*) Ratio of reactive current to current input from generator (i_d/i_g); $Q = 100$. (*c*) i_d/i_g; $Q = 20$.

$$\frac{\Delta\omega}{\omega_0} \cong \frac{R}{\sqrt{LC}}. \tag{12.23}$$

Resonant circuits are highly underdamped; therefore, $\Delta\omega/\omega \ll 1$.

Resonant circuit damping is parametrized by the quantity Q. The circuit Q is defined as

$$\begin{aligned} Q &= \frac{\omega_0\ (\textit{energy stored in the resonant circuit})}{(\textit{time-averaged power loss})} \\ &= \frac{\pi\ (\textit{energy stored in the resonant circuit})}{(\textit{energy lost per half cycle})} \end{aligned} \tag{12.24}$$

In the limit of low damping near resonance, the reactive current exchanged between the inductor and capacitor of the circuit of Figure 12.3 is much larger than the current input from the generator. The reactive current is $i(t) = I_0 \exp(j\omega t)$, where I_0 is a slowly decreasing function of time. The circuit energy, U, is equal to the energy stored in the inductor at peak current:

$$U = LI_0 I_0^*/2 \tag{12.25}$$

Energy is lost to the resistor. The power lost to the resistor (averaged over a cycle) is

$$\overline{P} = \overline{i(t)^2}\ R = \tfrac{1}{2} I_0 I_0^* R. \tag{12.26}$$

Substituting Eqs. (12.25) and (12.26) into Eq. (12.24), the Q value for the LRC circuit of Figure 12.3 is

$$Q \cong \omega_0 L/R = \sqrt{L/C}\ /\ R. \tag{12.27}$$

In an underdamped circuit, the characteristic impedance of the LC circuit is large compared to the resistance, so that $Q \gg 1$.

Energy balance can be used to determine the impedance that the circuit of Figure 12.3 presents to the generator at resonance. The input voltage V_0 is equal to the voltage across the capacitor. The input voltage is related to the stored energy in the circuit by

$$U = CV_0^2/2 = V_0^2\ /\ 2\omega_0\sqrt{L/C}. \tag{12.28}$$

By the definition of Q, the input voltage is related to the average power loss by

$$\overline{P} = V_0^2\ /\ 2Q\sqrt{L/C}. \tag{12.29}$$

Defining the resistive input impedance so that

$$\overline{P} = \overline{V^2(t)}\ /\ R_{in} = V_0^2\ /\ 2R_{in}, \tag{12.30}$$

we find at resonance ($\omega \cong \omega_0$) that

$$R_{in} \cong Q\ \sqrt{L/C} = (\sqrt{L/C})^2\ /\ R. \tag{12.31}$$

The same result can be obtained directly from the general impedance expression in the limit $\sqrt{L/C} \gg R$. The impedance is much larger than R. This reflects the fact that the reactive current is much larger than the current from the generator. In terms of Q, the resonance width of an

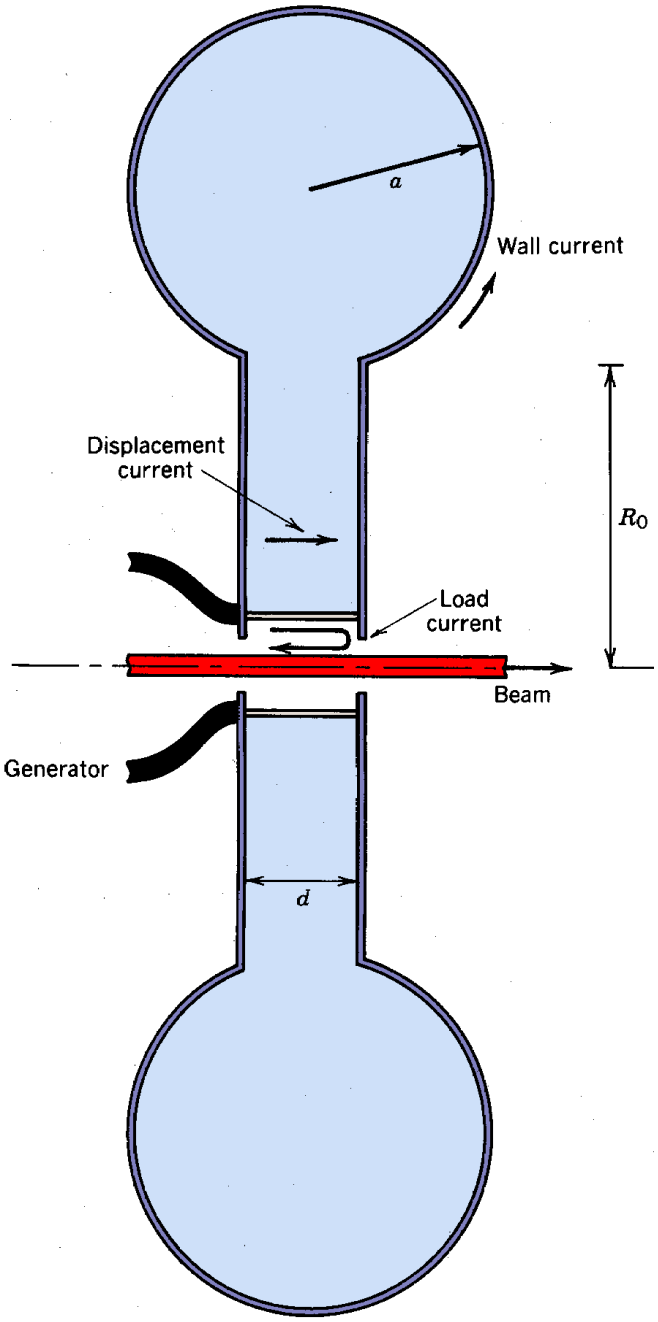

Figure 12.5 Reentrant cavity with on-axis power input.

imperfect oscillating circuit [Eq. (12.23)] can be written

$$\Delta\omega/\omega_0 \cong 1/Q. \tag{12.32}$$

Resonant cavities used for particle acceleration have many features in common with the circuits we have studied in this section. Figure 12.5 illustrates a particularly easy case to analyze, the reentrant cavity. This cavity is used in systems with space constraints, such as klystrons. It oscillates at relatively low frequency for its size. The reentrant cavity can be divided into predominantly capacitive and predominantly inductive regions. In the central region, there is a narrow gap. The capacitance is large and the inductance is small. A harmonic voltage generator connected at the center of the cavity induces displacement current. The enlarged outer region acts as a single-turn inductor. Real current flows around the wall to complete the circuit. If the walls are not superconducting, the inductor has a series resistance.

Assume that there is a load, such as a beam, on the axis of the cavity. Neglecting cavity resistance, the circuit is the same as that of Figure 12.2. If the generator frequency is low, most of the input current flows around the metal wall (leakage current). The cavity is almost a short circuit. At high frequency, most of the current flows across the capacitor as displacement current. At the resonance frequency of the cavity, the cavity impedance is infinite and all the generator energy is directed into the load. In this case, the cavity can be useful for particle acceleration. When the cavity walls have resistivity, the cavity acts as a high impedance in parallel to the beam load. The generator must supply energy for cavity losses as well as energy to accelerate the beam.

The resonant cavity accelerator has much in common with the cavity of an induction linear accelerator. The goal is to accelerate particles to high energy without generating large electrostatic voltages. The outside of the accelerator is a conductor; voltage appears only on the beamline. Electrostatic voltage is canceled on the outside of the accelerator by inductively generated fields. The major difference is that leakage current is inhibited in the induction linear accelerator by ferromagnetic inductors. In the resonant accelerator, a large leakage current is maintained by reactive elements. The linear induction accelerator has effective inductive isolation over a wide frequency range; the resonant accelerator operates at a single frequency. The voltage on the axis of a resonant cavity is bipolar. Therefore, particles are accelerated only during the proper half-cycle. If an accelerator is constructed by stacking a series of resonant cavities, the crossing times for particles must be synchronized to the cavity oscillations.

The resonant frequency of the reentrant cavity can be estimated easily. Dimensions are illustrated in Figure 12.5. The capacitance of the central region is $C \cong \varepsilon_o \pi R_0^2/d,$ and the inductance is $L \cong \mu_o \pi a^2/2\pi(R_0+a)$.. The resonant angular frequency is

$$\omega_0 = 1/\sqrt{LC} \cong \sqrt{2\pi(R_0+a)d/\varepsilon_o\mu_o R_0^2 a^2\pi^2} = c\sqrt{2(R_0+a)d/R_0^2 a^2\pi}. \qquad (12.33)$$

12.3 RESONANT MODES OF A CYLINDRICAL CAVITY

The resonant modes of a cavity are the natural modes for electromagnetic oscillations. Once excited, a resonant mode will continue indefinitely in the absence of resistivity with no further input of energy. In this section, we shall calculate modes of the most common resonant structure

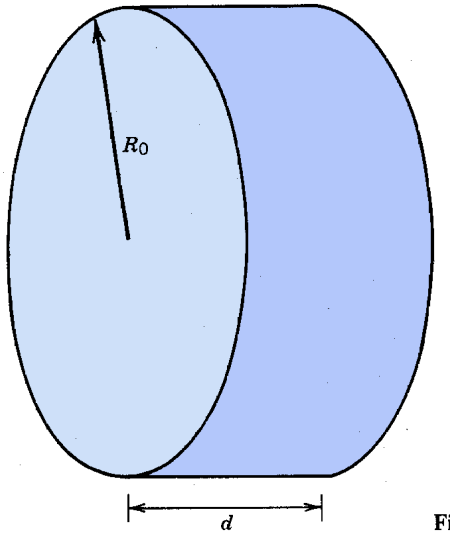

Figure 12.6 Geometry of cylindrical resonant cavity.

encountered in particle accelerator applications, the cylindrical cavity (Fig. 12.6). The cavity length is denoted d and radius R_0.In the initial treatment of resonant modes, we shall neglect the perturbing effects of power feeds, holes for beam transport, and wall resistivity. The cylindrical cavity has some features in common with the reentrant cavity of Section 2.2. A capacitance between the upstream and downstream walls carries displacement current. The circuit is completed by return current along the walls. Inductance is associated with the flow of current. The main difference from the reentrant cavity is that regions of electric field and magnetic field are intermixed. In this case, a direct solution of the Maxwell equations is more effective than an extension of the lumped element analogy. This approach demonstrates that resonant cavities can support a variety of oscillation modes besides the low-frequency mode that we identified for the reentrant cavity.

We seek solutions for electric and magnetic fields that vary in time according to $\exp(j\omega t)$. We must use the full set of coupled Maxwell equations [Eqs. (3.1l)-(3.14)]. We allow the possibility of a uniform fill of dielectric or ferromagnetic material; these materials are assumed to be linear, characterized by parameters ε and μ. The field equations are

$$\nabla \times \boldsymbol{E} + \partial \boldsymbol{B}/\partial t = 0, \qquad (12.34)$$

$$\nabla \cdot \boldsymbol{E} = 0, \qquad (12.35)$$

$$\nabla \times \boldsymbol{B} - \varepsilon\mu\, \partial \boldsymbol{E}/\partial t = 0, \qquad (12.36)$$

$$\nabla \cdot \boldsymbol{B} = 0. \qquad (12.37)$$

Applying the vector identity $\nabla \times (\nabla \times \boldsymbol{V}) = \nabla(\nabla \cdot \boldsymbol{V}) - \nabla^2 \boldsymbol{V}$, Eqs. (12.34)-(12.37) can be rewritten as

$$\nabla^2 \boldsymbol{E} - (1/v^2)\, \partial^2 \boldsymbol{E}/\partial t^2 = 0, \qquad (12.38)$$

$$\nabla^2 \boldsymbol{B} - (1/v^2)\, \partial^2 \boldsymbol{B}/\partial t^2 = 0. \qquad (12.39)$$

where v is the velocity of light in the cavity medium,

$$v = c / \sqrt{\varepsilon\mu/\varepsilon_o\mu_o}. \qquad (12.40)$$

The features of electromagnetic oscillations can be found by solving either Eq. (12.38) or (12.39) for **E** or **B**. The associated magnetic or electric fields can then be determined by substitution into Eq. (12.34) or (12.36). Metal boundaries constrain the spatial variations of fields. The wave equations have solutions only for certain discrete values of frequency. The values of resonant frequencies depend on how capacitance and inductance are partitioned in the mode.

The general solutions of Eqs. (12.38) and (12.39) in various cavity geometries are discussed in texts on electrodynamics. We shall concentrate only on resonant modes of a cylindrical cavity that are useful for particle acceleration. We shall solve Eq. (12.38) for the electric field since there are easily identified boundary conditions. The following assumptions are adopted:

1. Modes of interest have azimuthal symmetry ($\partial/\partial\theta = 0$).

2. The electric field has no longitudinal variation, or $\partial \boldsymbol{E}/\partial z = 0$.

3. The only component of electric field is longitudinal, E_z.

4. Fields vary in time as exp(jωt).

The last two assumptions imply that the electric field has the form

$$\boldsymbol{E} = E_z(r)\, \exp(j\omega t)\, \boldsymbol{u_z}. \qquad (12.41)$$

Using the cylindrical coordinate form of the Laplacian operator, dropping terms involving azimuthal and longitudinal derivatives, and substituting Eq. (12.41), we find that the class of resonant modes under consideration satisfies the equation

$$\frac{d^2E_z(r)}{dr^2} + \frac{1}{r}\frac{dE_z(r)}{dr} + \frac{\omega^2}{v^2} E_z(r) = 0. \qquad (12.42)$$

Equation (12.42) is expressed in terms of total derivatives because there are only radial variations. Equation (12.42) is a special form of the Bessel equation. The solution can be expressed in terms

TABLE 12.1 Parameters of TM_{0n0} Modes

Mode	k_n	ω_n
TM_{010}	$2.405/R_0$	$2.405/\sqrt{\varepsilon\mu}\,R_0$
TM_{020}	$5.520/R_0$	$5.520/\sqrt{\varepsilon\mu}\,R_0$
TM_{030}	$8.654/R_0$	$8.654/\sqrt{\varepsilon\mu}\,R_0$
TM_{040}	$11.792/R_0$	$11.792/\sqrt{\varepsilon\mu}\,R_0$

of the zero-order Bessel functions, $J_0(k_nr)$ and $Y_0(k_nr)$. The Y_0 function is eliminated by the requirement that E_z has a finite value on the axis. The solution is

$$E_{zn}(r,t) = E_{0n}\, J_0(k_n r)\, \exp(j\omega t), \tag{12.43}$$

where E_{0n} is the magnitude of the field on the axis.

The second boundary condition is that the electric field parallel to the metal wall at $r = R_0$ must be zero, or $E_z(R_0,t) = 0$. This implies that only certain values of k_n give valid solutions. Allowed values of k_n are determined by the zeros of J_0 (Table 12.1). A plot of $E_z(r)$ for $n = 1$ is given in Figure 12.7. Substituting Eq. (12.43) into Eq. (12.42), the angular frequency is related to the

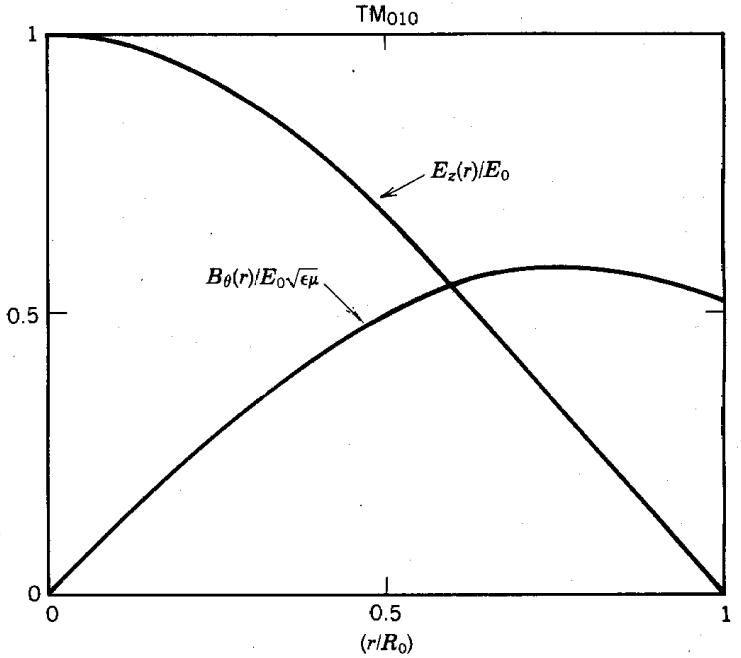

Figure 12.7 Normalized electric axial electric field and azimuthal magnetic field as a function of radius; TM_{010} mode in a cylindrical cavity.

wavenumber k_n by

$$\omega_n = vk_n. \tag{12.44}$$

Angular frequency values are tabulated in Table 12.1.

The magnetic field of the modes can be calculated from Eq. (12.34),

$$\partial \boldsymbol{B}/\partial t = -(\nabla \times \boldsymbol{E}). \tag{12.45}$$

Magnetic field is directed along the θ direction. Assuming time variation exp(jωt) and substituting from Eq. (12.43),

$$j\omega_n B_{\theta n} = dE_{zn}/dr = E_{0n}\, dJ_0(k_n r)/dr. \tag{12.46}$$

Rewriting Eq. (12.46),

$$B_{\theta n}(r) = -j\sqrt{\varepsilon\mu}\, E_{0n}\, J_1(k_n r).$$

Magnetic field variation for the TM_{010} mode is plotted in Figure 12.7. The magnetic field is zero on the axis. Moving outward in radius, B_θ increases linearly. It is proportional to the integral of axial displacement current from 0 to r. Toward the outer radius, there is little additional contribution of the displacement current. The l/r factor [see Eq. (4.40)] dominates, and the magnitude of B_θ decreases toward the wall.

12.4 PROPERTIES OF THE CYLINDRICAL RESONANT CAVITY

In this section, we consider some of the physical implications of the solutions for resonant oscillations in a cylindrical cavity. The oscillations treated in the previous section are called TM_{0n0} modes. The term TM (transverse magnetic) indicates that magnetic fields are normal to the longitudinal direction. The other class of oscillations, TE modes, have longitudinal components of **B**, and $E_z = 0$. The first number in the subscript is the azimuthal mode number; it is zero for azimuthally symmetric modes. The second number is the radial mode number. The radial mode number minus one is the number of nodes in the radial variation of E_z. The third number is the longitudinal mode number. It is zero in the example of Section 12.3 because E_z is constant in the z direction. The wavenumber and frequency of TM_{0n0} modes depends only on R_0, not d. This is not generally true for other types of modes.

TM_{0n0} modes are optimal for particle acceleration. The longitudinal electric field is uniform along the propagation direction of the beam and its magnitude is maximum on axis. The

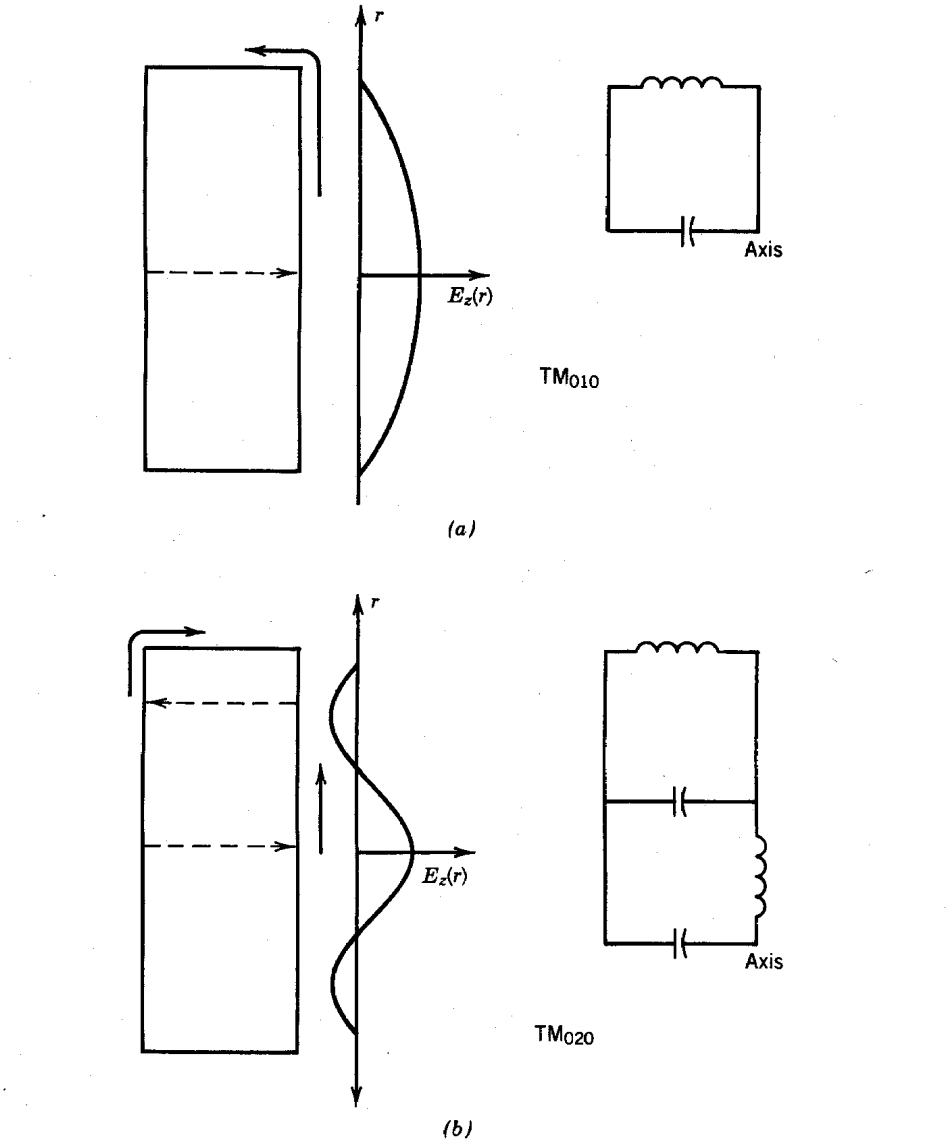

Figure 12.8 Spatial variations of axial electric field and equivalent circuits for electromagnetic oscillations in a cylindrical resonant cavity. Dashed line indicates displacement current, solid line indicates real current flow in the cavity walls. (*a*) TM_{010} mode. (*b*) TM_{020} mode.

transverse magnetic field is zero on axis; this is important for electron acceleration where transverse magnetic fields could deflect the beam. TM modes with nonzero longitudinal wavenumber (p ≠ 0) have axial electric field of the form $E_z(0,z) \sim \sin(p\pi x/d)$; it is clear that the acceleration of particles crossing the cavity is reduced for these modes.

Figure 12.8 clarifies the nature of TM_{0n0} modes in terms of lumped circuit element approximations. Displacement currents and real currents are indicated along with equivalent circuit models. At values of *n* greater than 1, the cavity is divided into *n* interacting resonant *LC*

circuits. The capacitance and inductance of each circuit is reduced by a factor of about l/*n*; therefore, the resonant frequency of the combination of elements is increased by a factor close to *n*.

Resonant cavities are usually constructed from copper or copper-plated steel for the highest conductivity. Nonetheless, effects of resistivity are significant because of the large reactive current. Resistive energy loss from the flow of real current in the walls is concentrated in the inductive regions of the cavity; hence, the circuit of Figure 12.3 is a good first-order model of an imperfect cavity. Current penetrates into the wall a distance equal to the skin depth [Eq. (10.7)]. Power loss is calculated with the assumption that the modes approximate those of an ideal cavity. The surface current per length on the walls is $J_s = B_\theta(r,z,t)/\mu_o$. Assuming that the current is distributed over a skin depth, power loss can be summed over the surface of the cavity. Power loss clearly depends on mode structure through the distribution of magnetic fields. The *Q* value for the TM_{010} mode of a cylindrical resonant cavity is

$$Q = \frac{d/\delta}{1 + d/R_0} \tag{12.48}$$

where the skin depth δ is a function of the frequency and wall material. In a copper cavity oscillating at $f = 1$ GHz, the skin depth is only 2 μm. This means that the inner wall of the cavity must be carefully plated or polished; otherwise, current flow will be severely perturbed by surface irregularities lowering the cavity *Q*. With a skin depth of 2 μm, Eq. (12.48) implies a *Q* value of 3×10^4 in a cylindrical resonant cavity of radius 12 cm and length 4 cm. This is a very high value compared to resonant circuits composed of lumped elements. Equation (12.32) implies that the bandwidth for exciting a resonance

$$\Delta f/f_0 \cong 1/Q = 3 \times 10^{-5}.$$

An rf power source that drives a resonant cavity must operate with very stable output frequency. For $f_0 = 1$ GHz, the allowed frequency drift is less than 33 kHz.

The total power lost to the cavity walls can be determined from Eq. (12.24) if the stored energy in the cavity, U, is known. The quantity can be calculated from Eq. (12.43) for the TM_{010} mode; we assume the calculation is performed at the time when magnetic fields are zero.

$$U = \int_0^d dz \int_0^{R_0} 2\pi r dr \; (\varepsilon E_o^2/2) \; J_0^2(2.405r/R_0) = (\pi R_0^2 d) \; (\varepsilon E_0^2/2) \; J_1^2(2.405). \tag{12.49}$$

A cylindrical cavity can support a variety of resonant modes, generally at higher frequency than the fundamental accelerating mode. Higher-order modes are generally undesirable. They do not

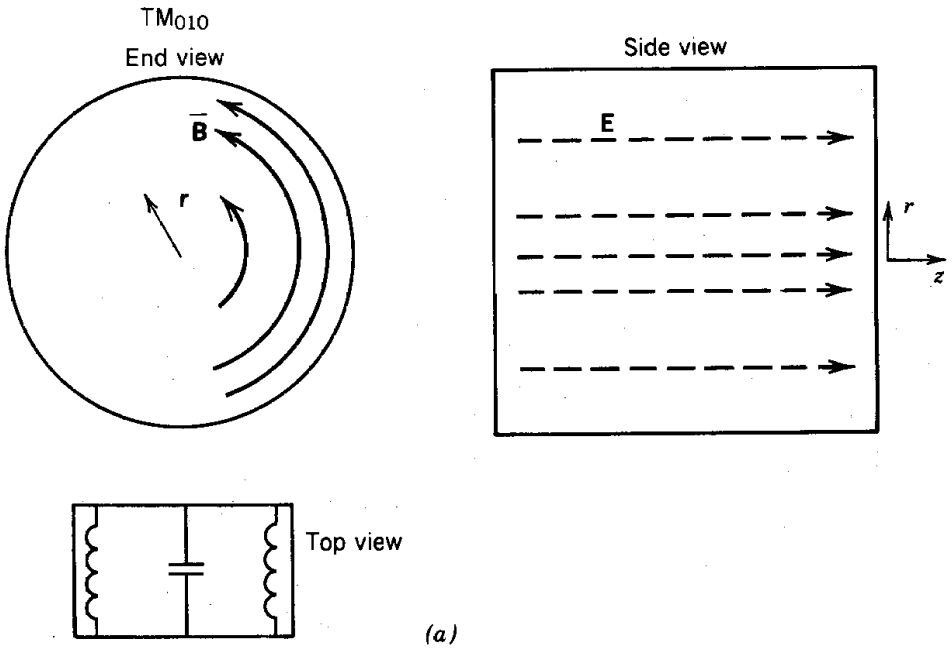

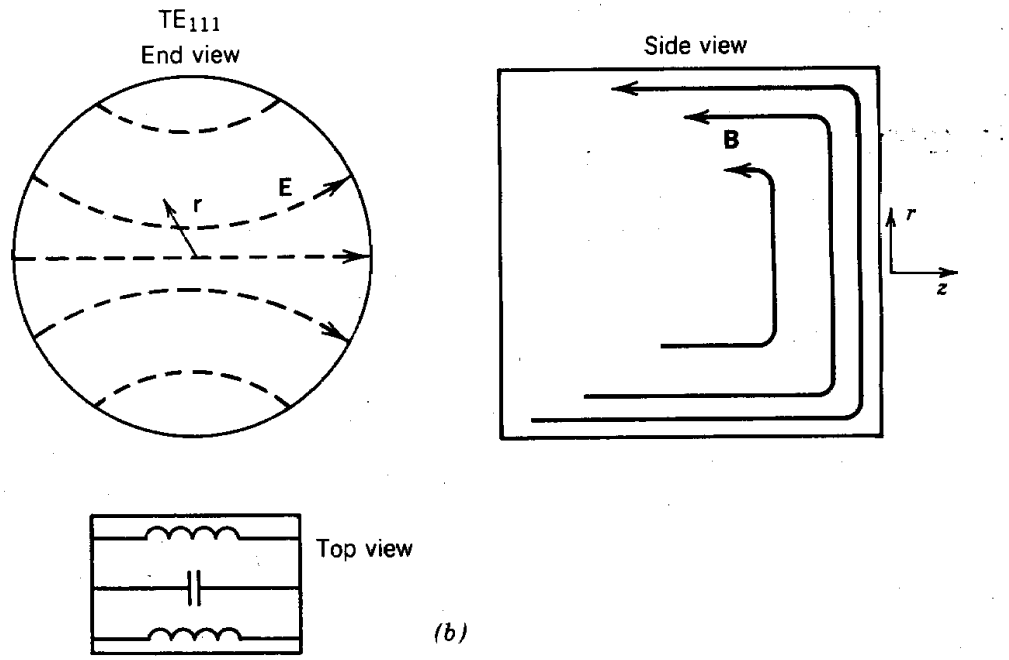

Figure 12.9 Field variations and distribution of capacitance and inductance in cylindrical resonant cavity. (*a*) TM_{010} mode. (*b*) TE_{111} mode.

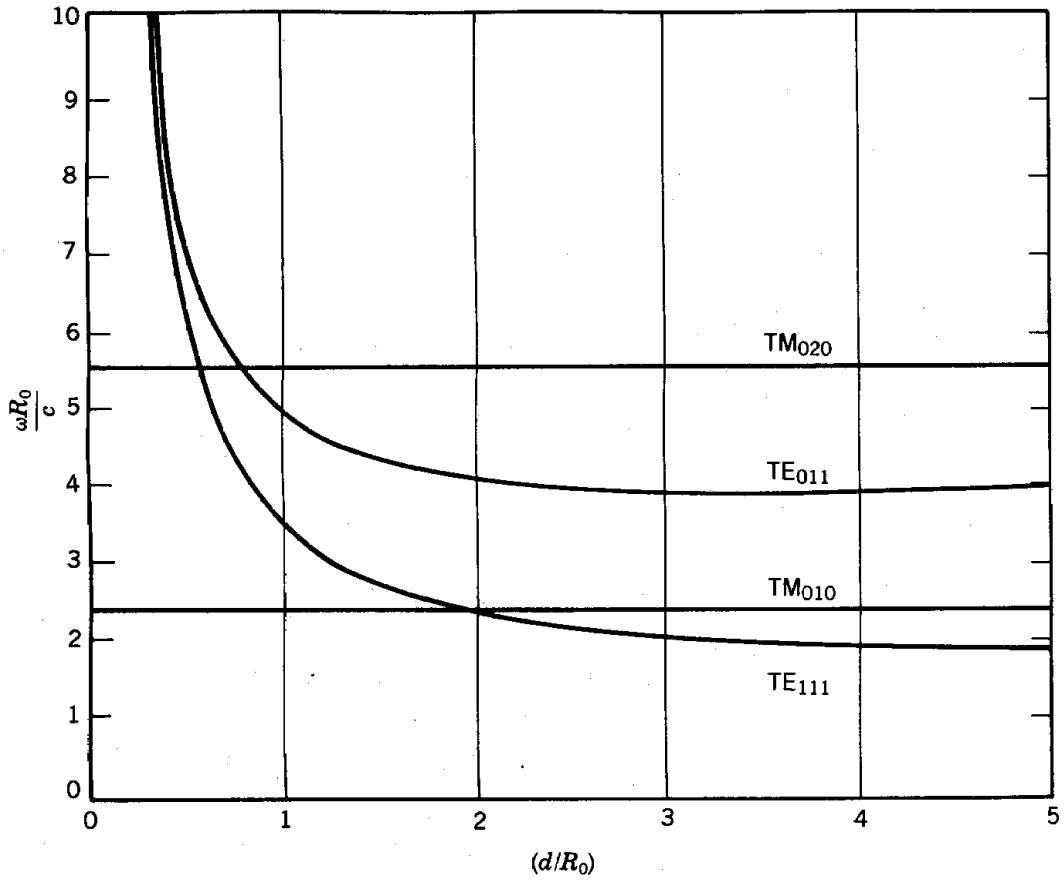

Figure 12.10 Variation of resonant angular frequency with geometry of cylindrical resonant cavity for various low-frequency modes.

contribute to particle acceleration; the energy shunted into higher-order modes is wasted. Sometimes, they interfere with particle acceleration; modes with transverse field components may induce beam deflections and particle losses.

As an example of an alternate mode, consider the lowest frequency TE mode, the TE_{111} mode. Figure 12.9 shows a sketch of the electric and magnetic fields. The displacement current oscillates from side to side across the diameter of the cavity. Magnetic fields are wrapped around the displacement current and have components in the axial direction. The distribution of capacitance and inductance for TE_{111} oscillations is also shown in Figure 12.9. The mode frequency depends on the cavity length (Fig. 12.10). As d increases over the range $d \ll R_0$ to $d \geq R_0$, there is a large increase in the capacitance of the cavity for displacement current flow across a diameter. Thus, the resonant frequency drops. For $d \gg R_0$, return current flows mainly back along the circular wall of the cavity. Therefore, the ratio of electric to magnetic field energy in the cavity approaches a constant value, independent of d. Inspection of Figure 2.10 shows that in long cavities, the TE_{111} mode has a lower frequency than the TM_{010}. Care must be taken not to excite the TE_{111} mode in parameter regions where there is *mode degeneracy*. The term degeneracy

indicates that two modes have the same resonant frequency. Mode selection is a major problem in the complex structures used in linear ion accelerators. Generally, the cavities are long cylinders with internal structures; the mode plot is considerably more complex than Figure 12.10. There is a greater possibility for mode degeneracy and power coupling between modes. In some cases, it is necessary to add metal structures to the cavity, which selectively damp competing modes.

12.5 POWER EXCHANGE WITH RESONANT CAVITIES

Power must be coupled into resonant cavities to maintain electromagnetic oscillations when there is resistive damping or a beam load. The topic of power coupling to resonant cavities involves detailed application of microwave theory. In this section, the approach is to achieve an understanding of basic power coupling processes by studying three simple examples.

We have already been introduced to a cavity with the power feed located on axis. The feed drives a beam and supplies energy lost to the cavity walls. In this case, power is electrically coupled to the cavity because the current in the power feeds interacts predominantly with electric fields. Although this geometry is never used for driving accelerator cavities, there is a practical application of the inverse process of driving cavity oscillations by a beam. Figure 12.11a shows a klystron, a microwave generator. An on-axis electron beam is injected across the cavity. The electron beam has time-varying current with a strong Fourier component at the resonant frequency of the cavity, ω_0. We will consider only this component of the current and represent it as a harmonic current source. The cavity has a finite Q, resulting from wall resistance and extraction of microwave energy.

The complete circuit model for the TM_{010} mode is shown in Figure 12.llb. The impedance presented to the component of the driving beam current with frequency ω is

$$Z = (j\omega L + R) \;/\; [(1 - \omega^2 LC) + j\omega RC]. \tag{12.50}$$

Assuming that $\omega = \omega_0 - 1/\sqrt{LC}$ and that the cavity has high Q, Eq. (12.50) reduces to

$$Z \cong L/RC = Z_0^2/R = QZ_0, \tag{12.51}$$

with Q given by Eq. (12.27). The impedance is resistive; the voltage oscillation induced is in phase with the driving current so that energy extraction is maximized. Equation (12.51) shows that the cavity acts as a step-down transformer when the power feed is on axis. Power at low current and high voltage (impedance Z_0^2/R) drives a high current through resistance R.

In applications to high-energy accelerators, the aim is to use resonant cavities as step-up transformers. Ideally, power should be inserted at low impedance and coupled to a low-current

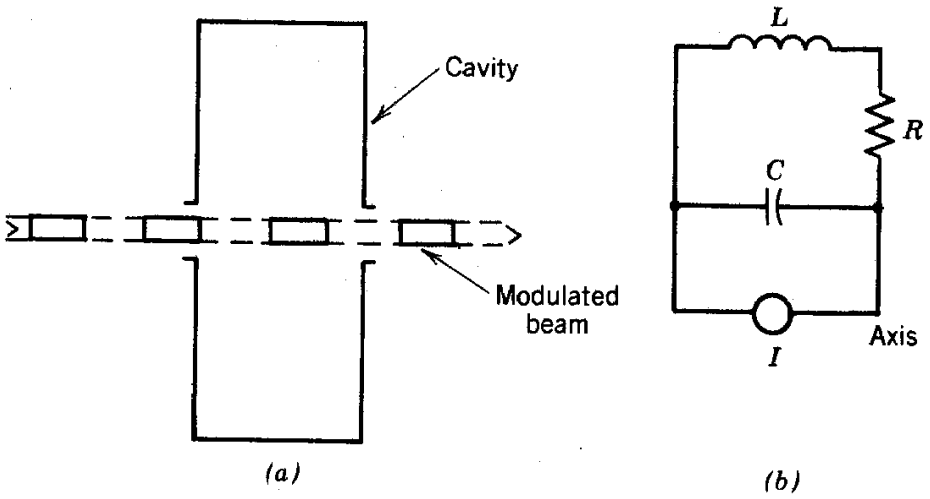

Figure 12.11 Electromagnetic oscillations in resonant cavity driven by modulated beam on axis (klystron). (*a*) Geometry. (*b*) Equivalent circuit.

beam at high voltage. This process is accomplished when energy is *magnetically coupled* into a cavity. With magnetic coupling, the power input is close to the outer radius of the cavity; therefore, interaction is predominantly through magnetic fields. A method for coupling energy to the TM_{010} mode is illustrated in Figure 12.12a. A loop is formed on the end of a transmission line. The loop is orientated to encircle the azimuthal magnetic flux of the TM_{010} mode. (A loop optimized to drive the TE_{111} mode would be rotated 90° to couple to radial magnetic fields.)

We shall first consider the inverse problem of extracting the energy of a TM_{010} oscillation through the loop. Assume that the loop couples only a small fraction of the cavity energy per oscillation period. In this case, the magnetic fields of the cavity are close to the unperturbed distribution. The magnetic field at the loop position, ρ, is

$$B(t) = B_0(\rho,t)\ \cos\omega t, \tag{12.52}$$

where $B_0(\rho,t)$ is a slowly varying function of time. The spatial variation is given by Eq. (12.47). The loop is attached to a transmission line that is terminated by a matched resistor R.

The voltage induced at the loop output depends on whether the loop current significantly affects the magnetic flux inside the loop. As we saw in the discussion of the Rogowski loop (Section 9.14), the magnetic field inside the loop is close to the applied field when $L/R \ll 1/\omega_o$, where L is the loop inductance and $1/\omega_o$ is the time scale for magnetic field variations. In this limit, the magnitude of the induced voltage around a loop of area A_l is $V \cong A_l\omega_o B_0$. The extracted power is

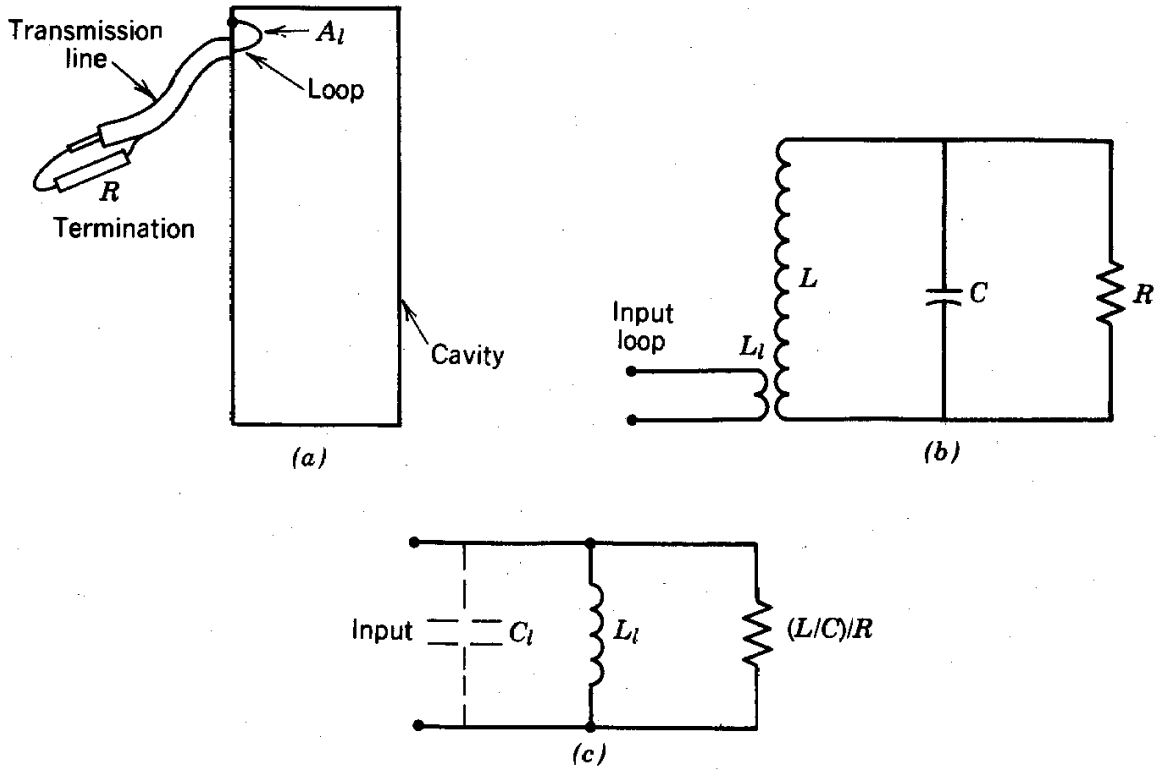

Figure 12.12 Resonant cavity interactions with magnetic coupling loop. (*a*) Geometry of loop set up to extract energy from cavity. (*b*) Equivalent circuit model to give input impedance of loop coupled to cavity. (*c*) Circuit of part *b* at resonance (transformer replaced by its equivalent circuit).

$$P \cong (A_l B_0 \omega)^2 / 2R. \tag{12.53}$$

Power coupled out of the cavity increases as A_l^2 in this regime. At the opposite extreme ($L/R \gg 1/\omega_o$), the loop voltage is shifted 90° in phase with respect to the magnetic field. Application of Eq. (9.124) shows that the extracted power is approximately

$$P \cong [A_l B_o/(L/R)]^2 / 2R. \tag{12.54}$$

Because the loop inductance is proportional to A_l, the power is independent of the loop area in this limit. Increasing A_l increases perturbations of the cavity modes without increasing power output. The optimum size for the coupling loop corresponds to maximum power transfer with minimum perturbation, or $L/R \sim 1/\omega_o$.

Note that in Eqs. (12.53) and (12.54), power loss from the cavity is proportional to B_0^2 and is therefore proportional to the stored energy in the cavity, U. The quantity U is governed by the equation

$$dU/dt \sim -U. \tag{12.55}$$

The stored energy decays exponentially; therefore, losses to the loop can be characterized by a Q factor Q_l. If there are also resistive losses in the cavity characterized by Q_c, then the total cavity Q is

$$Q = (1/Q_l + 1/Q_c)^{-1}. \tag{12.56}$$

We can now proceed to develop a simple circuit model to describe power transfer through a magnetically coupled loop into a cavity with a resistive load on axis. The treatment is based on our study of the transformer (Section 9.2). The equivalent circuit model is illustrated in Figure 12.12b. The quantity R represents the on-axis load. We consider the loop as the primary and the flow of current around the outside of the cavity as the secondary. The primary and secondary are linked together through shared magnetic flux. The loop area is much smaller than the cross-section area occupied by cavity magnetic fields. An alternate view of this situation is that there is a large secondary inductance, only part of which is linked to the primary.

Following the derivation of Section 9.2, we can construct the equivalent circuit seen from the primary input (Fig. 12.12c). The part of the cavity magnetic field enclosed in the loop is represented by L_l; the secondary series inductance is L - L_l. We assume that energy transfer per oscillation period is small and that $L_l \ll L$. Therefore, the magnetic fields are close to those of an unperturbed cavity. This assumption allows a simple estimate of L_l.

To begin, we neglect the effect of the shunt inductance L_l in the circuit of Figure 12.12c and calculate the impedance the cavity presents at the loop input. The result is

$$Z = [j\omega L + R(1-\omega^2 LC)] / (1+j\omega RC). \tag{12.57}$$

Damping must be small for an oscillatory solution. This is true if the load resistance is high, or $R \gg \sqrt{LC}$. Assuming this limit and taking $\omega = \omega_o$, Eq. (12.57) becomes

$$Z \cong R\ [(L/C)/R^2]. \tag{12.58}$$

Equation (12.58) shows that the cavity presents a purely resistive load with impedance much smaller than R. The combination of coupling loop and cavity act as a step-up transformer.

We must still consider the effect of the primary inductance in the circuit of Figure 12.12c. The best match to typical power sources occurs when the total input impedance is resistive. A simple

method of matching is to add a shunt capacitor C_1, with a value chosen so that $C_1L_1 = LC$. In this case, the parallel combination of L_1 and C_1 has infinite impedance at resonance, and the total load is $(L/C)/R$. Matching can also be performed by adjustment of the transmission fine leading to the cavity. We shall see in Section 12.6 that transmission lines can act as impedance transformers. The total impedance will appear to be a pure resistance at the generator for input at a specific frequency if the generator is connected to the cavity through a transmission line of the proper length and characteristic impedance.

12.6 TRANSMISSION LINES IN THE FREQUENCY DOMAIN

In the treatment of the transmission line in Section 9.8, we considered propagating voltage pulses with arbitrary waveform. The pulses can be resolved into frequency components by Fourier analysis. If the waveform is limited to a single frequency, the description of electromagnetic signal propagation on a transmission line is considerably simplified. In complex exponential notation, current is proportional to voltage. The proportionality constant is a complex number, containing information on wave amplitude and phase. The advantage is that wave propagation problems can be solved algebraically, rather than through differential equations.

Voltage waveforms in a transmission line move at a velocity $v = 1/\sqrt{\varepsilon\mu}$ along the line. A harmonic disturbance in a transmission line may have components that travel in the positive or negative directions. A single-frequency voltage oscillation measured by a stationary observer has the form

$$V(z,t) = V_+ \exp[j\omega(t - z/v)] + V_- \exp[j\omega(t + z/v)]. \tag{12.59}$$

Equation (12.59) states that points of constant V move along the line at speed v in either the positive or negative z directions. As we found in Section 9.9, the current associated with a wave traveling in either the positive or negative direction is proportional to the voltage. The constant of proportionality is a real number, Z_o. The total current associated with the voltage disturbance of Eq. (12.59) is

$$I(z,t) = (V_+/Z_o) \exp[j\omega(t - z/v)] - (V_-/Z_o) \exp[j\omega(t + z/v)]. \tag{12.60}$$

Note the minus sign in the second term of Eq. (12.60). It is included to preserve the convention that current is positive when positive waves move in the +z direction. A voltage wave with positive voltage moving in the -z direction has negative current. The total impedance at a point is, by definition

$$Z = V(z,t)/I(z,t). \tag{12.61}$$

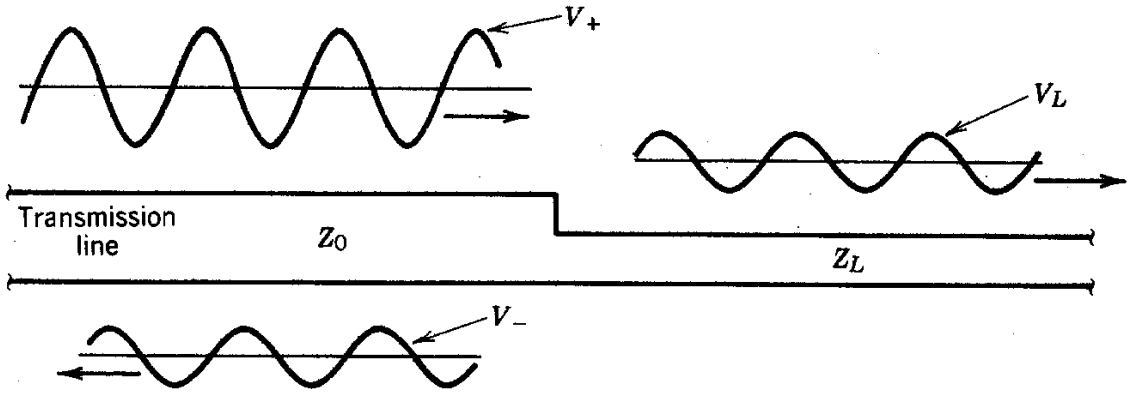

Figure 12.13 Incident, transmitted, and reflected waves at junction of two transmission lines.

If there are components of $V(z,t)$ moving in both the positive and negative directions, Z may not be a real number. Phase differences arise because the sum of V_+ and V_- may not be in phase with the sum of I_+ and I_-.

We will illustrate transmission line properties in the frequency-domain by the calculation of wave reflections at a discontinuity. The geometry is illustrated in Figure 12.13. Two infinite length transmission lines are connected at z = 0. Voltage waves at angular ω frequency travel down the line with characteristic impedance Z_o toward the line with impedance Z_L. If $Z_L = Z_o$, the waves travel onward with no change and disappear down the second line. If $Z_L \neq Z_o$, we must consider the possibility that wave reflections take place at the discontinuity. In this case, three wave components must be included:

1. The incident voltage wave, of form $V_+\exp[j\omega(t-z/v)]$ is specified. The current of the wave is $(V_+/Z_o)\exp[j\omega(t-z/v)]$.

2. Some of the incident wave energy may continue through the connection into the second line. The wave moves in the +z direction and is represented by $V_L\exp[j\omega(t-z/v')]$. The current of the *transmitted wave* is $(V_L/Z_L)\exp[j\omega(t-z/v')]$. There is no negatively directed wave in the second line because the line has infinite length.

3. Some wave energy may be reflected at the connection, leading to a backward-directed wave in the first fine. The voltage and current of the reflected wave are $V_-\exp[j\omega(t-z/v)]$ and $-(V_-/Z_o)\exp[j\omega(t-z/v)]$.

The magnitudes of the transmitted and reflected waves are related to the incident wave and the properties of the lines by applying the following conditions at the connection point ($z = 0$):

1.The voltage in the first line must equal the voltage in the second line at the connection.

2. All charge that flows into the connection must flow out.

The two conditions can be expressed mathematically in terms of the incident, transmitted, and reflected waves.

$$V_+ \exp(j\omega t) + V_- \exp(j\omega t) = V_L \exp(j\omega t), \qquad (12.62)$$

$$(V_+/Z_o) \exp(j\omega t) - (V_-/Z_o) \exp(j\omega t) = (V_L/Z_L) \exp(j\omega t). \qquad (12.63)$$

Canceling the time dependence, Eqs. (12.62) and (12.63) can be solved to relate the reflected and transmitted voltages to the incident voltage:

$$\rho = (V_-/V_+) = (Z_L - Z_o)/(Z_L + Z_o), \qquad (12.64)$$

$$\tau = (V_L/V_+) = 2Z_L/(Z_L + Z_o). \qquad (12.65)$$

Equations (12.64) and (12.65) define the reflection coefficient ρ and the transmission coefficient τ. The results are independent of frequency; therefore, they apply to transmission and reflection of voltage pulses with many frequency, components. Finally, Eqs. (12.64) and (12.65) also hold for reflection and absorption of waves at a resistive termination, because an infinite length transmission line is indistinguishable from a resistor with $R = Z_L$.

A short-circuit termination has $Z_L = 0$. In this case, $\rho = -1$ and $\tau = 0$. The wave is reflected with inverted polarity, in agreement with Section 9.10. There is no transmitted wave. When $Z_L \Rightarrow \infty$ there is again no transmitted wave and the reflected wave has the same voltage as the incident wave. Finally, if $Z_L = Z_o$, there is no reflected wave and $\tau = 1$; the lines are matched.

As a final topic, we consider transformations of impedance along a transmission line. As shown in Figure 12.14, assume there is a load Z_L at $z = 0$ at the end of a transmission line of length l and characteristic impedance Z_o. The load may consist of any combination of resistors, inductors, and capacitors; therefore, Z_L may be a complex number. A power source, located at the point $z = -l$ produces a harmonic input voltage, $V_o \exp(j\omega t)$. The goal is to determine how much current the source must supply in order to support the input voltage. This is equivalent to calculating the impedance $Z(-l)$.

The impedance at the generator is generally different from Z_L. In this sense, the transmission line is an *impedance transformer*. This property is useful for matching power generators to loads that contain reactive elements. In this section, we shall find a mathematical expression for the transformed impedance. In the next section, we shall investigate some of the implications of the result .

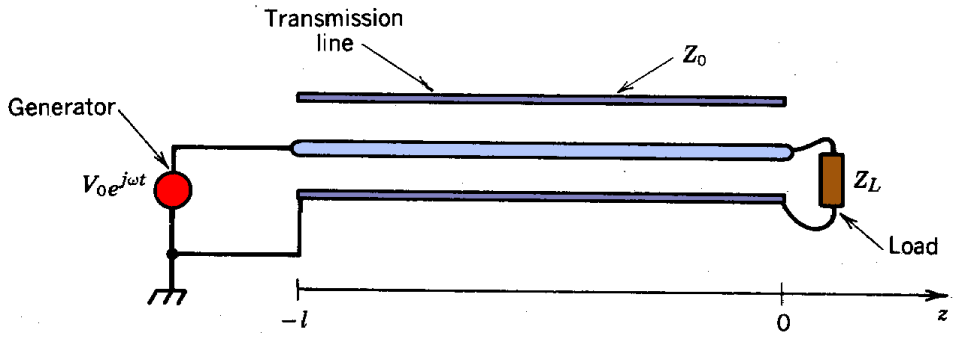

Figure 12.14 Connection of ac voltage generator to a load through transmission line.

Voltage waves are represented as in Eq. (12.59). Both a positive wave traveling from the generator to the load and a reflected wave must be included. All time variations have the form exp(jωt). Factoring out the time dependence, the voltage and current at $z = 0$ are

$$V(0) = V_+ + V_-, \qquad (12.66)$$

$$I(0) = (V_+/Z_o) - (V_-/Z_o). \qquad (12.67)$$

The voltage and current at z = -*l* are

$$V(-l) = V_+ \exp(+jl\omega/v) + V_- \exp(-jl\omega/v), \qquad (12.68)$$

$$I(-l) = (V_+/Z_o) \exp(+jl\omega/v) - (V_-/Z_o) \exp(-jl\omega/v). \qquad (12.69)$$

Furthermore, the treatment of reflections at a line termination [Eq. (12.64)] implies that

$$V_-/V_+ = (Z_L - Z_o)/(Z_L + Z_o). \qquad (12.70)$$

Taking $Z(-l) = V(-l)/I(-l)$, and substituting from q. (12.70), we find that

$$Z(-l) = Z_o \frac{\exp(jl\omega/v) + (Z_L - Z_o)\exp(-l\omega/v)/(Z_L + Z_o)}{\exp(jl\omega/v) - (Z_L - Z_o)\exp(-l\omega/v)/(Z_L + Z_o)}$$

$$= Z_o \frac{Z_L[\exp(jl\omega/v) + \exp(-jl\omega/v)] + Z_o[\exp(jl\omega/v) - \exp(-jl\omega/v)]}{Z_L[\exp(jl\omega/v) - \exp(-jl\omega/v)] + Z_o[\exp(jl\omega/v) + \exp(-jl\omega/v)]} \qquad (12.71)$$

$$= Z_o \frac{Z_L \cos(2\pi l/\lambda) + jZ_o \sin(2\pi l/\lambda)}{Z_o \cos(2\pi l/\lambda) + jZ_L \sin(2\pi l/\lambda)}.$$

where $\omega/v = 2\pi/\lambda$.. In summary, the expressions of Eq. (12.71) give the impedance at the input of a transmission line of length l terminated by a load Z_L.

12.7 TRANSMISSION LINE TREATMENT OF THE RESONANT CAVITY

In this section, the formula for the transformation of impedance by a transmission line [Eq. (12.71)] is applied to problems related to resonant cavities. To begin, consider terminations at the end of a transmission line with characteristic impedance Z_o and length l. The termination Z_L is located at $z = 0$ and the voltage generator at $z = -l$. If Z_L is a resistor with $R = Z_o$, Eq. (1 2.71) reduces to $Z(-l) = Z_o$, independent of the length of the line. In this case, there is no reflected wave, The important property of the matched transmission line is that the voltage wave at the termination is identical to the input voltage wave delayed by time interval l/v. Matched lines are used to conduct diapostic signals without distortion.

Another interesting case is the short-circuit termination, $Z_L = 0$. The impedance at the line input is

$$Z(-l) = jZ_o \tan(2\pi l/\lambda). \tag{12.72}$$

The input impedance is zero when $l = 0, \lambda/2, 3\lambda/2,\ldots$. An interesting result is that the shorted line has infinite input impedance (open circuit) when

$$l = \lambda/4, 3\lambda/4, 5\lambda/4,... \tag{12.73}$$

A line with length given by Eq. (12.73) is called a *quarter wave line*.

Figure 12.15 illustrates the analogy between a cylindrical resonant cavity and a quarter wave line. A shorted radial transmission line of length l has power input at frequency ω at the inner diameter., Power flow is similar to that of Figure 12.2. If the frequency of the input power matches one of the resonant frequencies of the line, then the line has an infinite impedance and power is transferred completely to the load on axis. The resonant frequencies of the radial transmission line are

$$\omega_1 = \pi v/2l, \qquad \omega_2 = 3\pi v/2l, \qquad \omega_1 = 5\pi v/2l, \ \ldots\ . \tag{12.74}$$

These frequencies differ somewhat from those of Table 12.1 because of geometric differences between the cavities.

The quarter wave line has positive and negative-going waves. The positive wave reflects at the short-circuit termination giving a negative-going wave with 180° phase shift. The voltages of the waves subtract at the termination and add at the input ($z = -l$). The summation of the voltage waves is a standing-wave pattern:

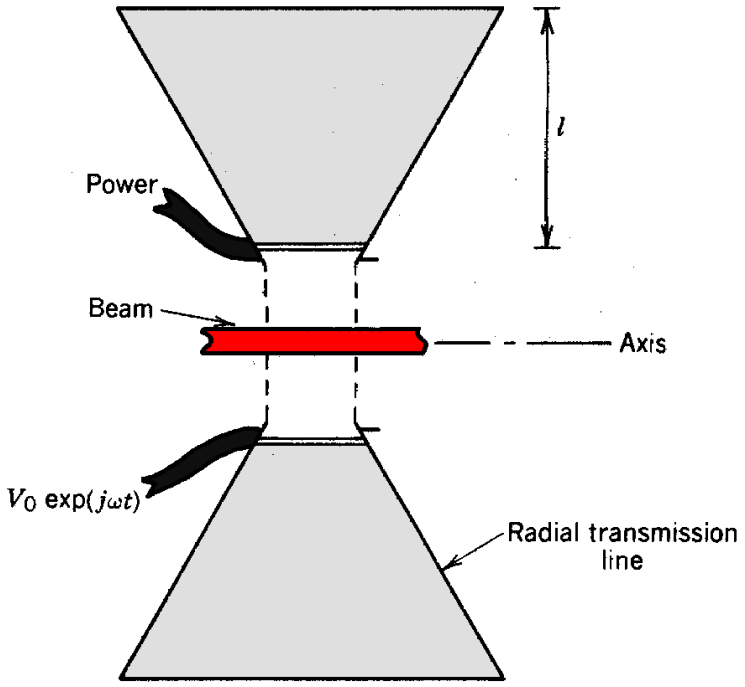

Figure 12.15 Resonant acceleration cavity formed from shorted radial transmission line.

$$V(z,t) = V_0 \sin(-\pi z/2l) \exp(j\omega t).$$

At resonance, the current of the two waves at z = l is equal and opposite. The line draws no current and has infinite impedance. At angular frequencies below ω_1, inspection of Eq. (12.72) shows that $Z \sim +j$; thus, the shorted transmission line acts like an inductor. For frequencies above w_1, the line has $Z \sim -j$; it acts as a capacitive load. This behavior repeats cyclically about higher resonant frequencies.

A common application of transmission lines is power matching from a harmonic voltage generator to a load containing reactive elements. We have already studied one example of power matching, coupling of energy into a resonant cavity by a magnetic loop (Section 12.5). Another example is illustrated in Figure 12.16. An ac generator drives an acceleration gap. Assume, for simplicity, that the beam load is modeled as a resistor R. The generator efficiency is optimized when the total load is resistive. If the load has reactive components, the generator must supply displacement currents that lead to internal power dissipation. Reactances have significant effects at high frequency. For instance, displacement current is transported through the capacitance between the electrodes of the accelerating gaps, C_g. The displacement current is comparable to the load current when $\omega \sim 1/RC_g$. In principle, it is unnecessary for the power supply to support displacement currents because energy is not absorbed by reactances. The strategy is to add circuit elements than can support the reactive current, leaving the generator to supply power only to the

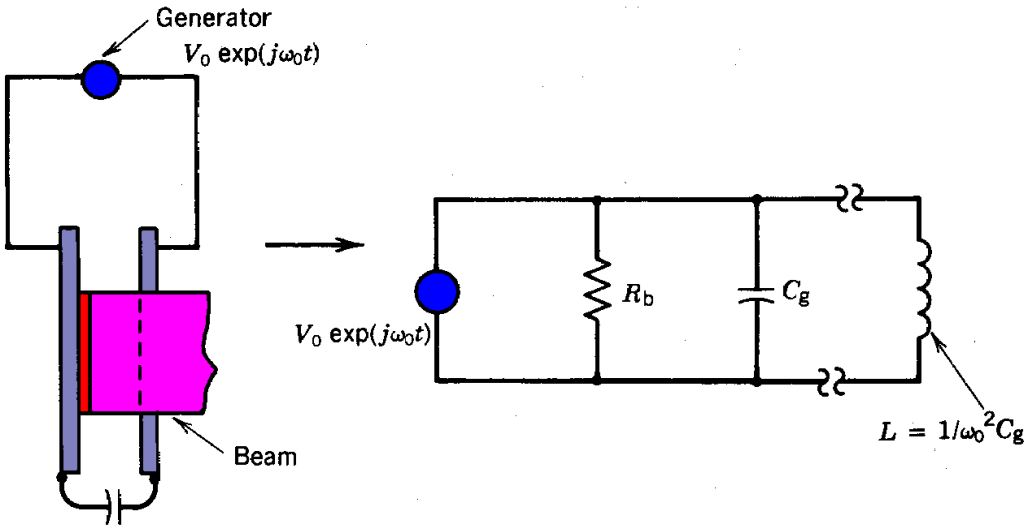

Figure 12.16 Power matching of harmonic generators to loads with reactive and resistive components. Geometry and equivalent circuit of acceleration gap at high frequency.

resistive load. This is accomplished in the acceleration gap by adding a shunt inductance with value $L = 1/\omega_o^2 C_g$, where ω_o is the generator frequency. The improvement of the Wideroe linac by the addition of resonant cavities (Section 14.2) is an example of this type of matching.

Section 12.5 shows that a coupling loop in a resonant cavity is a resistive load at the driving frequency if the proper shunt capacitance is added. Matching can also be accomplished by adjusting the length of the transmission line connecting the generator to the loop. At certain values of line length, the reactances of the transmission line act in concert with the reactances of the loop to support displacement current internally. The procedure for finding the correct length consists of adjusting parameters in Eq. (12.71) with Z_1 equal to the loop impedance until the imaginary part of the right-hand side is equal to zero. In this circumstance, the generator sees a purely resistive load. The search for a match is aided by use of the Smith chart; the procedure is reviewed in most texts on microwaves.

12.8 WAVEGUIDES

Resonant cavities have finite extent in the axial direction. Electromagnetic waves are reflected at the axial boundaries, giving rise to the standing-wave patterns that constitute resonant modes. We shall remove the boundaries in this section and study electromagnetic oscillations that travel in the axial direction. A structure that contains a propagating electromagnetic wave is called a *waveguide*. Consideration is limited to metal structures with uniform cross section and infinite extent in the z direction. In particular, we will concentrate on the cylindrical waveguide, which is simply a hollow tube.

Waveguides transport electromagnetic energy. Waveguides are often used in accelerators to couple power from a microwave source to resonant cavities. Furthermore, it is possible to transport particle beams in a waveguide in synchronism with the wave phase velocity so that they continually gain energy. Waveguides used for direct particle acceleration must support slow waves with phase velocity equal to or less than the speed of light. Slow-wave structures have complex boundaries that vary periodically in the axial direction; the treatment of slow waves is deferred to Section 12.9.

Single-frequency waves in a guide have fields of the form $\exp[j(\omega t - kz)]$ or $\exp[j(\omega t + kz)]$. Electromagnetic oscillations move along the waveguide at velocity ω/k. In contrast to transmission lines, waveguides do not have a center conductor. This difference influences the nature of propagating waves in the following ways:

1. The phase velocity in a waveguide varies with frequency. A structure with frequency-dependent phase velocity exhibits *dispersion*. Propagation in transmission lines is dispersionless.

2. Waves of. any frequency can propagate in a transmission line. In contrast, low-frequency waves cannot propagate in a waveguide. The limiting frequency is called the *cutoff frequency*.

3. The phase velocity of waves in a waveguide is greater than the speed of light. This does not violate the principles of relativity since information can be carried only by modulation of wave amplitude or frequency. The propagation velocity of frequency modulations is the group velocity, which is always less than the speed of light in a waveguide.

The properties of waveguides are easily demonstrated by a lumped circuit element analogy. We can generate a circuit model for a waveguide by starting from the transmission line model introduced in Section 9.9. A coaxial transmission line is illustrated in Figure 12.17a. At frequencies low compared to $1/(R_o - R_i)\sqrt{\varepsilon\mu}$, the field pattern is the familiar one with radial electric fields and azimuthal magnetic fields. This field is a TEM (transverse electric and magnetic) mode; both the electric and magnetic fields are transverse to the direction of propagation. Longitudinal current is purely real, carried by the center conductor. Displacement current flows radially; longitudinal voltage differences result from inductive fields. The equivalent circuit model for a section of line is shown in Figure 12.17a.

The field pattern may be modified when the radius of the center conductor is reduced and the frequency is increased. Consider the limit where the wavelength of the electromagnetic disturbance, $\lambda = 2\pi/k$, is comparable to or less than the outer radius of the line. In this case, voltage varies along the high-inductance center conductor on a length scale $\leq R_o$. Electric field lines may directly connect regions along the outer conductor (Fig. 12.17b). The field pattern is no longer a TEM mode because there are longitudinal components of electric field. Furthermore, a portion of the longitudinal current flow in the transmission line is carried by displacement current. An equivalent circuit model for the coaxial transmission line at high frequency is shown in Figure

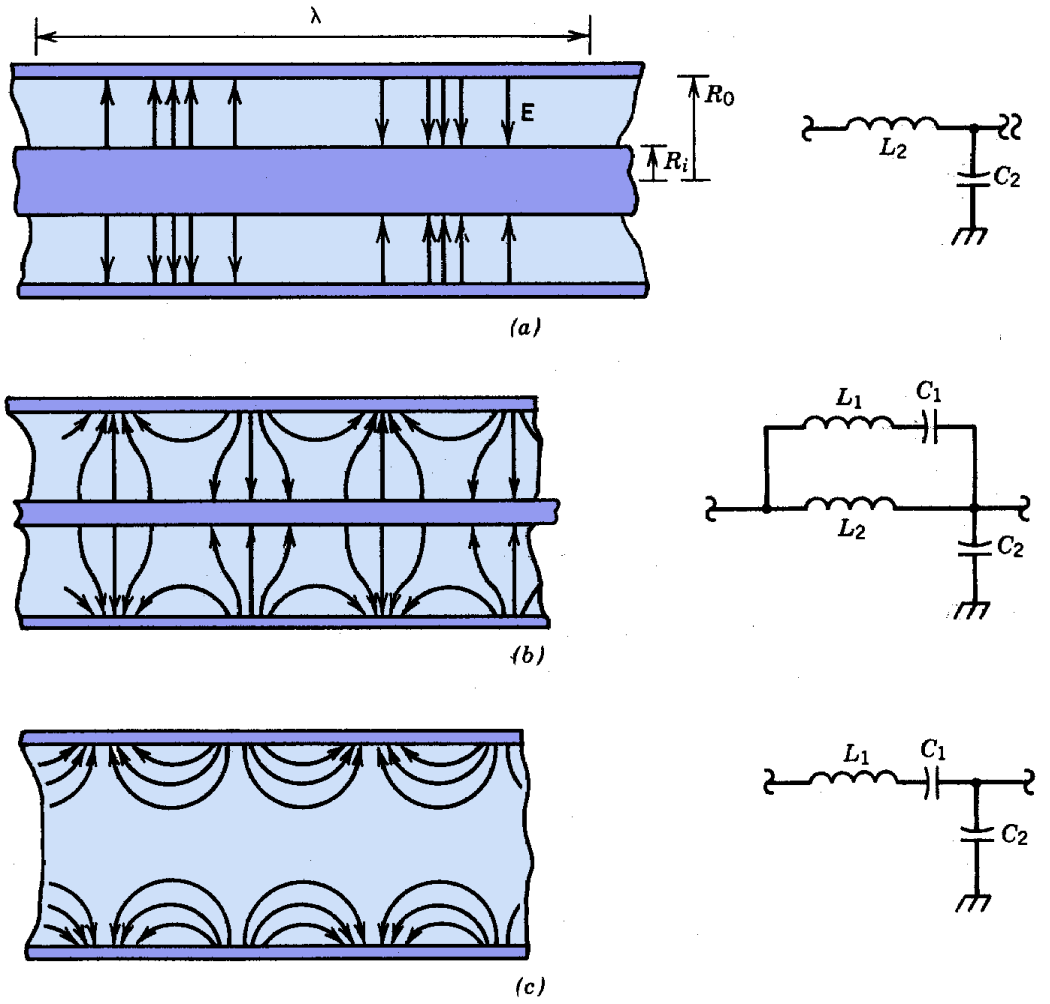

Figure 12.17 Propagating waves in coaxial transmission lines and circular waveguides, electric field patterns, and equivalent circuits. (*a*) TEM mode in transmission line, low frequency. (*b*) TM mode in transmission line, high frequency. (*c*) TM_{10} mode in waveguide.

12.17b. The capacitance between the inner and outer conductors, C_2, is reduced. The flow of real current through inductor L_2 is supplemented by axial displacement current through the series combination of C_1 and L_1. The inductance L_1 is included because displacement currents generate magnetic fields.

As the diameter of the center conductor is reduced, increasing L_2, a greater fraction of the axial current is carried by displacement current. The limit where $R_i \Rightarrow 0$ is illustrated in Figure 12.17c. All axial current flow is via displacement current; L_2 is removed from the mode. The field pattern and equivalent circuit model are shown. We can use the impedance formalism to find the appropriate wave equations for the circuit of Figure 12.17c. Assume that there is a wave moving in the + z direction and take variations of voltage and current as

$$V = V_+ \exp[j(\omega t - kz)] \qquad \textit{and} \qquad I = I_+ \exp[j(\omega t - kz)].$$

The waveguide is separated into sections of length Δz. The inductance of a section is $l_1 \Delta z$ where l_1 is the inductance per unit length. The quantity C_2 equals $c_2 \Delta z$, where c_2 is the shunt capacitance per unit length in farads per meter. The series capacitance is inversely proportional to length, so that $C_1 = c_1 \Delta z$, where c_1 is the series capacitance of a unit length. The quantity c_1 has units of farad-meters. The voltage drop across an element is the impedance of the element multiplied by the current or

$$\Delta V = -I\ (-j\Delta z/\omega c_1 + j\omega l_1 \Delta z),$$

or

$$\partial V/\partial z = -(-j/\omega c_1 + j\omega l_1)\ I \tag{12.76}$$

The change in longitudinal current occurring over an element is equal to the current that is lost through C_2 to ground

$$\Delta I = -jc_2 \Delta z \omega\ V,$$

or

$$\partial I/\partial z = -j\omega c_2\ V. \tag{12.77}$$

Equations (12.76) and (12.77) can be combined to the single-wave equation

$$\partial^2 V/\partial z^2 = -k^2\ V = j\omega c_2\ (-j/\omega c_1 + j\omega l_1)\ V = (c_2/c_1 - \omega^2 l_1 c_2)\ V. \tag{12.78}$$

Solving for k and letting $\omega_c = 1/\sqrt{l_1 c_1}$, we find that

$$k = \sqrt{c_2/c_1}\ \sqrt{\omega^2/\omega_c^2 - 1}. \tag{12.79}$$

Equation (12.79) relates the wavelength of the electromagnetic disturbance in the cylindrical waveguide to the frequency of the waves. Equation (12.79) is a dispersion relationship. It determines the phase velocity of waves in the guide as a function of frequency:

$$\omega/k = \sqrt{c_1/c_2}\ \omega_c\ /\ \sqrt{1 - \omega_c^2/\omega^2}.$$

Note that the phase velocity is dispersive. It is minimum at high frequency and approaches infinity as $\omega \Rightarrow \omega_c$. Furthermore, there is a *cutoff frequency*, ω_c, below which waves cannot propagate. The wavenumber is imaginary below ω_c. This implies that the amplitude of low-frequency waves decreases along the guide. Low-frequency waves are reflected near the input of the waveguide; the waveguide appears to be a short circuit.

The above circuit model applies to a propagating wave in the TM_{01} mode. The term TM refers to the fact that magnetic fields are transverse; only electric fields have a longitudinal component. The leading zero indicates that there is azimuthal symmetry; the 1 indicates that the mode has the simplest possible radial variation of fields. There are an infinite number of higher-order modes that can occur in a cylindrical transmission line. We will concentrate on the TM_{01} mode because it has the optimum field variations for particle acceleration. The mathematical methods can easily be extended to other modes. We will now calculate properties of azimuthally symmetric modes in a cylindrical waveguide by direct solution of the field equations. Again, we seek propagating disturbances of the form

$$\boldsymbol{E}(r,\theta,z,t) = \boldsymbol{E}(r,\theta)\ \exp[j(\omega t - kz)], \qquad (12.80)$$

$$\boldsymbol{B}(r,\theta,z,t) = \boldsymbol{B}(r,\theta)\ \exp[j(\omega t - kz)]. \qquad (12.81)$$

With the above variation and the condition that there are no free charges or current in the waveguide, the Maxwell equations [Eqs. (3.11) and (3.12)] are

$$\nabla \times \boldsymbol{E} = -j\omega \boldsymbol{B}, \qquad (12.82)$$

$$\nabla \times \boldsymbol{B} = -j\omega\varepsilon\mu \boldsymbol{E}. \qquad (12.83)$$

Equations (12.82) and (12.83) can be combined to give the two wave equations

$$\nabla^2 \boldsymbol{E} = -k_o^2\ \boldsymbol{E}, \qquad (12.84)$$

$$\nabla^2 \boldsymbol{B} = -k_o^2\ \boldsymbol{B}. \qquad (12.85)$$

where $k_o = \sqrt{\varepsilon\mu}\ \omega = \omega/v$.

The quantity k_o is the *free-space wavenumber*; it is equal to $2\pi/\lambda_o$, where λ_o is the wavelength of electromagnetic waves in the filling medium of the waveguide in the absence of the boundaries.

In principle, either Eq. (12.84) or (12.85) could be solved for the three components of **E** or **B**, and then the corresponding components of **B** or **E** found through Eq. (12.82) or (12.83). The process is complicated by the boundary conditions that must be satisfied at the wall radius, R_o:

$$E_{\parallel}(R_o) = 0, \qquad (12.86)$$

$$B_{\perp}(R_o) = 0. \qquad (12.87)$$

Equations (12.86) and (12.87) refer to the vector sum of components; the boundary conditions couple the equations for different components. An organized approach is necessary to make the calculation tractable.

We will treat only solutions with azimuthal symmetry. Setting $\partial/\partial\theta = 0$, the component forms of Eqs. (12.82) and (12.83) are

$$jkE_\theta = -j\omega B_r, \qquad (12.88)$$

$$(1/r)\ \partial(rE_\theta)/\partial r = -j\omega B_z, \qquad (12.89)$$

$$-jkE_r - \partial E_z/\partial r = -j\omega B_\theta, \qquad (12.90)$$

$$jkB_\theta = -j(k_o^2/\omega)\ E_r, \qquad (12.91)$$

$$(1/r)\ \partial(rB_\theta)/\partial r = -j(k_o^2/\omega)\ E_z, \qquad (12.92)$$

$$-jkB_r - \partial B_z/\partial r = -j(k_o^2/\omega)\ E_\theta. \qquad (12.93)$$

These equations can be manipulated algebraically so that the transverse fields are proportional to derivatives of the longitudinal components:

$$B_r = -jk\ (\partial B_z/\partial r)\ /\ (k_o^2 - k^2), \qquad (12.94)$$

$$E_r = -jk\ (\partial E_z/\partial r)\ /\ (k_o^2 - k^2), \qquad (12.95)$$

$$B_\theta = -j(k^2/\omega)\ (\partial E_z/\partial r)\ /\ (k_o^2 - k^2), \qquad (12.96)$$

$$E_\theta = -j\omega\ (\partial B_z/\partial r)\ /\ (k_o^2 - k^2). \qquad (12.97)$$

Notice that there is no solution if both B_z and E_z equal zero; a waveguide cannot support a TEM mode. Equations (12.94)-(12.97) suggest a method to simplify the boundary conditions on the wave equations. Solutions are divided into two categories: waves that have $E_z = 0$ and waves that have $B_z = 0$. The first type is called a TE wave, and the second type is called a TM wave. The first type has transverse field components B_r and E_θ. The only component of magnetic field perpendicular to the metal wall is B_r. Setting $B_r = 0$ at the wall implies the simple, decoupled

boundary condition

$$\partial B_z(R_o)/\partial r = 0. \tag{12.98}$$

Equation (1 2.98) implies that $E_\theta(R_o) = 0$ and $B_r(R_o) = 0$. The wave equation for the axial component of **B** [Eq. (12.85)] can be solved easily with the above boundary condition. Given B_z, the other field components can be calculated from Eqs. (12.94) and (12.97).

For TM modes, the transverse field components are E_r and B_θ. The only component of electric field parallel to the wall is E_z so that the boundary condition is

$$E_z(R_o) = 0. \tag{12.99}$$

Equation (12.84) can be used to find E_z; then the transverse field components are determined from Eqs. (12.95) and (12.96). The solutions for TE and TM waves are independent. Therefore, any solution with both E_z and B_z can be generated as a linear combination of TE and TM waves. The wave equation for E_z of a TM mode is

$$\nabla^2 E_z = (1/r)\ (\partial/\partial r)\ (\partial E_z/\partial r) - k^2 E_z = -k_o^2\ E_z, \tag{12.100}$$

with $E_z(R_o) = 0$. The longitudinal contribution to the Laplacian follows from the assumed form of the propagating wave solution. Equation (12.100) is a special form of the Bessel equation. The solution is

$$E_z(r,z,t) = E_o\ J_0\left(\sqrt{k_o^2 - k^2}\,r\right) \exp[j(\omega t - kz)] \tag{12.101}$$

The boundary condition of Eq. (12.99) constraints the wavenumber in terms of the free-space wavenumber:

$$k_o^2 - k^2 = x_n^2/R_o^2, \tag{12.102}$$

where $x_n = 2.405, 5.520, \ldots$. Equation (12.102) yields the following dispersion relationship for TM_{0n} modes in a cylindrical waveguide:

$$k = \sqrt{\varepsilon\mu\omega^2 - x_n^2/R_o^2}, \tag{12.103}$$

The mathematical solution has a number of physical implications. First, the wavenumber of low-frequency waves is imaginary so there is no propagation. The cutoff frequency of the TM_{01} mode is

$$\omega_c = 2.405/\sqrt{\varepsilon\mu}R_o. \tag{12.104}$$

Near cutoff, the wavelength in the guide approaches infinity. The free-space wavelength of a TM_{01} electromagnetic wave at frequency ω_c is $\lambda_o \cong 2.61R_o$. The free-space wavelength is about equal to the waveguide diameter; waves with longer wavelengths are shorted out by the metal waveguide walls.

The wavelength in the guide is

$$\lambda = \lambda_o / \sqrt{1 - \omega_c^2/\omega^2}. \tag{12.105}$$

The phase velocity is

$$\omega/k = 1 / \sqrt{\varepsilon\mu}\sqrt{1 - \omega_c^2/\omega^2}. \tag{12.106}$$

Note that the phase velocity in a vacuum waveguide is always greater than the speed of light.

The solution of the field equations indicates that there are higher-order TM_{0n} waves. The cutoff frequency for these modes is higher. In the frequency range $2.405/\sqrt{\varepsilon\mu}R_o$ to $5.520/\sqrt{\varepsilon\mu}R_o$, the only TM mode that can propagate is the TM_{01} mode. On the other hand, a complete solution for all modes shows that the TE_{11} has the cutoff frequency $\omega_c = 1.841/\sqrt{\varepsilon\mu}R_o$ which is lower than that of the TM_{01} mode. Precautions must be taken not to excite the TE_{11} mode because: 1) the waves consume rf power without contributing to particle acceleration and 2) the on-axis radial electric and magnetic field components can cause deflections of the charged particle beam.

12.9 SLOW-WAVE STRUCTURES

The guided waves discussed in Section 12.8 cannot be used for particle acceleration because they have phase velocity greater than c. It is necessary to generate slow waves with phase velocity less than c. It is easy to show that slow waves cannot propagate in waveguides with simple boundaries. Consider, for instance, waves with electric field of the form $\exp[j(\omega t - kz)]$ with $\omega/k < c$ in a uniform cylindrical pipe of radius R_o. Because the wave velocity is assumed less than the speed of light, we can make a transformation to a frame moving at speed $u_z = \omega/k$. In this frame, the wall is unchanged and the wave appears to stand still. In the wave rest frame the electric field is static. Because there are no displacement currents, there is no magnetic field. The electrostatic field must be derivable from a potential. This is not consistent with the fact that the wave is surrounded by a metal pipe at constant potential. The only possible static field solution inside the pipe is $\mathbf{E} = 0$.

Slow waves can propagate when the waveguide has periodic boundaries. The properties of slow

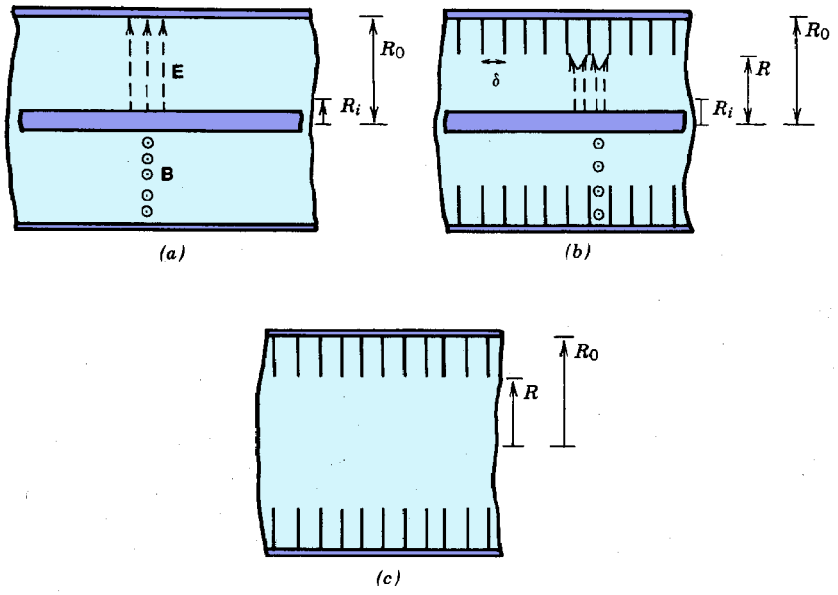

Figure 12.18 Slow-wave structures. (*a*) Electric and magnetic fields of TEM mode in coaxial transmission line. (*b*) Modified TEM mode in coaxial transmission line with capacitive loading. (*c*) Iris-loaded waveguide.

waves can be derived by a formal mathematical treatment of wave solutions in a periodic structure. In this section, we shall take a more physical approach, examining some special cases to understand how periodic structures support the boundary conditions consistent with slow waves. To begin, we consider the effects of the addition of periodic structures to the transmission line of Figure 12.18a. If the region between electrodes is a vacuum, TEM waves propagate with $\omega/k = c$. The line has a capacitance C and inductance L per unit length given by Eqs. (9.71) and (9.72). We found in Section 9.8 that the phase velocity of waves in a transmission line is related to these quantities by

$$\omega/k = 1/\sqrt{LC}. \tag{12.107}$$

Consider reconstructing the line as shown in Figure 12.18b. Annular metal pieces called *irises* are attached to the outer conductor. The irises have inner radius R and spacing δ.

The electric field patterns for a TEM wave are sketched in Figure 12.18b in the limit that the wavelength is long compared to δ. The magnetic fields are almost identical to those of the standard transmission line except for field exclusion from the irises; this effect is small if the irises are thin. In contrast, radial electric fields cannot penetrate into the region between irises. The electric fields are restricted to the region between the inner conductor and inner radius of the irises. The result is that the inductance per unit length is almost unchanged, but C is significantly increased. The capacitance per unit length is approximately

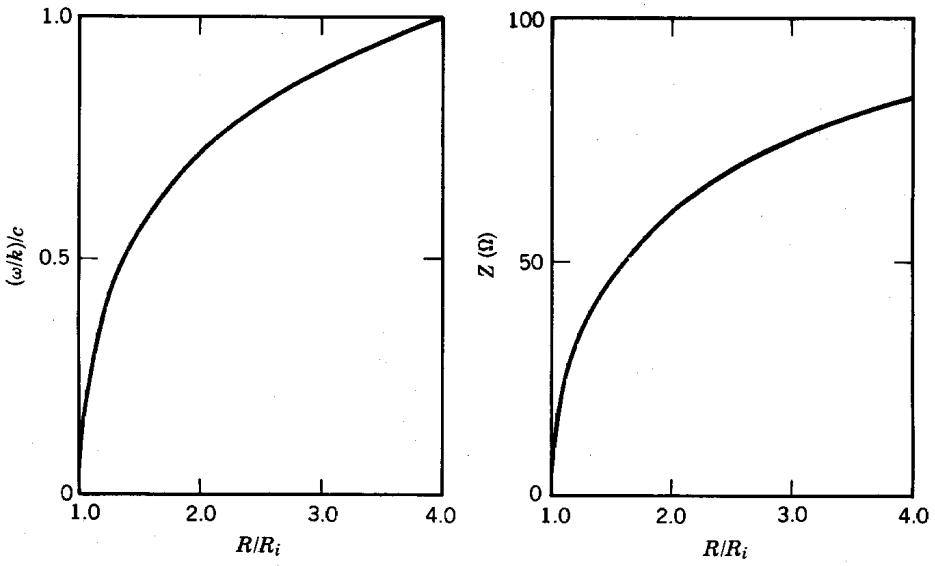

Figure 12.19 Phase velocity and characteristic impedance of capacitively loaded transmission line as function of R/R_i. ($\varepsilon = \varepsilon_0$, $R_i/R_0 = 0.25$).

$$C = 2\pi\varepsilon \;/\; \ln(R/R_i). \tag{12.108}$$

The phase velocity as a function of R/R_o is

$$\omega/k \cong c\sqrt{\ln(R/R_i) \;/\; \ln(R_o/R_i)}. \tag{12.109}$$

The characteristic impedance for TEM waves becomes

$$Z = \sqrt{L/C} = Z_o\sqrt{\ln(R_o/R_i) \;/\; \ln(R/R_i)}. \tag{12.109}$$

The phase velocity and characteristic impedance are plotted in Figure 12.19 as a function of R/R_i. Note the following features:

1.The phase velocity decreases with increasing volume enclosed between the irises.

2.The phase velocity is less than the speed of light.

3.The characteristic impedance decreases with smaller iris inner radius.

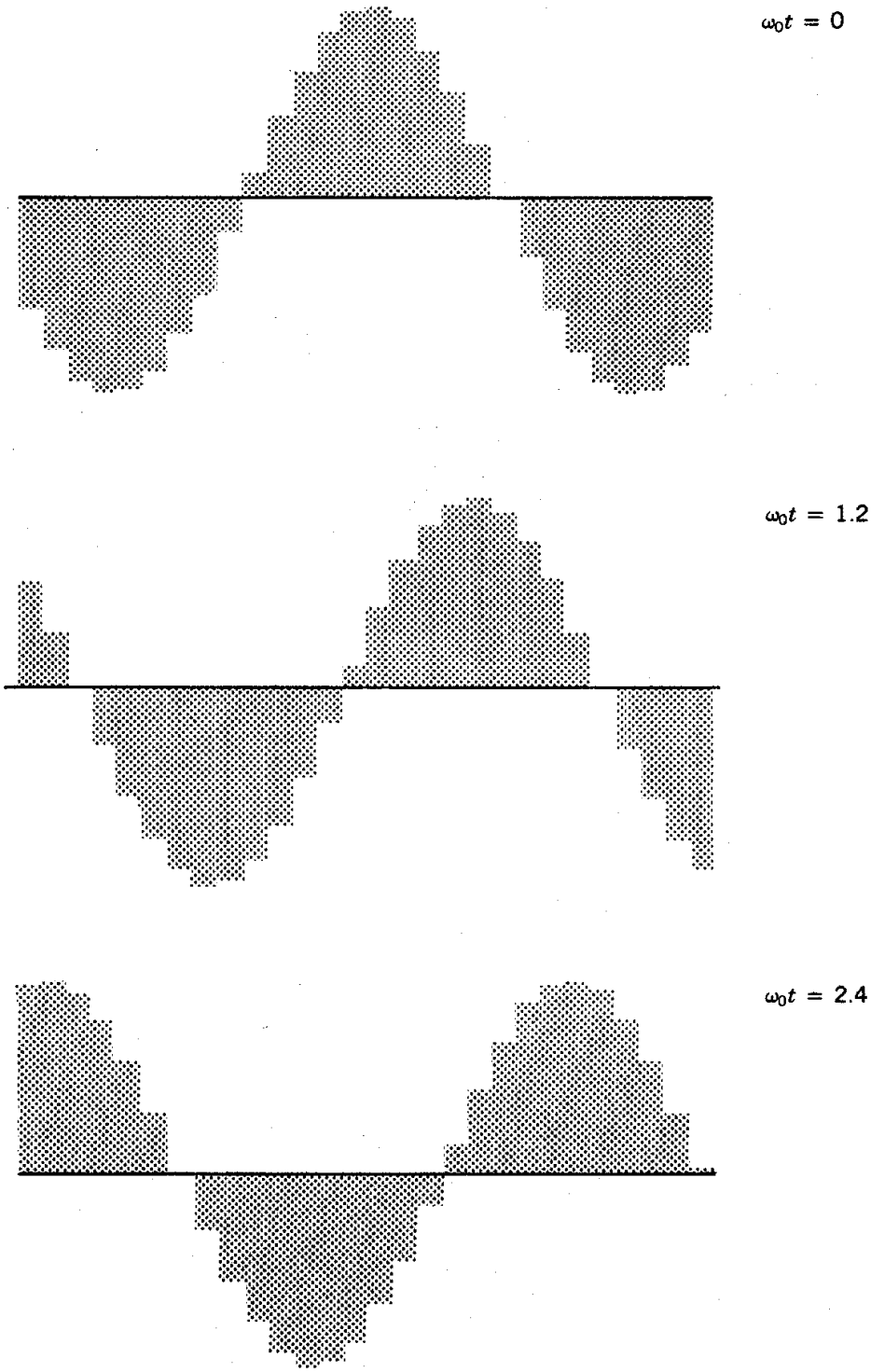

Figure 12.20 Electric field amplitudes in array of individually phased resonant cavities (27 cavities, with oscillations separated by constant phase difference $\Delta\phi = -0.3$ rad). Plots at times given by $\omega_0 t = 0, 1.2, 2.4, 3.6, 4.8, 6$.

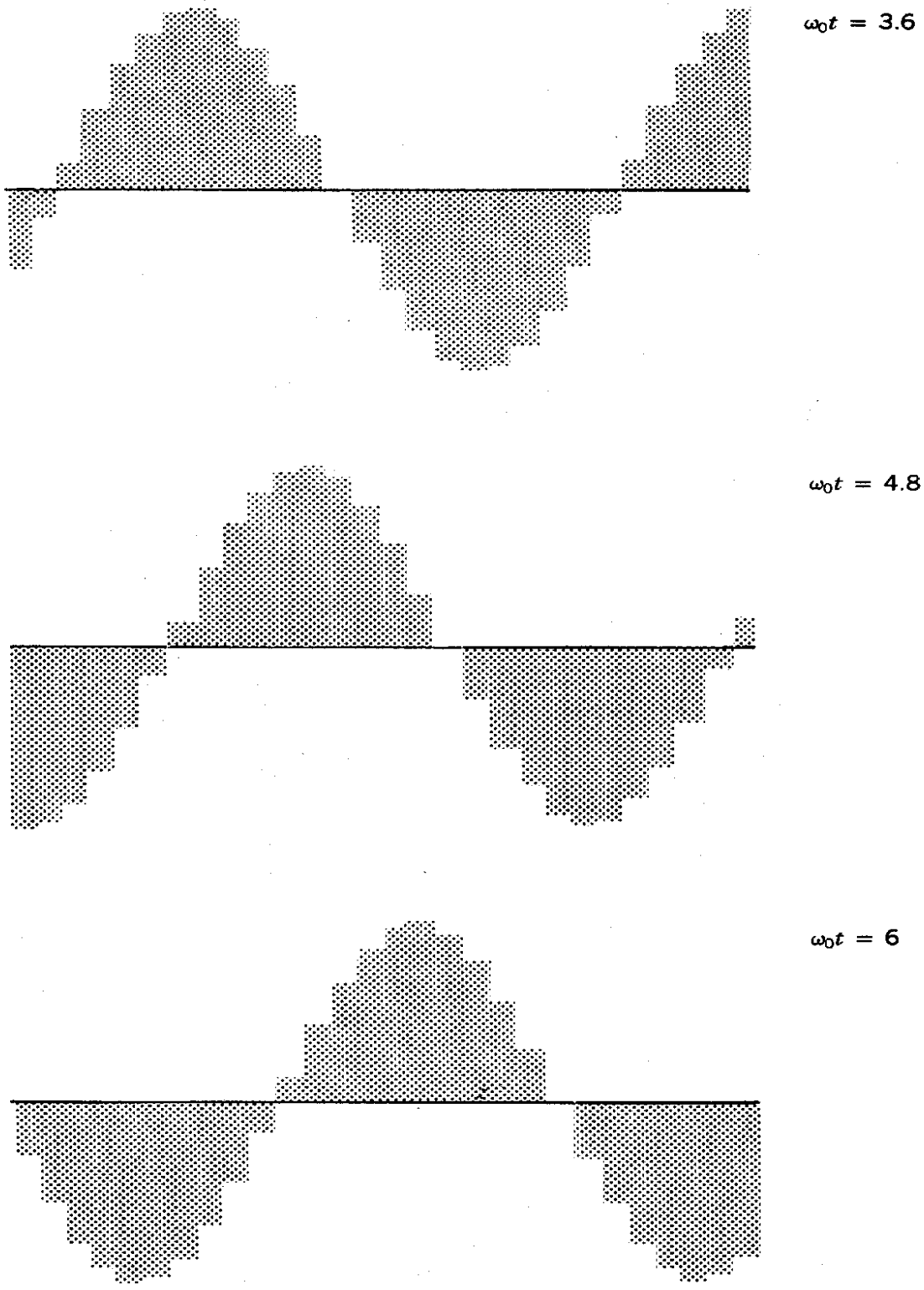

Figure 12.20 (*Continued*).

4.In the long wavelength limit ($\lambda \gg \delta$), the phase velocity is independent of frequency. This is not true when $\lambda \leq \delta$. A general treatment of the capacitively loaded transmission line is given in Section 12.10.

A similar approach can be used to describe propagation of TM_{01} modes in an iris-loaded waveguide (Fig. 12.18c). At long wavelength the inductance L_1 is almost unchanged by the presence of irises, but the capacitances C_1 and C_2 of the lumped element model is increased. The phase velocity is reduced. Depending on the geometry of the irises, the phase velocity may be pulled below c. Capacitive loading also reduces the cutoff frequency ω_c. In the limit of strong loading ($R \ll R_o$), the cutoff frequency for TM_{01} waves approaches the frequency of the TM_{010} mode in a cylindrical resonant cavity of radius R_o.

The following model demonstrates how the irises of a loaded waveguide produce the proper boundary fields to support an electrostatic field pattern in the rest frame of a slow wave. Consider an iris-loaded waveguide in the limit that $R \ll R_o$ (Fig. 12.18c). The sections between irises are similar to cylindrical resonant cavities. A traveling wave moves along the axis through the small holes; this wave carries little energy and has negligible effect on the individual cavities. Assume that cavities are driven in the TM_{010} mode by external power feeds; the phase of the electromagnetic oscillation can be adjusted in each cavity. Such a geometry is called an *individually phased cavity array*. In the limit $\lambda \gg \delta$, the cavity fields at R are almost pure E_z fields. These fields can be matched to the longitudinal electric field of a traveling wave to determine the wave properties.

Assume that δ is longitudinally uniform and that there is a constant phase difference $-\Delta\varphi$ between adjacent cavities. The input voltage has frequency $\omega \cong 2.405c/R_o$. Figure 12.20 is a plot of electric field at R in a number of adjacent cavities separated by a constant phase interval at different times. Observe that the field at a particular time is a finite difference approximation to a sine wave with wavelength

$$\lambda = 2\pi\delta/\Delta\varphi. \tag{12.111}$$

Comparison of plots at different times shows that the waveform moves in the $+z$ direction at velocity

$$v(phase) = \omega_o/k = (2.405/\Delta\varphi)\ (\delta/R_0)\ c. \tag{12.112}$$

The phase velocity is high at long wavelength. A slow wave results when

$$\Delta\varphi \geq 2.405\ \delta/R_0 \qquad or \qquad \lambda < R_0/2.405. \tag{12.113}$$

In the rest frame of a slow wave, the boundary electric fields at R approximate a static sinusoidal field pattern. Although the fields oscillate inside the individual cavities between irises, the electric field at R appears to be static to an observer moving at velocity ω/k. Magnetic fields are confined within the cavities. The reactive boundaries, therefore, are consistent with an axial variation of electrostatic potential in the wave rest frame.

12.10 DISPERSION RELATIONSHIP FOR THE IRIS-LOADED WAVEGUIDE

The dispersion relationship $\omega = \omega(k)$ is an equation relating frequency and wavenumber for a propagating wave. In this section, we shall consider the implications of dispersion relationships for electromagnetic waves propagating in metal structures. We are already familiar with one quantity derived from the dispersion relationship, the phase velocity ω/k. The group velocity v_g is another important parameter. It is the propagation velocity for modulations of frequency or amplitude. Waves with constant amplitude and frequency cannot carry information; information is conveyed by changes in the wave properties. Therefore, the group velocity is the velocity for information transmission. The group velocity is given by

$$v_g = d\omega/dk. \tag{12.114}$$

Equation (12.114) can be derived through the calculation of the motion of a pulsed disturbance consisting of a spectrum of wave components. The pulse is Fourier analyzed into frequency components; a Fourier synthesis after a time interval shows that the centroid of the pulse moves if the wavenumber varies with frequency.

As an example of group velocity, consider TEM electromagnetic waves in a transmission line. Frequency and wavenumber are related simply by $\omega = k/\sqrt{\varepsilon\mu} = kv$. Both the phase and group velocity are equal to the speed of light in the medium. There is no dispersion; all frequency components of a pulse move at the same rate through the line; therefore, the pulse translates with no distortion. Waves in waveguides have dispersion. In this case, the components of a pulse move at different velocities and a pulse widens as it propagates.

The group velocity has a second important physical interpretation. In most circumstances, the group velocity is equal to the flux of energy in a wave along the direction of propagation divided by the electromagnetic energy density. Therefore, group velocity usually characterizes energy transport in a wave.

Dispersion relationships are often represented as graphs of ω versus k. In this section, we shall construct ω-k plots for a number of wave transport structures, including the iris-loaded waveguide. The straight-line plot of Figure 12.21a corresponds to TEM waves in a vacuum transmission line. The phase velocity is the slope of a line connecting a point on the dispersion curve to the origin. The group velocity is the slope of the dispersion curve. In this case, both velocities are equal to c at all frequencies.

Figure 12.21b shows an ω-k plot for waves passing along the axis of an array of individually phased circular cavities with small coupling holes. The curve is plotted for an outer radius of R_0 = 0.3 m and a distance of 0.05 m between irises. The frequency depends only on the cavity properties not the wavelength of the weak coupling wave. Only discrete frequencies correspond ing to cavity resonances are allowed, The reactive boundary conditions for azimuthally symmetric slow waves can be generated by any TM_{0n0} mode. Choice of the relative phase, $\Delta\varphi$, determines k for the propagating wave. Phase velocity and group velocity are indicated in Figure 12.21b. The line

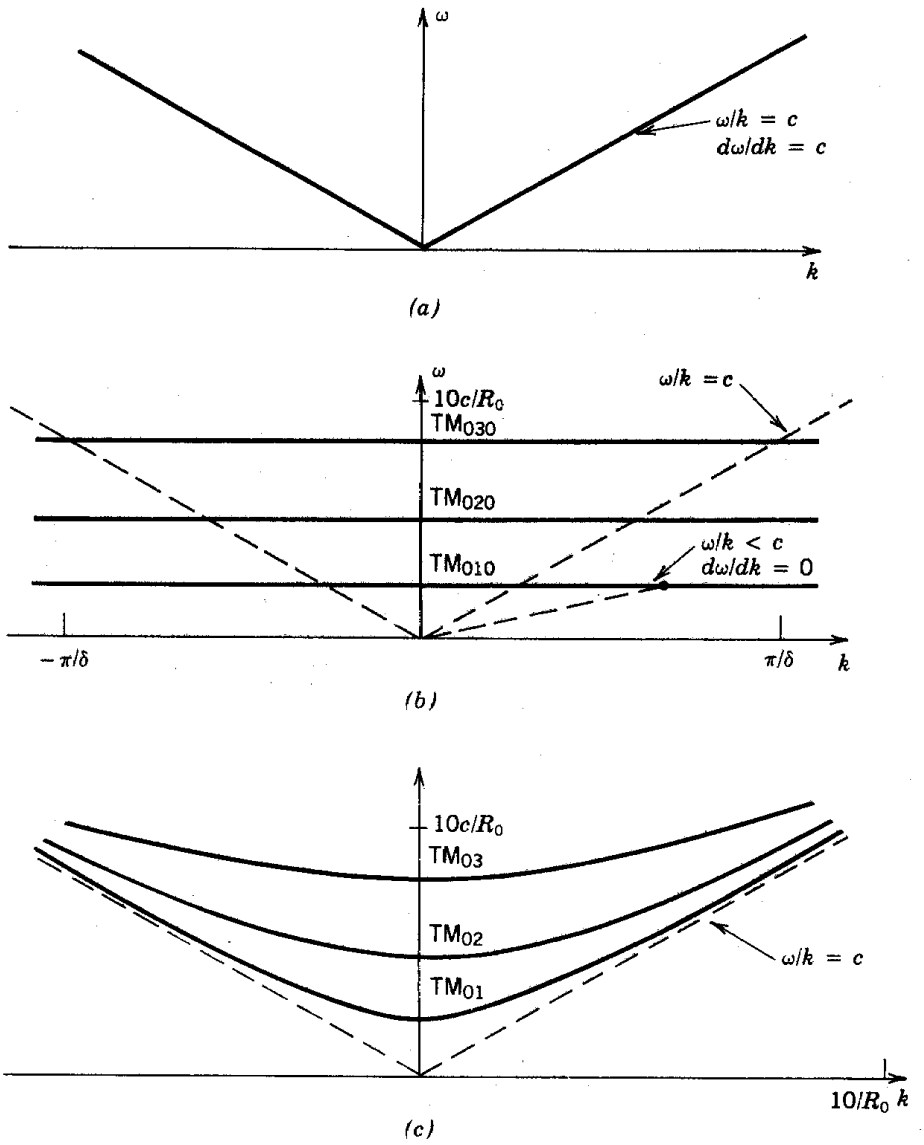

Figure 12.21 Dispersion relationships. (*a*) TEM waves in a transmission line. (*b*) Weakly coupled waves between individually phased cavities with constant phase difference, TM_{0n0} cavity modes. Point indicates possible conditions for a slow wave. (*c*) TM_{0n} modes in a circular waveguide.

corresponding to $\omega/k = c$ has also been plotted. At short wavelengths (large k), the phase velocity can be less than c. Note that since ω is not a function of k, the group velocity is zero. Therefore, the traveling wave does not transport energy between the cavities. This is consistent with the assumption of small coupling holes. The physical model of Section 12.8 is not applicable for wavelengths less than 2δ; this limit has also been indicated on the ω/k graph.

The third example is the uniform circular waveguide. Figure 12.21c shows a plot of Eq. (12.103)

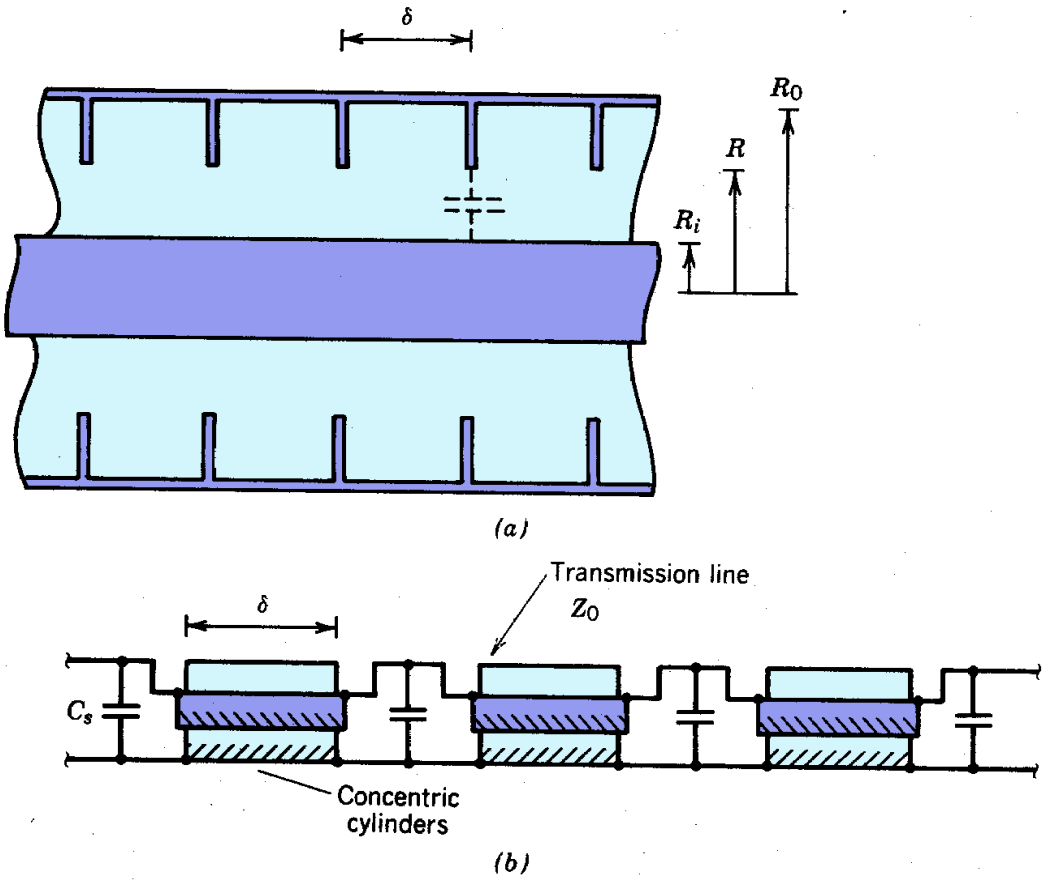

Figure 12.22 Modeling capacitively loaded transmission line as uniform transmission line with periodic shunt capacitance. (*a*) Geometry. (*b*) Equivalent circuit.

for a choice of R_0 = 0.3 m. Curves are included for the TM_{01}, TM_{02}, and TM_{03} modes. Observe that wavenumbers are undefined for frequency less than ω_c. The group velocity approaches zero in the limit that $\omega \Rightarrow \omega_c$,. When $\omega = \omega_c$ energy cannot be transported into the waveguide because k = 0. The group velocity is nonzero at short wavelengths (large k). The boundaries have little effect when $\lambda \ll R$; in this limit, the ω-k plot approaches that of free-space waves, $\omega/k = c$. At long wavelength (small k), the oscillation frequencies approach those of TM_{0n0} modes in an axially bounded cavity with radius R. The phase velocity in a waveguide is minimum at long wavelength; it can never be less than c.

As a fourth example, consider the dispersion relationship for waves propagating in the capacitively loaded transmission line of Figure 12.22a. This example illustrates some general properties of waves in periodic structures and gives an opportunity to examine methods for analyzing periodic structures mathematically. The capacitively loaded transmission line can be considered as a transmission line with periodic impedance discontinuities. The discontinuities arise from the capacitance between the irises and the center conductor. An equivalent circuit is shown in Figure 12.22b; it consists of a series of transmission lines of impedance Z_o and length δ with a

shunt capacitance C_s at the junctions. The goal is to determine the wavenumber of harmonic waves propagating in the structure as a function of frequency. Propagating waves may have both positive-going and negative-going components.

Equations (12.68) and (12.69) can be used to determine the change in the voltage and current of a wave passing through a section of transmission line of length δ. Rewriting Eq. (12.68),

$$\begin{aligned} V(z+\delta) &= = V_+ \exp(-\omega\delta/v) + V_- \exp(\omega\delta/v) \\ &= (V_+ + V_-) \cos(\omega\delta/v) - j\,(V_+ + V_-) \sin(\omega\delta/v) \\ &= V(z) \cos(\omega\delta/v) - jZ_o\, I(z) \sin(\omega\delta/v). \end{aligned} \tag{12.115}$$

The final form results from expanding the complex exponentials [Eq. (12.5)] and applying Eqs. (12.66) and (12.67). A time variation $\exp(j\omega t)$ is implicitly assumed. In a similar manner, Eq. (12.69) can be modified to

$$I(z+\delta) = I(z) \cos(\omega\delta/v) - j\, V(z) \sin(\omega\delta/v)/Z_o. \tag{12.116}$$

Equations (12.115) and (12.116) can be united in a single matrix equation,

$$\begin{pmatrix} V(z+\delta) \\ I(z+\delta) \end{pmatrix} = \begin{bmatrix} \cos(\omega\delta/v) & -jZ_o \sin(\omega\delta/v) \\ -j \sin(\omega\delta/v)/Z_o & \cos(\omega\delta/v) \end{bmatrix} \begin{pmatrix} V(z) \\ I(z) \end{pmatrix} \tag{12.117}$$

The shunt capacitance causes the following changes in voltage and current propagating across the junction:

$$V' = V(z+\delta), \tag{12.118}$$

$$I' = I(z+\delta) - j\omega C_s\, V(z+\delta). \tag{12.119}$$

In matrix notation, Eqs. (12.118) and (12.119) can be written,

$$\begin{pmatrix} V' \\ I' \end{pmatrix} = \begin{bmatrix} 1 & 0 \\ -j\omega C_s & 1) \end{bmatrix} \begin{pmatrix} V(z+\delta) \\ I(z+\delta) \end{pmatrix}. \tag{12.120}$$

The total change in voltage and current passing through one cell of the capacitively loaded transmission line is determined by multiplication of the matrices in Eqs. (12.117) and (12.120):

$$\begin{pmatrix} V' \\ I' \end{pmatrix} = \begin{bmatrix} \cos(\omega\delta/v) & -jZ_o \sin(\omega\delta/v) \\ -j\,[\omega C_s\cos(\omega\delta/v)+\sin(\omega\delta/v)/Z_o] & \cos(\omega\delta/v)-\omega C_s Z_o\sin(\omega\delta/v) \end{bmatrix} \begin{pmatrix} V \\ I \end{pmatrix} \quad (12.117)$$

Applying the results of Section 8.6, the voltage and current at the cell boundaries vary harmonically along the length of the loaded transmission line with phase advance given by $\cos\mu = Tr\boldsymbol{M}/2$, where $\boldsymbol{M}$ is the transfer matrix for a cell [Eq. (12.121)]. If k is the wavenumber of the propagating wave, the phase advance over a cell of length δ is $\mu = k\delta$. Taking the trace of the matrix of Eq. (12.121) gives the following dispersion relationship for TEM waves in a capacitively loaded transmission line:

$$\cos(k\delta) = \cos(\omega\delta/v) - (C_s Z_o v/2\delta)\,(\omega\delta/v)\,\sin(\omega\delta/v). \quad (12.122)$$

Equation (12.122) is plotted in Figure 12.23 for three choices of $(C_s Z_o v/2\delta)$. In the limit of no loading ($C_s = 0$), the dispersion relationship reduces to that of an unloaded line; both the group and phase velocities equal v (the velocity of light in the medium filling the line). With loading, the phase velocity is reduced below v (slow waves). The long wavelength (small k) results agree with the analysis of Section 12.9; the phase velocity and group velocity are independent of frequency. The wave characteristics deviate considerably from those of a TEM wave in an unloaded line when k approaches π/δ. The group velocity approaches zero when $\lambda/2 \Rightarrow \delta$. In this case, the wave is a standing-wave pattern with equal components of positive-going and negative-going waves. The feature is explained below in terms of constructive interference of wave reflections from the line discontinuities. The form of Eq. (12.122) implies that the dispersion plot repeats periodically for higher values of wavenumber.

The final example of a dispersion curve is the iris-loaded waveguide. The ω-k diagram is important in designing traveling wave particle accelerators; the phase velocity must match the particle velocity at all points in the accelerator, and the group velocity must be high enough to transport power through the structure effectively. In this calculation, we will determine how the size of the aperture (R) affects a TM_{01} wave moving through the coupling holes. We will limit attention to the long wavelength limit ($\lambda > 2\delta$). The iris spacing and outer radius are assumed constant. We have already treated two special cases, $R/R_0 = 1$ (uniform circular waveguide) and $R/R_0 = 0$ (independently phased array). Curves for these limits are plotted on Figure 12.24. Consider an intermediate case such as $R/R_0 = 0.5$. At long wavelength, inspection of the curves for the limiting cases infers that the frequency approaches $\omega = 2.405c/R_0$. This behavior can be understood if we consider a long wavelength TM_{01} mode in an ordinary waveguide of radius R_0. The magnetic field is azimuthal, while the electric field is predominantly axial. The addition of thin irises has negligible effect on the electric and magnetic field lines because the oscillating fields induce little net current flow on the irises. In the long wavelength limit, electric fields of the TM_{01} mode are relatively unaffected by the radial metal plates. Current flow induced on the irises by oscillating magnetic field is almost equal and opposite on the upstream and downstream sides. The

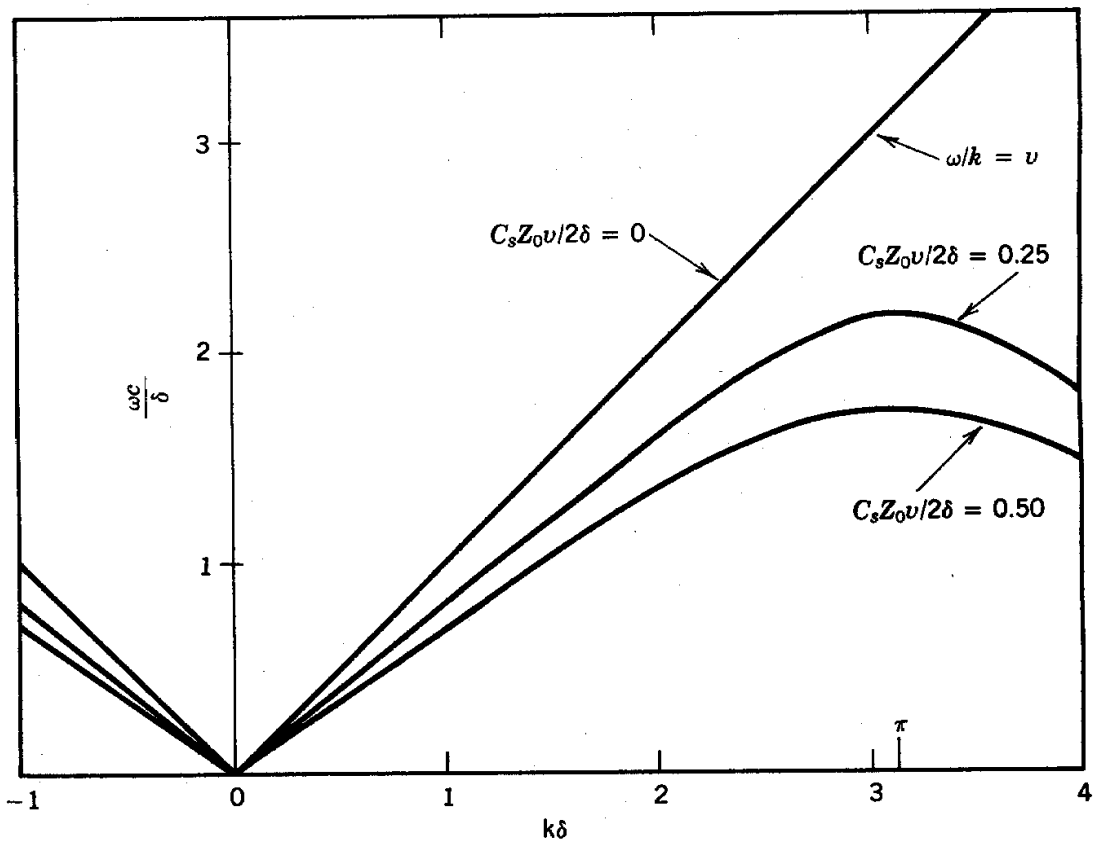

Figure 12.23 Dispersion relationship for capacitively loaded transmission line as function of $C_sZ_0v/2\delta$. C_s, shunt capacitance between iris and inner conductor; Z_0, characteristic impedance of uniform line; v, speed of light in line medium; δ, distance between irises.

only effect is exclusion of magnetic field from the interior of the thin irises.

We can understand the ω-*k* diagram at short wavelengths by approximating the wave as a free-space plane wave. The irises represent discontinuities in the waveguide along the direction of propagation; some of the wave energy may be reflected at the discontinuity. Depending on the geometry, there is the possibility of constructive interference of the reflected waves. To understand this, assume that transmitted and reflected waves are observed at the point $z = 0$. Irises are located at distances δ, 2δ, 3δ, .. ., $n\delta$ downstream. A waveform reaches a particular iris at a time $n\delta/(\omega/k)$ after it passes the point $z = 0$. A reflected wave from the iris takes a time $n\delta/(\omega/k)$ to return to the origin. The sum of reflected waves at z = 0 is therefore

$$E_z(reflected) \sim \sum \exp[j(\omega t - 2\pi\delta k)] = \sum \exp(j\omega t)\cos(2nk\delta). \qquad (12.123)$$

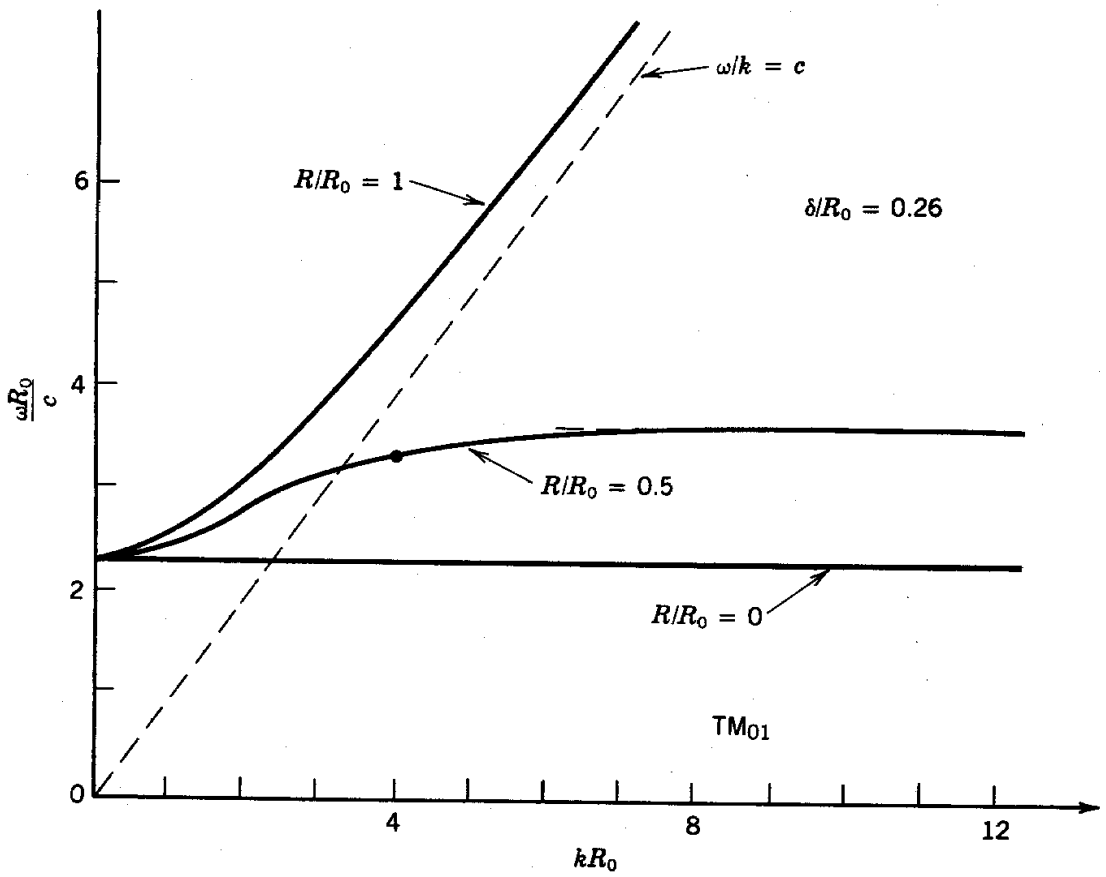

Figure 12.24 Dispersion relationships in the range $0 \le k \le \pi/\delta$ for TM_{01} mode propagation in iris-loaded waveguide of radius R_0 as a function of inner radius of iris, R. $R/R_0 = 0$ corresponds to individually phase cavities, $R/R_0 = 1$ corresponds to circular waveguide. Point indicates slow wave with nonzero group velocity.

The summation of Eq. (12.123) diverges when $k = \pi/\delta$. In this case, there is a strong reflected wave. The final state has equipartition of energy between waves traveling in the +z and -z directions; therefore, a standing-wave pattern with zero group velocity is set up.

We can estimate the frequency of the standing wave at $k = \pi/\delta$ by calculating the resonant frequency of a hollow annular cavity with specified inner radius. In the limit $\delta \ll (R_o - R_i)$, resonant frequencies of TM_{0n0} modes are determined by solving Eq. (12.42) with boundary conditions $E_z(R_o) = 0$ and $B_\theta(R) = 0$. The latter condition comes about because the axial displacement current between $r = 0$ and $r = R$ is small. The boundary condition can be rewritten as $dE_z(R)/dr = 0$. The resonant frequencies are determined by the solutions of the transcendental equation:

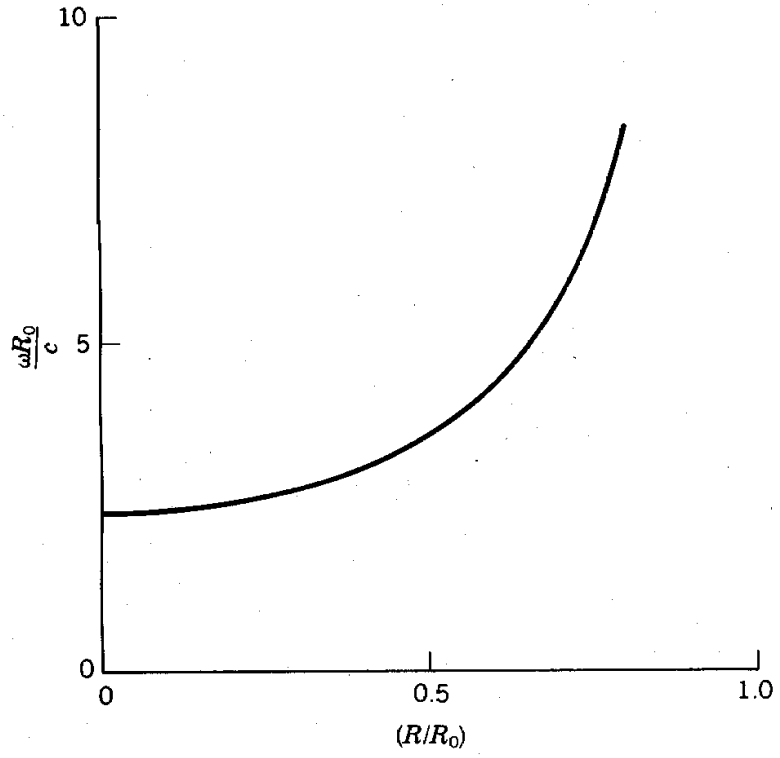

Figure 12.25 Frequency of TM_{010} mode as function of R/R_0 in annular cavity with length d, outer radius R_0, and inner radius R. Open circuit boundary at inner radius; $\delta \ll R$.

$$\frac{J_1(\omega R/c)\ Y_0(\omega R_0/c)}{J_0(\omega R_0/c)\ Y_1(\omega R/c)} = 1 \tag{12.124}$$

Resonant frequencies as a function of R/R_0 are plotted in Figure 12.25 for the TM_{01} and TM_{02} modes. For our example [$R/R_0 = 0.5$], the frequency of the hollow cavity is about 50% higher than that of the complete cavity. This value was incorporated in the plot of Figure 12.24.

Consider some of the implications of Figure 12.24. In the limit of small coupling holes, the cavities are independent. We saw in discussing individually phased cavities that phase velocities much less than the speed of light can be generated by the proper choice of the phasing and δ/R. Although there is latitude to achieve a wide range of phase velocity in the low coupling limit, the low group velocity is a disadvantage. Low group velocity means that energy cannot be coupled between cavities by a traveling wave.

The interdependence of phase and group velocity in a periodic structure enters into the design of rf linear accelerators (Chapter 14). In an accelerator for moderate- to high-energy electrons, the phase velocity is close to c. Inspection of Figure 12.24 shows that this value of phase velocity can

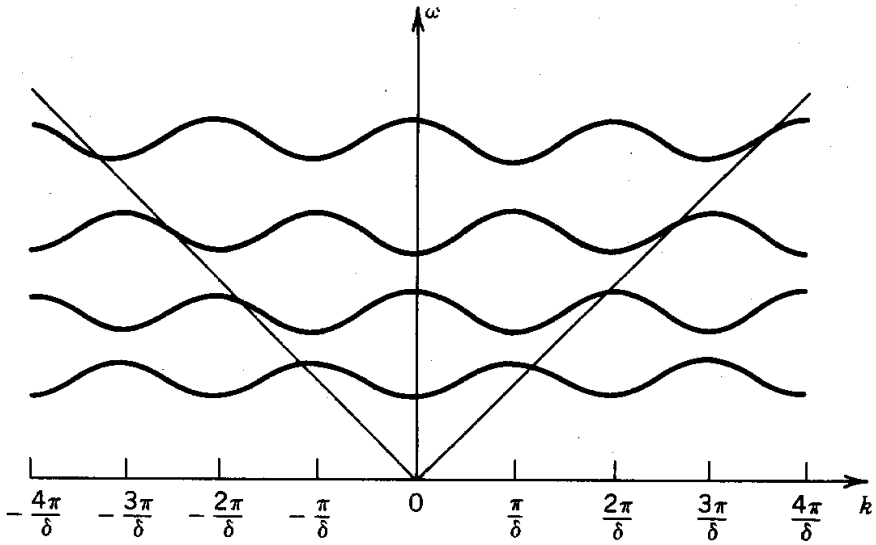

Figure 12.26 Brillouin diagram of wave properties in a capacitively loaded cylindrical waveguide with iris spacing δ.

be achieved in a structure with substantial coupling holes and a high value of group velocity. This means that a useful traveling wave can be excited in an extended structure with nonzero wall resistivity by a single power input. The boundary cavities between irises are excited by energy carried by the traveling wave. This approach is not suitable for linear ion accelerators, where the phase velocity must be well below the speed of light. This is the reason linear ion accelerators generally use external rf coupling of individual cavities to synthesize a slow traveling wave on axis.

In the above derivation, we concentrated on TM_{01} waves over the wavenumher range $0 < k < \pi/\delta$. This is the range generally encountered in accelerator applications. We should recognize, nonetheless, that higher-order modes and traveling waves with $\lambda < 2\delta$ can be propagated. The complete ω-k plot for a periodic waveguide structure is called a *Brillouin diagram* [L. Brillouin. **Wave Propagation in Periodic Structures**, Dover, New York, 1953]. An example is illustrated in Figure 12.26. The periodic repetition of the curve along the k axis is a consequence of the axial periodicity of the waveguide structure. Note the similarities between Figure 12.26 and the dispersion relationship for TEM waves in the capacitively loaded transmission line (Fig. 12.22).

13

Phase Dynamics

The axial electric field at a particular location in an rf accelerator has negative polarity half the time. Particles must move in synchronism with variations of electromagnetic fields in order to be accelerated continuously. Synchronization must be effective over long distances to produce high-energy beams. In this chapter, we shall study the longitudinal dynamics of particles moving in traveling electromagnetic waves. Particle motion is summarized in the phase equations, which describe axial displacements of particles relative to the traveling wave. The phase equations lead to the concept of phase stability [V. Veksler, Doklady U. S. S. R. **44**, 444 (1944); E. M. McMillan, Phys. Rev. **69** 145 (1945). Groups of particles can be confined to the accelerating phase of a wave if they have a small enough spread in kinetic energy. Individual particles oscillate about a constant point in the wave called the synchronous phase.

There are a number of important applications of the phase equations:

1. Injected particles are captured efficiently in an rf accelerator only if particles are introduced at the proper phase of the electromagnetic field. The longitudinal acceptance of an accelerator can by calculated from the theory of longitudinal phase dynamics. A knowledge of the allowed kinetic energy spread of injected particles is essential for designing beam injectors and bunchers.

2. There is a trade-off between accelerating gradient and longitudinal acceptance in an rf accelerator. The theory of longitudinal phase dynamics predicts beam flux limits as a

function of the phase and the properties of the accelerating wave. Effects of space charge can be added to find longitudinal current limits in accelerators.

3. The output from resonant accelerators consists of beam bunches emerging at the frequency of the accelerating wave. Information on the output beam structure is necessary to design debunchers, matching sections to other accelerators, and high-energy physics experiments.

Section 13.1 introduces phase stability. Longitudinal motion is referenced to the hypothetical synchronous particle. Acceleration and inertial forces are balanced for the synchronous particle; it remains at a point of constant phase in a traveling wave. The synchronous particle is the longitudinal analogy of an on-axis particle with no transverse velocity. Particles that deviate in phase or energy from the synchronous particle may either oscillate about the synchronous phase or may fall out of synchronism with the wave. In the former case, the particles are said to be phase stable. Conditions for phase stability are discussed qualitatively in Section 13.1. Equations derived in Section 13.2 give a quantitative description of phase oscillations. The derivation is facilitated by a proof that the fields of all resonant accelerators can be expressed as a sum of traveling waves. Only the wave with phase velocity near the average particle velocity interacts strongly with particles.

T'he phase equations are solved for nonrelativistic particles in Section 13.3 in the limit that changes in the average particle velocity are slow compared to the period of a phase oscillation. The derivation introduces a number of important concepts such as rf buckets, kinetic energy error, and longitudinal acceptance. A second approximate analytic solution, discussed in Section 13.4, holds when the amplitude of phase oscillations is small. The requirement of negligible velocity change is relaxed. The model predicts reversible compression of longitudinal beam bunches during acceleration. The process is similar to the compression of transverse oscillations in the betatron. Longitudinal motion of non-relativistic particles in an induction linac is discussed in Section 13.5. Synchronization is important in the linear induction accelerator even though it is not a resonant device. Pulses of ions must pass through the acceleration gaps during the time that voltage is applied. Section 13.6 discusses longitudinal motion of highly relativistic particles. The material applies to rf electron linacs and linear induction electron accelerators. Solutions of the phase equation are quite different from those for non-relativistic particles. Time dilation is the major determinant of particle behavior. Time varies slowly in the rest frame of the beam relative to the stationary frame. If the electrons in an rf accelerator are accelerated rapidly, they do not have time to perform a phase oscillation before exiting the machine. In some circumstances, electrons can be captured in the positive half-cycle of a traveling wave and synchronously accelerated to arbitrarily high energy. This process is called electron capture. Relativistic effects are also important in linear induction electron accelerators; electron beams remain synchronized even in the presence of large imperfections of voltage waveform.

13.1 SYNCHRONOUS PARTICLES AND PHASE STABILITY

The concept of the synchronous particle and phase stability can be illustrated easily by considering motion in an accelerator driven by an array of independently phased cavities (Fig. 13.1a). Particles receive longitudinal impulses in narrow acceleration gaps. The gaps are spaced equal distances apart; the phase in each cavity is adjusted for the best particle acceleration. Figure 13.lb shows the time variation of gap voltage in a cavity. The time axis is referenced to the beginning of the accelerating half-cycle in gap n.

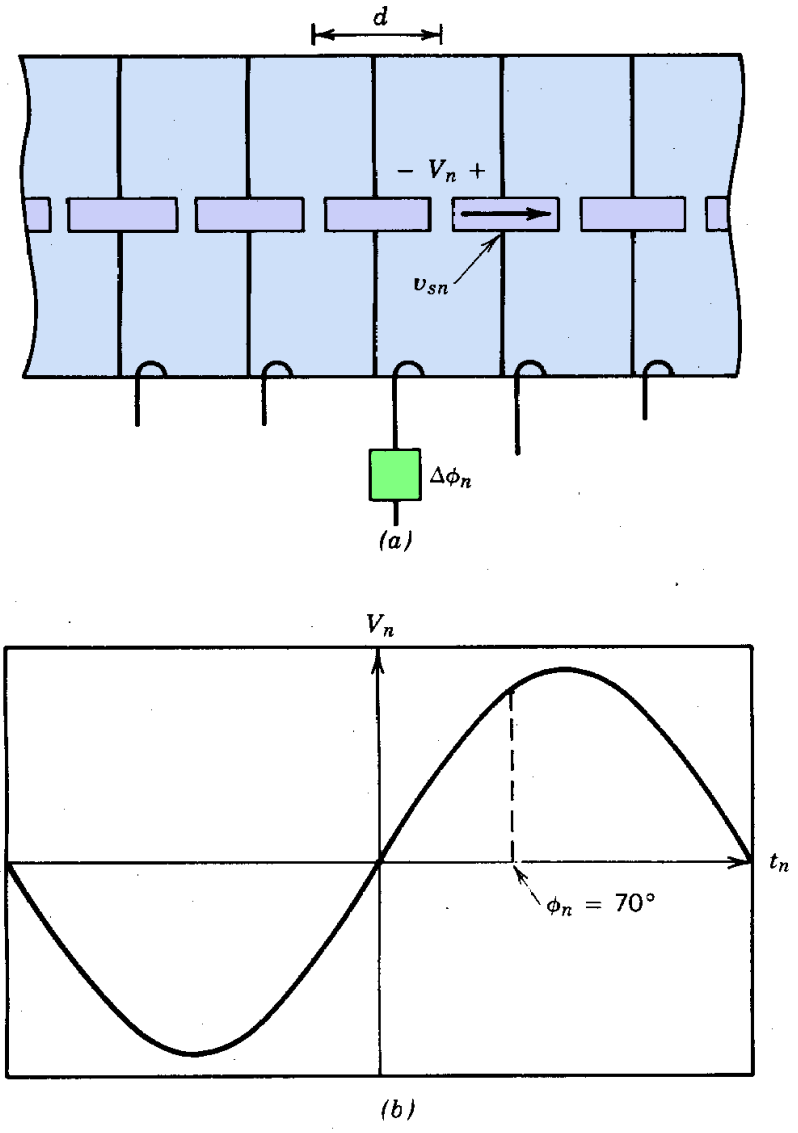

Figure 13.1 Phase of a particle in resonant accelerator. (a) Array of uniform cavities with different rf phase offsets. (b) Definition of phase of particle with respect to time-dependent accelerating voltage in cavity n. Time of crossing of particle with $\phi_n = 70°$ illustrated.

The time at which a test particle crosses gap *n* is indicated in Figure 13.1b. The phase of the particle in defined in terms of the crossing time relative to the cavity waveform. Phase is measured from the beginning of the acceleration half-cycle. Figure 13.lb illustrates a particle with +70° phase. A particle with a phase of +90° crosses at the time of peak cavity voltage; it gains the maximum possible energy. (Note that in many discussions of linear accelerators, the gap fields are assumed to vary as $E_z(t) = E_{zo} \cos\omega t$. Therefore, a synchronous phase value quoted as -32° corresponds to $\varphi_s = 58°$ in the convention used in this book.)

A *synchronous particle* is defined as a particle that has the same phase in all cavities. Crossing times of a synchronous particle are indicated as solid squares in Figure 13.2a. The synchronous phase φ_s is the phase of the synchronous particle. The synchronous particle is in longitudinal equilibrium. Acceleration of the particle in the cavities matches the phase difference of electromagnetic oscillations between cavities so that the particle always crosses gaps at the same relative position in the waveform. A synchronous particle exists only if the frequencies of oscillations in all cavities are equal. If frequency varies, the accelerating oscillations will continually shift relative to each other and the diagram of Figure 13.2a will not hold at all times. Particles are accelerated if the synchronous phase is between 0° and 180°.

An accelerator must be properly designed to fulfill conditions for a synchronous particle. In some accelerators, the phase difference is constant while the distance between gaps is chosen to match particle acceleration. In the present example, the phase of oscillations in individual cavities is adjusted to match the particle mass and average accelerating gradient with the distance between gaps fixed. It is not difficult to determine the proper phase differences for non-relativistic particles. The phase difference between oscillations in cavity *n*+1 and cavity *n* is denoted $\Delta\varphi_{n+1}$. The accelerating voltages in cavities *n* through *n*+2 are defined as

$$\begin{aligned} V_n &= V_o \sin(\omega t), \\ V_{n+1} &= V_o \sin(\omega t + \Delta\varphi_{n+1}), \\ V_{n+1} &= V_o \sin(\omega t + \Delta\varphi_{n+1} + \Delta\varphi_{n+2}), \end{aligned} \tag{13.1}$$

where *t* is the time and ω is the angular rf frequency. By the definition of φ_s, the synchronous particle crosses cavity *n* at time $\omega t = 0$. Assuming non-relativistic ions, the change in synchronous particle velocity imparted by cavity *n* is given by

$$\tfrac{1}{2} m v_{sn}^2 = \tfrac{1}{2} m v_{sn-1}^2 + q V_o \sin\varphi_s, \tag{13.2}$$

where v_{sn} is the particle velocity emerging from gap *n*. The particle arrives at gap *n*+1 at time

(13.3)

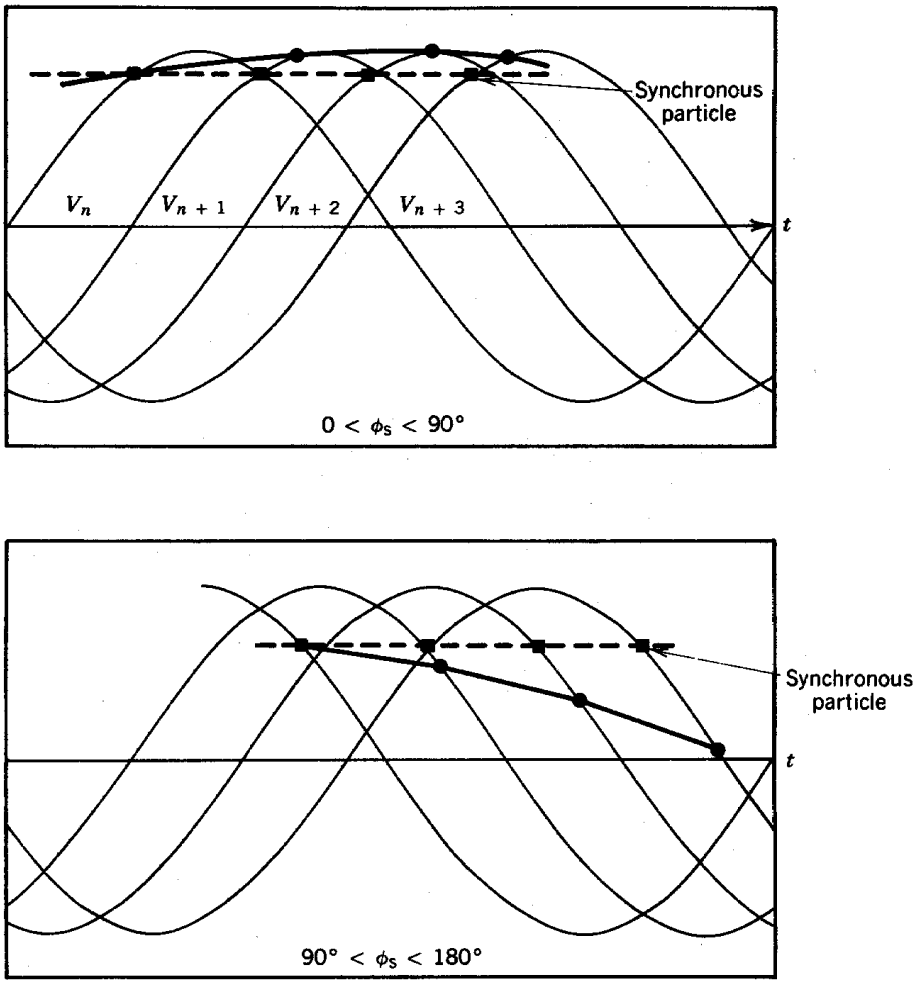

Figure 13.2 Synchronous phase and phase stability. Voltage waveforms illustrated for a number of adjacent acceleration cavities. Squares designate times of crossing for synchronous particle, circles correspond to nonsynchronous particle: (*a*) $0° < \phi_s < 90°$, (*b*) $90° < \phi_s < 180°$.

where d is the distance between gaps. Because the particle is a synchronous particle, the voltage in cavity n+1 equals $V_o \sin\varphi_s$ at time t_{n+1}; therefore, Eq. (13.1) implies that

$$\omega d/v_{sn} + \varphi_s + \Delta\varphi_{n+1} = \varphi_s,$$

or

$$\Delta\varphi_{n+1} = -\omega d/v_{sn}, \tag{13.4}$$

where we have used Eqs. (13.1) and (13.3). Equation (13.4) specifies phase differences between

cavity oscillations. Once V_o and φ_s are chosen, the quantities v_{sn} can be calculated.

Particles injection can never be perfect. Beams always have a spread in longitudinal position and velocity with respect to the synchronous particle. Figure 13.2a illustrates crossing times (circles) for a particle with $v \leq v_s$ with the synchronous phase chosen so that $0° < \varphi_s < 90°$. In the example, the particle crosses cavity *n* at the same time as the synchronous particle. It crosses cavity *n*+1 at a later time; therefore, it sees a higher accelerating voltage than the synchronous particle and it receives a higher velocity increment. The process continues until the particle gains enough velocity to overtake and pass the synchronous particle. In subsequent cavities, it sees reduced voltage and slows with respect to the synchronous particle. The result is that particles with parameters near those of the synchronous particle have stable oscillations about φ_s. These particles constitute a bunch that remains synchronized with accelerating waves; the bunch is *phase stable*.

It is also possible to define a synchronous particle when φ_s is in the range $90° < \varphi_s < 180°$. Such a case is illustrated in Figure 13.2b. The relative phase settings of the cavity are the same as those of Figure 13.2a because the voltages are the same at the crossing time of the synchronous particle. The crossing time history of a particle with $v < v_s$ is also plotted in Figure 13.2b. This particle arrives at cavity *n*+1 later than the synchronous particle and sees a reduced voltage. Its arrival time at the subsequent cavity is delayed further because of its reduced velocity. After a few cavities, the particle moves into the decelerating phase of gap voltage. In its subsequent motion, the particle is completely desynchronized from the cavity voltage oscillations; its axial velocity remains approximately constant.

The conclusion is that particle distributions are not phase stable when the synchronous phase is in the range $90° < \varphi_s < 180°$. The stable range of φ_s for particle acceleration is $0° < \varphi_s < 90°$. Similar considerations apply to charged particle deceleration, an important process for microwave generation. The relative phases of the cavity oscillations can be adjusted to define a decelerating synchronous particle. It can be shown that decelerating bunches have phase stability when $0° < \varphi_s < -90°$. Particle bunches are dispersed when the synchronous phase is in the range $-90° < \varphi_s < -180°$.

Particles accelerated in a traveling electromagnetic wave also can have phase stability. Figure 13.3 shows the electric field as a function of position viewed in the rest frame of a slow wave. The figure illustrates the definition of phase with respect to the wave; the particle shown has $\varphi = +70°$. Figure 13.3 (which shows an electric field variation in space at a constant time) should not be confused with Figure 13.1 (which shows an electric field variation in time at a constant position). Note that the phase definition of Figure 13.3 is consistent with Figure 13.1.

The synchronous particle in a traveling wave is defined by

$$\frac{dp_z}{dt} = eE_o \sin\varphi_s. \tag{13.5}$$

In order for a synchronous particle to exist, the slow-wave structure must be designed so that the

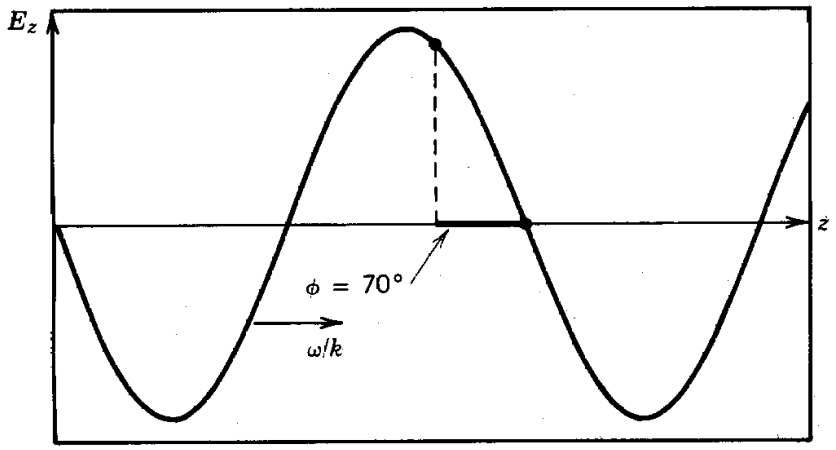

Figure 13.3 Definition of particle phase moving with a traveling wave. Longitudinal electric field plotted as function of position at specific time, position of particle with $\phi = 70°$ indicated.

phase velocity of the wave changes to equal the particle velocity at all points in the accelerator. A slow-wave structure must be designed to accelerate particles with a specific charge-to-mass ratio (Z^*e/m_o) if the accelerating electric field E_o is specified. The above derivations can be modified to show that a particle distribution has phase stability in a traveling wave if the synchronous phase is in the range $0° < \varphi_s < 90°$. (In the convention common to discussions of linear accelerators, the stable phase range is given as $-90° < \varphi_s < 0°$.)

13.2 THE PHASE EQUATIONS

The phase equations describe the relative longitudinal motion of particles about the synchronous particle. The general phase equations are applicable to all resonant accelerators; we shall apply them in subsequent chapters to linear accelerators, cyclotrons, and synchrotrons.

It is most convenient to derive continuous differential equations for phase dynamics. We begin by showing that the synchronized accelerating fields in any accelerator can be written as a sum of traveling waves. Only one component (with phase velocity equal to the average particle velocity) interacts strongly with particles. Longitudinal motion is well described by including only the effects of this component. The derivation leads to a unified treatment of both discrete cavity and traveling wave accelerators.

The accelerator of Figure 13.4a has discrete resonant cavities oscillating at ω_o. The cavities drive narrow acceleration gaps. We assume that rf oscillations in the cavities have the same phase. Particles are synchronized to the oscillations by varying the distance between the gaps. The distance between gaps n and n+1 is

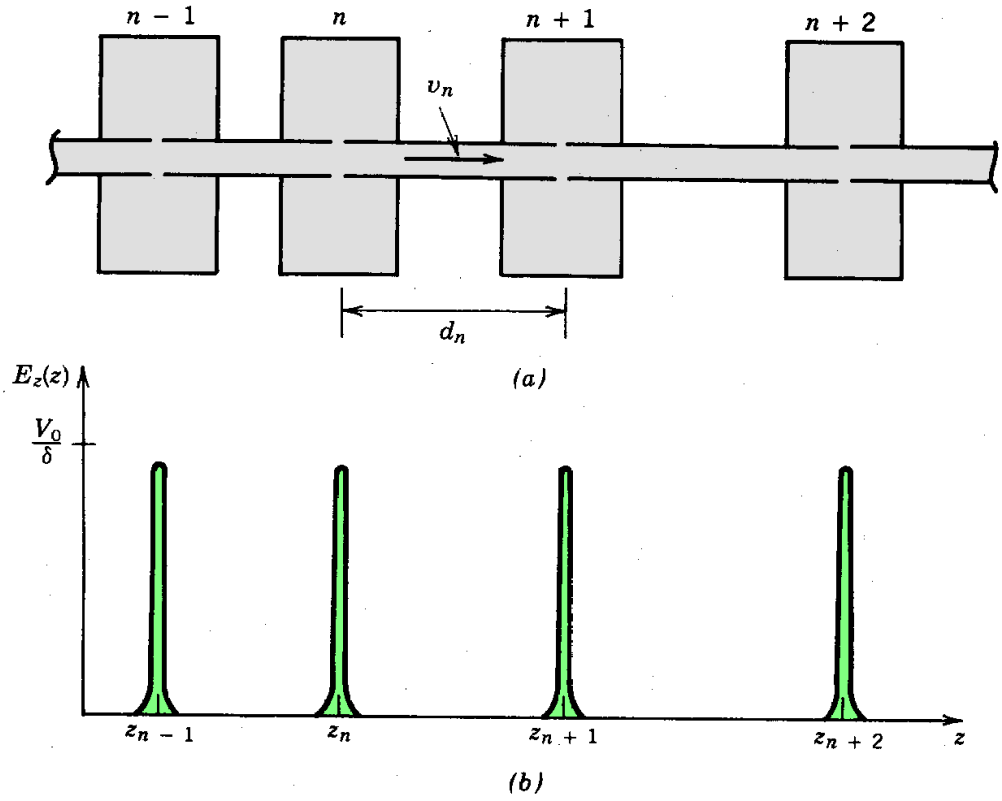

Figure 13.4 Resolution of synchronized gap voltages of standing wave accelerator into traveling wave components. (*a*) Array of uniform, phased cavities with varying intergap distances to preserve synchronization. (*b*) Variation of axial electric field as function of position at time of peak acceleration.

$$d_n = v_n\,(2\pi/\omega_o). \tag{13.6}$$

The quantity v_n is the average velocity of particles emerging from gap *n*. Equation (13.6) implies that the transit time of a synchronous particle between cavities is equal to one oscillation period. The distribution of longitudinal electric fields along the axis is plotted in Figure 13.4b. Assuming a peak voltage V_o, E_z can be approximated as a sum of δ functions,

$$E_z(z,t) \cong V_o \sin\omega_o t\,[\delta(z-z_1) + \delta(z-z_2) + \ldots + \delta(z-z_n) + \ldots\,]. \tag{13.7}$$

The electric field in a region of width d_n at gap *n* is represented by the Fourier expansion

$$E_z(z) = (2V_o/d_n)\sum_m \cos[m\pi(z-z_n)/d_n]. \tag{13.8}$$

Applying Eq. (13-6), the electric field distribution in the entire accelerator can be represented by a Fourier expansion of the delta functions,

$$E_z(z) = [V_o\omega_o/\pi v_z(z)] \sum_m \cos[mz\omega_o/v_z(z)], \tag{13.9}$$

where v(z) is a continuous function that equals v_n at d_n. Assuming a temporal variation $\sin\omega_o t$, axial electric field variations can be expressed as

$$\begin{aligned} E_z(z,t) &= [V_o\omega_o/\pi v_z(z)] \sum_m \sin\omega_o t \cos[mz\omega_o/v_z(z)] \\ &= [V_o\omega_o/2\pi v_z(z)] \sum_m \left(\sin[\omega_o t + mz\omega_o/v_z(z)] + \sin[\omega_o t - mz\omega_o/v_z(z)] \right) \end{aligned} \tag{13.10}$$

The gap fields are equivalent to a sum of traveling waves with axially varying phase velocity. The only component that has a long-term effect for particle acceleration is the positive-going component with $m = 1$. In subsequent discussions, the other wave components are neglected. The accelerating field of any resonant accelerator can be represented as

$$E_z(z,t) = E_o(z) \sin(\omega t - z\omega/v_s + \varphi_s). \tag{13.11}$$

The factor $E_o(z)$ represents a long-scale variation of electric field magnitude. In linear accelerators, ω is constant throughout the machine. In cycled circular accelerators such as the synchrocyclotron and synchrotron, ω varies slowly in time. The velocity v_s is the synchronous particle velocity as a function of position. The requirement for the existence of a synchronous particle is that v_s equals ω/k, the phase velocity of the slow wave. The motion of the synchronous particle is determined by Eq. (13.5).

Other particles shift position with respect to the synchronous particle; their phase, φ, varies in time. Orbits are characterized by φ rather than by axial position because the phase is almost constant during the acceleration process. In this section, we shall concentrate on a non-relativistic derivation since phase oscillations are most important in linear ion accelerators. Relativistic results are discussed in Section 13.6.

The longitudinal equation of motion for a nonsynchronous particle is

$$\frac{dp_z}{dt} = qE_o(z) \sin(\omega t - \omega z/v_s + \varphi_s) = qE_o(z) \sin\varphi(z). \tag{13/12}$$

The particle orbit is expanded about the synchronous particle in terms of the variables

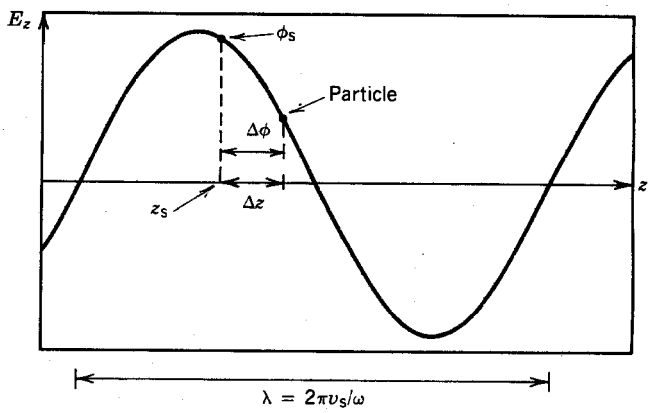

Figure 13.5 Relationship between position difference with respect to synchronous particle, $\Delta z = z - z_s$, and the phase difference, $\Delta\phi = \phi - \phi_s$.

$$z = z_s + \Delta z, \qquad (13.13)$$

$$v_z = dz/dt = v_s + \Delta v_z \qquad (13.14)$$

$$\varphi = \varphi_s + \Delta\varphi. \qquad (13.15)$$

where

$$\Delta\varphi = \omega t - \omega z/v_s.$$

Inspection of Figure 13.5 shows that the phase difference is related to the position difference by

$$\Delta\varphi/2\pi = -\Delta z/(2\pi v_s/\omega)$$

or

$$\Delta\varphi = -\omega\Delta z/v_s. \qquad (13.16)$$

Equations (13.12)-(13.16) can be combined to the forms

$$\varphi = \varphi_s - \omega\Delta z/v_s, \qquad (13.17)$$

$$d^2z_s/dt^2 + d^2\Delta z/dt^2 = (qE_o/m_o)\sin\varphi. \qquad (13.18)$$

Equations (13.17) and (13.18) relate φ to Δz; the relationship is influenced by the parameters of

the synchronous orbit. In Sections 13.3, 13.4, and 13.6, analytic approximations will allow the equations to be combined into a single phase equation.

13.3APPROXIMATE SOLUTION TO THE PHASE EQUATIONS

The phase equations for non-relativistic particles can be solved in the limit that the synchronous particle velocity is approximately constant over a phase oscillation period. Although the assumption is only marginally valid in linear ion accelerators, the treatment gives valuable physical insight into the phase equations.

With the assumption of constant v_s the second derivative of Eq. (13.17) is

$$d^2\varphi/dt^2 \cong -(\omega/v_s)\ d^2\Delta z/dt^2. \tag{13.19}$$

Furthermore, Eqs. (13.5) and (13.18) imply that

$$d^2\Delta z/dt^2 = (qE_o/m_o)\ \sin\varphi - d^2z_s/dt^2 = (qE_o/m_o)\ (\sin\varphi - \sin\varphi_s). \tag{13.20}$$

Equations (13.19) and (13.20) combine to

$$d^2\varphi/dt^2 = -(\omega qE_o/m_o v_s)\ (\sin\varphi - \sin\varphi_s). \tag{13.21}$$

Equation (13.21) is a familiar equation in physics; it describes the behavior of a nonlinear oscillator (such as a pendulum with large displacement). Consider, first, the limit of small oscillations ($\Delta\varphi/\varphi_s \ll 1$). The first sine term becomes

$$\sin\varphi = \sin(\varphi_s + \Delta\varphi) = \sin\varphi_s\ \cos\Delta\varphi + \cos\varphi_s\ \sin\Delta\varphi \cong \sin\varphi_s + \Delta\varphi\ \cos\varphi_s. \tag{13.22}$$

Equation (13.21) reduces to

$$d^2(\Delta\varphi)/dt^2 \cong -(\omega qE_o\cos\varphi_s/m_o v_s)\ \Delta\varphi. \tag{13.23}$$

The solution of Eq. (13.23) is

$$\Delta\varphi = \Delta\varphi_o\ \cos\omega_z t, \tag{13.24}$$

where ω_z is the phase oscillation frequency

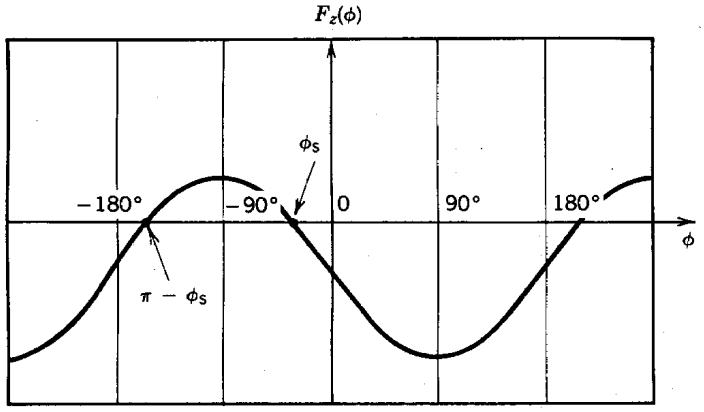

Figure 13.6 Effective force acting on nonsynchronous particles as function of particle phase. Example shows $\phi_s = 30°$.

$$\omega_z = \sqrt{qE_o\omega \cos\varphi_s / m_o v_s}. \tag{13.25}$$

Small-amplitude oscillations are harmonic; this is true for particles confined near a stable equilibrium point of any smoothly varying force.

In order to treat oscillations of arbitrary amplitude, observe that Eq. (13.21) has the form of a force equation. The effective force confines φ about φ_s. Figure 13.6 shows a plot of the effective restoring force $-(\omega qE_o m_o v_s)\ (\sin\varphi - \sin\varphi_s)$ as a function of φ. This expression is linear near φ_s; hence, the harmonic solution of Eq. (13.24). Particles which reach $\varphi > \pi - \varphi_s$ do not oscillate about φ_s. A first integral of Eq. (13.21) can be performed by first multiplying both sides by $2(d\varphi/dt)$:

$$(d\varphi/dt)^2 = (2\omega qE_o/m_o v_s)\ (\cos\varphi + \varphi \sin\varphi_s) + K. \tag{13.26}$$

We shall determine the integration constant K for the orbit of the oscillating particle with the maximum allowed displacement from φ_s. The orbit bounds the distribution of confined particles. Inspection of Figure 13.6 shows that the extreme orbit must have $(d\varphi/dt) = 0$ at $\varphi = \pi - \varphi_s$. Substituting into Eq. (13.26), the phase equation for the boundary orbit is

$$(d\varphi/dt)^2 = (2\omega qE_o/m_o v_s)\ [\cos\varphi + \cos\varphi_s + (\varphi + \varphi_s - \pi) \sin\varphi_s]. \tag{13.27}$$

The boundary particle oscillates about φ_s with maximum phase excursions given by the solution of

$$\cos\varphi + \cos\varphi_s = \sin\varphi_s\ (\pi - \varphi - \varphi_s). \tag{13.28}$$

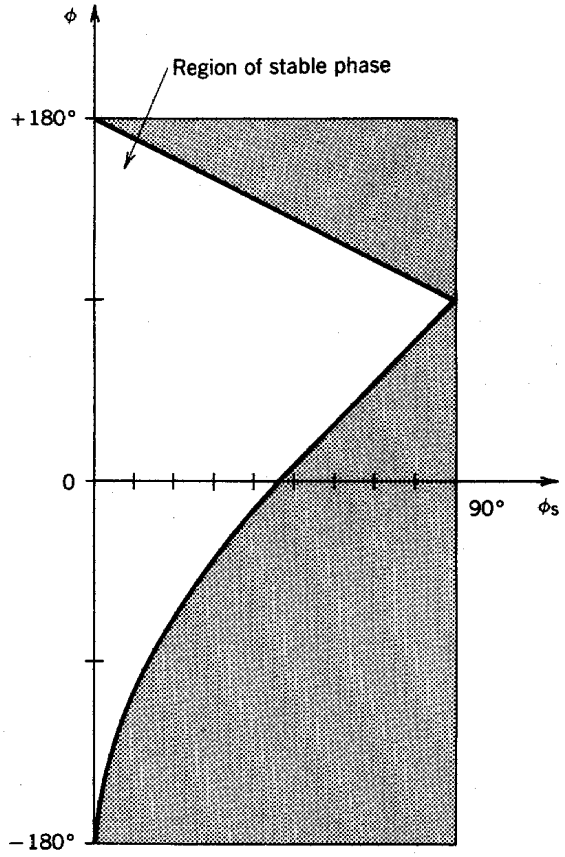

Figure 13.7 Range of stable phase as function of ϕ_s.

Figure 13.7 shows the limits of phase oscillations as a function of φ_s. The figure illustrates the trade-off between accelerating phase and longitudinal acceptance. A synchronous phase of 0° gives stable confinement of particles with a broad range of phase, but there is no acceleration. Although a choice of $\varphi_s = 90°$ gives the strongest acceleration, particles with the slightest variation from the synchronous particle are not captured by the accelerating wave. Figure 13.8 is a normalized longitudinal acceptance diagram in φ-($d\varphi/dt$) space as a function of φ_s derived from the orbit of the boundary particle. The acceptable range of longitudinal orbit parameters for trapped particles contracts as $\varphi_s \Rightarrow 90°$.

The principles of particle trapping in an accelerating wave and the limits of particle oscillations are well illustrated by a longitudinal potential diagram. Assume a traveling wave with an on-axis electric field given by $E_z(z,t) = E_o \sin(\omega t - \omega z/v_s)$. The electric field measured by an observer traveling at the non-relativistic velocity v_s is

$$E_z(\Delta z) = E_o \sin(\omega \Delta z/v_s) \tag{13.29}$$

if the origin of the moving frame is coincident with the point of zero phase and Δz is the distance

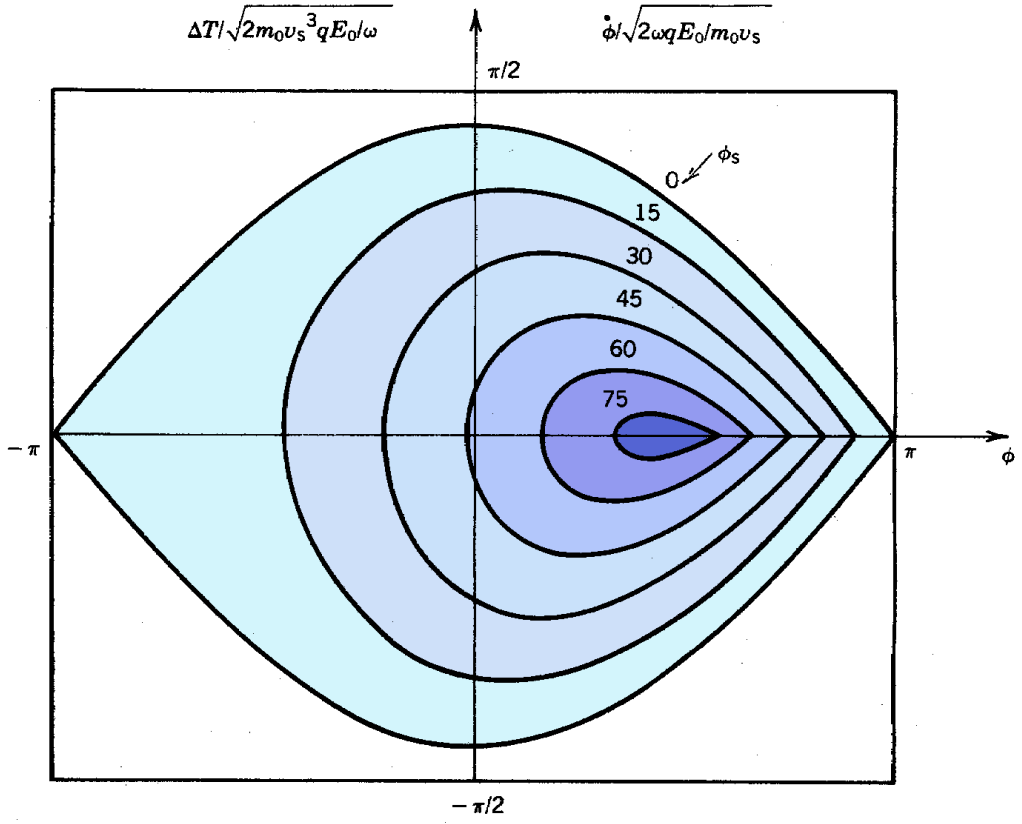

Figure 13.8 Longitudinal acceptance diagram (nonrelativistic motion); particle orbit parameters consistent with synchronized acceleration by a traveling wave as function of ϕ_s. Ordinate is either normalized rate of change of phase or normalized kinetic energy error. $\Delta T = T - T_s$ (kinetic energy), m_0 (particle rest mass), q (particle charge), v_s (synchronous particle velocity), E_0 (peak accelerating field), ω (rf angular frequency).

from the origin. Consider first a wave with constant velocity. In this case, $dv_s/dt = 0$ and Eq. (13.5) implies that $\varphi_s = 0°$. The moving observer determines the following longitudinal variation of potential energy (Fig. 13.9a):

$$U_s(\Delta z) = -\int d\Delta z\ qE_z(\Delta z) = (qE_o v_s/\omega)\ [1 - \cos(\omega \Delta z/v_s)], \tag{13.30}$$

corresponding to a potential well centered at $\Delta z = 0$. Particles are confined within a single half-cycle of the wave (an *rf bucket*) if they have a rest frame kinetic energy at $\Delta z = 0$ bounded by

$$m_o\ \Delta v_z^2 \le 2qE_o v_s/\omega = U_{e,\max}. \tag{13.31}$$

In order to accelerate particles, the phase velocity of a wave must increase with time. An observer

in the frame of an accelerating wave frame sees an addition force acting on particles. It is an inertial force in the negative *z* direction. Applying Eq. (13.5), the inertial force is

$$F_i = m_o\ (dv_s/dt) = qE_o\ \sin\varphi_s. \tag{13.32}$$

Integrating Eq. (13.32) from $\Delta z' = 0$ to Δz, the interial potential energy relative to the accelerating frame is

$$U_i = qE_o\ \sin\varphi_s\ \Delta z. \tag{13.33}$$

The total potential energy for particles in the wave frame (representing electric and inertial forces) is

$$U_t(\Delta z) = (qE_o v_s/\omega)\ [1 - \cos(\omega\Delta z/v_s)] + qE_o\ \sin\varphi_s\ \Delta z. \tag{13.34}$$

Figures 13.9b-e show U_t as a function of φ_s. The figure has the following physical interpretations:

1.The rf bucket is the region of the wave where particle containment is possible. The bucket region is shaded in the figures.

2.A particle with high relative kinetic energy will spill out of the bucket (Fig. 13.9c). In the wave frame, the desynchronized particle appears to move backward with acceleration $-dv_s/dt$ neglecting the small variations of velocity from interaction with the fields of subsequent buckets). In the stationary frame, the particle drifts forward with approximately the velocity it had at the time of desynchronization.

3.Increased wave acceleration is synonymous with larger φ_s. This leads to decreased bucket depth and width.

4.The acceleration limit occurs with $\varphi_s = 90°$. At this value, the bucket has zero depth. A wave with higher acceleration will outrun all particles.

5.The conditions for a synchronous particle are satisfied at φ_s and $\pi - \varphi_s$. The latter value is a point of unstable longitudinal equilibrium.

Equation (13.25) can be applied to derive a validity condition for the assumption of constant v_s over a phase oscillation. Equation (13.5) implies that the change in v_s in time Δt is $\Delta v_s \cong (qE_o \sin\varphi_s/m_o)\ \Delta t$. Taking $\Delta t = 2\pi/\omega_z$, we find that

$$\Delta v_s/v_s \cong 2\pi\ \sqrt{(qE_o/m_o v_s\omega)\ (\sin^2\varphi_s/\cos\varphi_s)}. \tag{13.35}$$

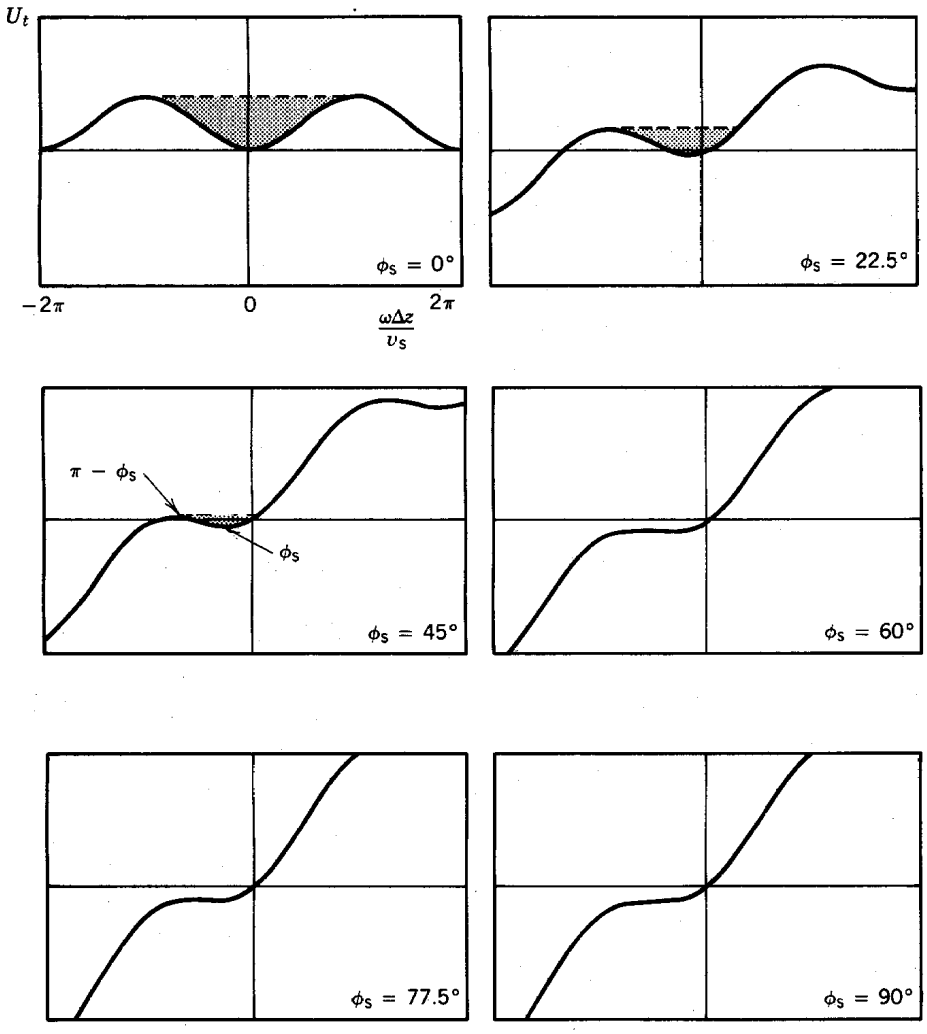

Figure 13.9 Longitudinal potential energy diagrams to illustrate phase stability. Potential energy of particle in accelerating traveling wave as function of ϕ for ϕ_s in the range of 0° to 90°.

As an example, assume 20-MeV protons ($v_s = 6.2 \times 10^7$ m/s), f = 800 MHz ($\omega = 5 \times 10^9$), $E_o = 2$ MV/m, and $\varphi_s = 70°$. These parameters imply that $\Delta v_s / v_s \cong 0.25$.

The longitudinal acceptance diagram is used to find limits on acceptable beam parameters for injection into an rf accelerator. In a typical injector, a steady-state beam is axially bunched by an acceleration gap oscillating at ω_o. The gap imparts a velocity dispersion to the beam. Faster particles overtake slower particles. If parameters are chosen correctly, the injected beam is localized to the regions of rf buckets at the accelerator entrance. Bunching involves a trade-off between spatial localization and kinetic energy spread. For injection applications, it is usually more convenient to plot a longitudinal acceptance diagram in terms of phase versus kinetic energy error. The difference in the kinetic energy of a non-relativistic particle from that of the synchronous particle is given by

$$\Delta T = \tfrac{1}{2} m_o \left[(dz_s/dt)+(d\Delta z/dt)\right]^2 - \tfrac{1}{2} m_o (dz_s/dt)^2 \cong m_o (dz_s/dt)(d\Delta z/dt).$$

Comparison with Eq. (13.16) shows that

$$\Delta T \cong (mv_s^2/\omega)(d\varphi/dt). \tag{13.36}$$

The dimensionless plot of Figure 13.8 also holds if the vertical axis is normalized to $\Delta T/\sqrt{2m_o v_s^3 qE_o/\omega}$.

13.4 COMPRESSION OF PHASE OSCILLATIONS

The theory of longitudinal phase dynamics can be applied to predict the pulselength and energy spread of particle bunches in rf buckets emerging from a resonant accelerator. This problem is of considerable practical importance. The output beam may be used for particle physics experiments or may be injected into another accelerator. In both cases, a knowledge of the micropulse structure and energy spread are essential.

In this section, we shall study the evolution of particle distributions in rf buckets as the synchronous velocity increases. In order to develop an analytic theory, attention will be limited to small phase oscillations in the linear region of restoring force. Again, the derivation is non-relativistic. Equation (13.16) implies that

$$\Delta z = -(v_s/\omega_o)\Delta\varphi. \tag{13.37}$$

The second derivative of Eq. (13.37) is

$$d^2\Delta z/dt^2 = -(1/\omega_o)\left[(dv_s/dt)(d\Delta\varphi/dt)+(d^2v_s/dt^2)\Delta\varphi+v_s(d^2\Delta\varphi/dt^2)+(dv_s/dt)(d\Delta\varphi/dt)\right] \tag{13.38}$$

Equation (13.20) can be rewritten

$$d^2\Delta z/dt^2 \cong (qE_o/m_o)\cos\varphi_s\,\Delta\varphi \tag{13.39}$$

in the limit that $\Delta\varphi \ll \varphi_s$. The mathematics is further simplified by taking $d^2v_s/dt^2=0$; the wave has constant acceleration. Setting the right-hand sides of Eqs. (13.38)and (13.39) equal gives

$$d^2\Delta\varphi/dt^2 + 2(dv_s/dt)(d\Delta\varphi/dt)/v_s + (\omega_o qE_o\cos\varphi_s/m_o v_s)\Delta\varphi = 0. \tag{13.40}$$

By the definition of the synchronous particle,

$$dv_s/dt = qE_o \sin\varphi_s/m_o. \tag{13.41}$$

This implies that

$$v_s = qE_o \sin\varphi_s t/m_o \tag{13.42}$$

if the origin of the time axis corresponds to $v_s = 0$. The quantity t is the duration of time that the particles are in the accelerator. Substituting Eqs. (13.41)and (13.42) into Eq. (13.40) gives

$$d^2\Delta\varphi/dt^2 + (2/t)\ (d\Delta\varphi/dt) + (\omega_o/\tan\varphi_s t)\ \Delta\varphi = 0. \tag{13.43}$$

Making the substitution $\Psi = \Delta\varphi t$, Eq. (13.43) can be written

$$d^2\Psi/dt^2 + \omega_z^2\ \Psi = 0, \tag{13.44}$$

where

$$\omega_z = \sqrt{\omega_o/\tan\varphi_s t}. \tag{13.45}$$

Equation (13.45) implies that Eq. (13.43) has an oscillatory acceleration solution for $0 < \varphi_s < \pi/2$. The condition for phase stability remains the same.

Equation (13.44) has the same form as Eq. (11.20), which describes the compression of betatron oscillations. Equation (13.44) is a harmonic oscillator equation with a slowly varying frequency. We apply the approximation that changes in the synchronous particle velocity take place slowly compared to the phase oscillation frequency, or $\omega_z T \gg 1$, where T is the time scale for acceleration. The linear phase oscillation frequency decreases as

$$\omega_z \sim 1/\sqrt{t} \sim 1/\sqrt{v_s}, \tag{13.46}$$

where Eq. (13.42) has been used to relate t and v_s. The quantity Ψ is the analogy of the amplitude of betatron oscillations. Equation (11-29) implies that the product $\Psi^2\omega_z$ is conserved in a reversible compression. Thus, the quantity Ψ increases as

$$\Psi \sim t^{1/4} \sim v_s^{1/4}. \tag{13.47}$$

Furthermore,

$$\Delta\varphi \sim \Psi/t \sim 1/t^{3/4} \sim 1/v_s^{3/4}. \quad (13.48)$$

In summary, the following changes take place in the distribution of particles in an rf bucket:

1. Particles injected with velocity v_i and micropulsewidth Δt_i emerge from a constant-frequency accelerator with velocity v_f and micropulsewidth

$$\Delta t_f = \Delta t_i \, (v_i/v_f)^{3/4}. \quad (13.49)$$

Although the spatial extent of the beam bunch is larger, the increase in velocity results in a reduced micropulsewidth.

2.Taking the derivative on the time scale of a phase oscillation, Eq. (13.48)implies that $d\Delta\varphi/dt \sim \omega_z/t^{3/4} \sim 1/t^{5/4} \sim 1/v_s^{5/4}$. Combining the above equation with Eq. (13.36) implies that the absolute kinetic energy spread of particles in an rf bucket increases as

$$\Delta T_f = \Delta T_i \, (v_f / v_i)^{3/4}. \quad (13.50)$$

Linear ion accelerators produce beams with a fairly large kinetic energy spread. If an application calls for a small energy spread, the particle pulses must be debunched after exiting the accelerator. The relative energy spread scales as

$$\Delta T_f/T_f = (\Delta T_i/T_i) \, (v_i/v_f)^{5/4}. \quad (13.51)$$

13.5 LONGITUDINAL DYNAMICS OF IONS IN A LINEAR INDUCTION ACCELERATOR

Although the linear induction accelerator is not a resonant accelerator, longitudinal motions of ions in induction linacs are discussed in this chapter because of the similarities to phase oscillations in rf linear ion accelerators. The treatment is limited to non-relativistic particles; electron accelerators are discussed in the next section.

The main problem associated with longitudinal dynamics in an induction accelerator is ensuring that ions are axially confined so that they cross acceleration gaps during the applied voltage pulses. A secondary concern is maintenance of a good current profile; this is important when beam loading of the pulse modulator is significant. In the following treatment, only single-particle

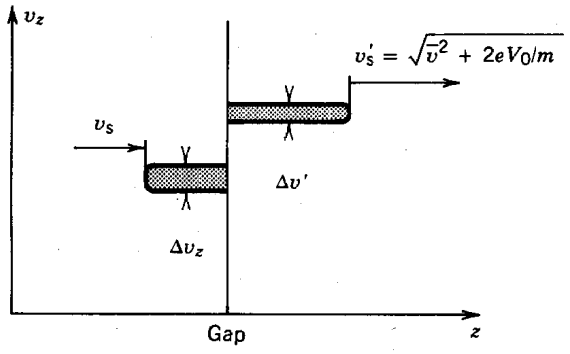

Figure 13.10 Modification of longitudinal beam distribution passing through constant-voltage acceleration gap.

effects are addressed. Cavity voltage waveforms are specified and beam loading is neglected.

To begin, consider a beam pulse of duration Δt_p moving through a gap with constant voltage V_o (Fig. 13.10). The incoming pulse has axial length l, longitudinal velocity v_s, and velocity spread Δv. The axial length is $l = v_s \Delta t_p$. Assume that the gap is narrow and the beam velocity spread is small ($\Delta v/v_s \ll 1$). The beam emerges with an increased velocity v_s'. Every particle entering the gap leaves it immediately, so that the pulselength is not changed. As shown in Figure 13.10, the beam length increases to

$$l' = l\ (v_s'/v_s). \tag{13.52}$$

The change in the velocity spread of the beam can be determined from conservation of energy for the highest-energy particles:

$$\tfrac{1}{2}m_o(v_s' + \tfrac{1}{2}\Delta v')^2 = \tfrac{1}{2}m_o(v_s + \tfrac{1}{2}\Delta v)^2 + qV_o \tag{13.53}$$

Keeping only the first-order terms of Eq. (13.53) and noting that $\tfrac{1}{2}m_o v_s'^2 = m_o v_s^2 + eV_o$, we find that

$$\Delta v' = \Delta v\ (v_s/v_s'). \tag{13.54}$$

The longitudinal velocity spread decreases with acceleration. As in any reversible process, the area occupied by the particle distribution in phase space (proportional to $l\Delta v$) remains constant. A flat voltage pulse gives no longitudinal confinement. The longitudinal velocity spread causes the beam to expand, as shown in Figure 13.11a. The expansion can be countered by adding a voltage ramp to the accelerating waveform (Fig. 13.11b). The accelerator is adjusted so that the synchronous particle in the middle of the beam bunch crosses the gap when the voltage equals V_o.

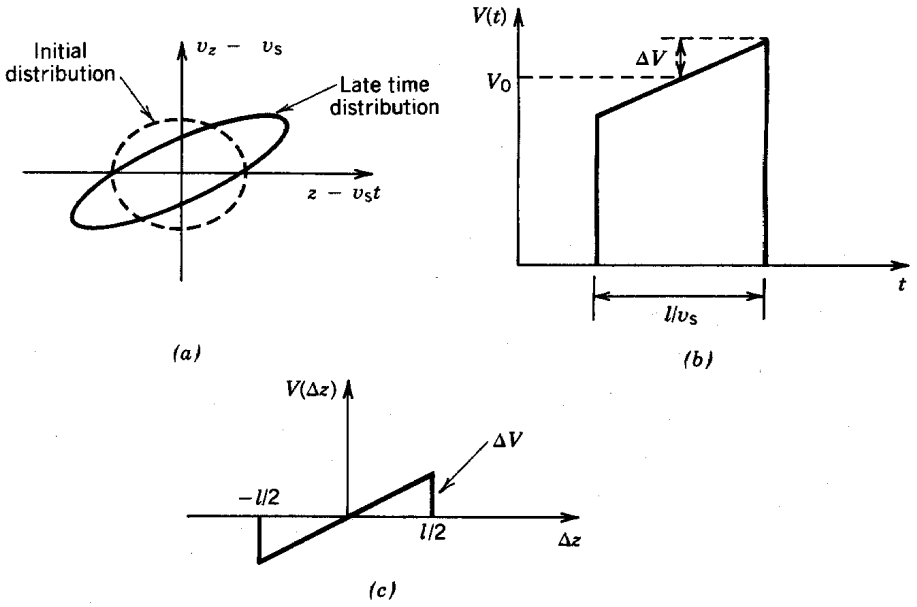

Figure 13.11 Longitudinal focusing of nonrelativistic beams in linear induction accelerators. (*a*) Spatial expansion of beam with spread in longitudinal velocity. (*b*) Accelerating voltage waveform with linear ramp. (*c*) Alternating-current portion of ramped accelerating voltage.

Particles lagging behind the synchronous particle experience a higher gap voltage and gain a larger velocity increment while advanced particles are retarded. This not only confines particles within the bunch but also provides stability for the entire beam pulse. For example, if the voltage in an upstream cavity is low, the centroid of the bunch arrives late in subsequent cavities. With ramped voltage waveforms, the bunch receives extra acceleration and oscillates about the synchronous particle position.

A simple model for beam confinement in an induction linear accelerator can be developed in the limit that (1) the beam crosses many gaps during a phase oscillation and (2) the change in v_s is small during a phase oscillation. Let the quantity Δz be the distance of a particle from the snchronous particle position, or

$$\Delta z = z - v_s t. \tag{13.55}$$

The quantity Δv is the width of the longitudinal velocity distribution at $\Delta z = 0$.

The dc part of the cavity voltage waveform can be neglected because of the assumption of constant v_s over time scales of interest. The time-varying part of the gap voltage has the waveform of Figure 13.11c. The gap voltage that accelerates a particle depends on the position of the particle relative to the synchronous particle:

$$\Delta V = -(2\Delta z/l)\ \Delta V_o, \tag{13.56}$$

where ΔV_o is defined in Figure 13.11c. The velocity changes by the amount

$$\Delta v \cong (q/m_o v_s)\ (-2\Delta z/l)\ \Delta V_o \tag{13.57}$$

crossing a gap. Equation (13.57) holds in the limit that $\Delta v \ll v_s$. Particles cross $N = v_s \Delta t/D$ gaps in time interval Δt if the gaps have uniform spacing D. Therefore, multiplying Eq. (13.57) by N gives the total change of Δv in Δt. The longitudinal equation of motion for ion in an induction linear accelerator is

$$d\Delta v/dt = d^2\Delta z/dt^2 \cong -(2q\Delta V_o/m_o lD)\ \Delta z. \tag{13.58}$$

Equation (13.58) has solution

$$\Delta z = \Delta z_o \sin\omega_z t, \tag{13.59}$$

where

$$\omega_z = \sqrt{2q\Delta V_o/m_o lD}. \tag{13.60}$$

The maximum value of Δv is determined from Eq. (13.59) by substituting $\Delta z_o = l/2$:

$$\Delta v \le \sqrt{(q\Delta V_o/2m_o)\ (l/D)}. \tag{13.61}$$

Equation (13.61) infers the allowed spread in kinetic energy,

$$\Delta T/T \cong \sqrt{(2q\Delta V_o/m_o)\ (l/D)}\ /\ v_s. \tag{13.62}$$

The longitudinal dynamics of ions in an induction linear accelerator is almost identical to the small $\Delta\varphi$ treatment of phase oscillations in an rf accelerator. The time-varying gap electric field in Figure 13.11 can be viewed as an approximation to a sine function expanded about the synchronous particle position. The main difference between the two types of accelerators is in the variation of phase oscillation frequency and velocity spread during beam acceleration. The electric field ramp in an rf linear accelerator is constrained by the condition of constant frequency. The wavelength increases as v_s, and hence the longitudinal confining electric field in the beam rest frame decreases as $1/v_s$. This accounts for the decrease in the phase oscillation frequency of Eq. (13.46). In the induction accelerator, there is the latitude to adjust the longitudinal confinement gradient along the accelerator.

Equation (13.61) implies that the longitudinal acceptance is increased by higher voltage ramp (ΔV_o) and long beam length compared to the distance between gaps (l/D). If v_s varies slowly, Eq.

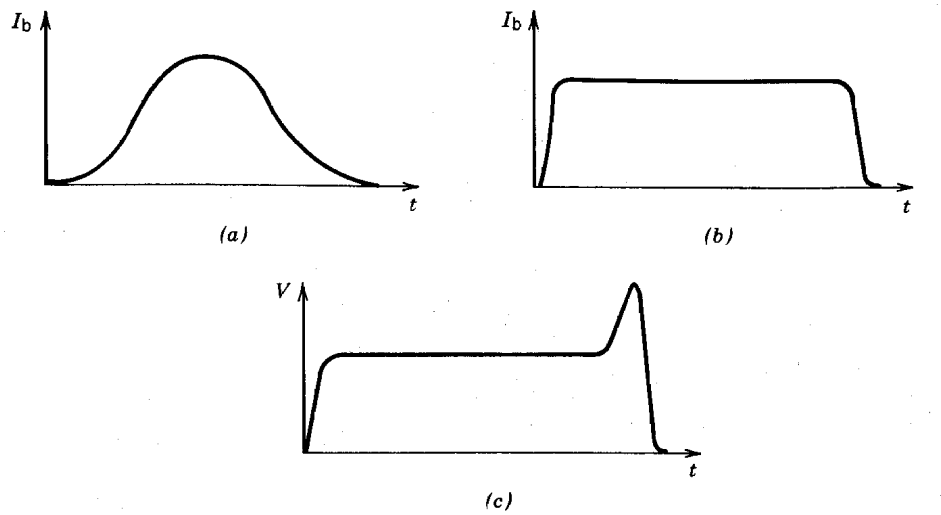

Figure 13.12 Longitudinal dynamics of nonrelativistic beams in linear induction accelerators. (*a*) Typical current profile of beam contained by accelerating voltage with linear ramp. (*b*) Desirable current profile for load matching to pulse modulator. (*c*) Voltage waveform with nonlinear variations to contain beam with flat current profile.

(13.61) implies that the magnitude of ΔV_0 must be reduced along the length of the accelerator to maintain a constant beam pulselength. Constant pulselength implies that $l \sim v_s$ and $\Delta v \sim 1/v_s$; therefore, ΔV_0 must be reduced proportional to $1/v_s^3$ for constant D. On the other hand, if ΔV_0 is constant throughout the accelerator, l and Δv are constant. This means that the pulselength, or the time for the beam bunch to pass through the gap, decreases as $1/v_s$.

The longitudinal shape of the beam bunch is not important when beam loading is negligible. Particles with a randomized velocity distribution acted on by linear forces normally have a bell-shaped density distribution; in this case, the beam current profile associated with a pulse looks like that of Figure 13.12a. When beam loading is significant, it is preferable to have a flat current pulse, like that of Figure 13.12b. This can be accomplished by nonlinear longitudinal confinement forces; a confining cavity voltage waveform consistent with the flat current profile is illustrated in Figure 13.12c. The design of circuits to generate nonlinear waveforms for beam confinement under varying load conditions is one of the major unanswered questions concerning the feasibility of linear induction ion accelerators.

13.6 PHASE DYNAMICS OF RELATIVISTIC PARTICLES

Straightforward analytic solutions for longitudinal dynamics in rf linear accelerators are possible for highly relativistic particles. The basis of the approach is to take the phase velocity of the accelerating wave exactly equal to c, and to seek solutions in which electrons are captured in the accelerating phase of the wave. In this situation, there is no synchronous phase because the

particles (with $v_z < c$) always move to regions of higher phase in the accelerating wave. We shall first derive the mathematics of electron capture and then consider the physical implications.

Assume electrons are injected into a traveling wave at $z = 0$. The quantity φ_o is the particle phase relative to the wave at the injection point. Equation (13.17) can be rewritten

$$\varphi = \varphi_o - \omega\Delta z/c, \tag{13.63}$$

where

$$\Delta z = z - ct. \tag{13.64}$$

The quantity z is the position of the electron after time t, and ct is the distance that the wave travels. Thus, Δz is the distance the electron falls back in the wave during acceleration. Clearly, Δz must be less than $\lambda/2$ or else the electron will enter the decelerating phase of the wave. Equation (13.63) can also be written

$$\varphi = \varphi_o + \omega\ (t - z/c). \tag{13.65}$$

The derivative of Eq. (13.65) is

$$d\varphi/dt = \omega\ (1 - z/c) = \omega\ (1 - \beta). \tag{13.66}$$

The relativistic form of Eq. (13.12) for electrons is

$$dp_z/dt = d(\gamma m_e \beta c)/dt = d[m_e \beta c/\sqrt{1-\beta^2}]/dt = eE_o \sin\varphi. \tag{13.67}$$

Equations (13.66) and (13.67) are two equations in the the unknowns φ and β. They can be solved by making the substitution

$$\beta = \cos\alpha. \tag{13.68}$$

Equation (13.67) becomes

$$d(\cos\alpha/\sin\alpha)/dt = (eE_o/m_e c)\ \sin\varphi = -(d\alpha/dt)\ (1+\cos^2\alpha/\sin^2\alpha). \tag{13.69}$$

Manipulation of the trigonometric functions yields

$$d\alpha/dt = -\ (eE_o/m_e c)\ \sin\varphi\ \sin^2\alpha. \tag{13.70}$$

Equation (13.66) is rewritten

$$d\varphi/dt = (d\varphi/d\alpha)\ (d\alpha/dt) = \omega\ (1-\cos\alpha). \tag{13.71}$$

Substituting Eq. (13.71) into Eq. (13.70) gives the desired equation,

$$-\sin\varphi\ d\varphi = (m_e c\omega/eE_o)\ (1 - \cos\alpha)\ d\alpha/\sin^2\alpha. \tag{13.72}$$

Integrating Eq. (13.72) with the lower limit given by the injection parameters, we find that

$$\cos\varphi - \cos\varphi_o = (m_e c\omega/eE_o)\ [\tan(\tfrac{1}{2}\alpha) - \tan(\tfrac{1}{2}\alpha_o)]. \tag{13.73}$$

Noting that $\tan(\tfrac{1}{2}\alpha) = \sqrt{(1-\cos\alpha)/(1+\cos\alpha)} = \sqrt{(1-\beta)/(1+\beta)}$, the electron phase relative to the accelerating wave is given in terms of β by

$$\cos\varphi - \cos\varphi_o = (m_e c\omega/eE_o)\left[\ \sqrt{(1-\beta)/(1+\beta)} - \sqrt{(1-\beta_o)/(1+\beta_o)}\ \right]. \tag{13.74}$$

The solution is not oscillatory; φ increases monotonically as β changes from β_o to 1 and the particle lags behind the wave. Acceleration takes place as long as the particle phase is less than $\varphi = 180°$. Note that since there are no phase oscillations, there is no reason to restrict the particle phase to $\varphi < 90°$. The important point to realize is that if acceleration takes place fast enough, electrons can be trapped in a single rf bucket and accelerated to arbitrarily high energy. With high enough E_o, the electrons never reach phase $\varphi = 180°$. This process is called *electron capture*. In this regime, time dilation dominates so that the particle asymptotically approaches a constant phase, φ.

The condition for electron capture can be derived from Eq. (13.74) by assuming that the final particle β is close to unity:

$$\cos\varphi - \cos\varphi_o = (m_e c\omega/eE_o)\ \sqrt{(1-\beta_o)/(1+\beta_o)} \le 1. \tag{13.75}$$

The limit proceeds from the fact that φ should approach 90° for optimum acceleration and φ_o must be greater than 0°. Equation (13.75) implies that

$$E_o > (m_e c\omega/e)\ \sqrt{(1-\beta_o)/(1+\beta_o)}. \tag{13.76}$$

As an example, consider injection of 1 MeV electrons into a traveling wave accelerator based on a 2 GHz ($\omega = 1.26 \times 10^{10}\ s^{-1}$) iris-loaded waveguide. The quantity β_o equals 0.9411. According to Eq. (13.76), the peak electric field of the wave must exceed 3.7 MV/m. This is a high but feasible

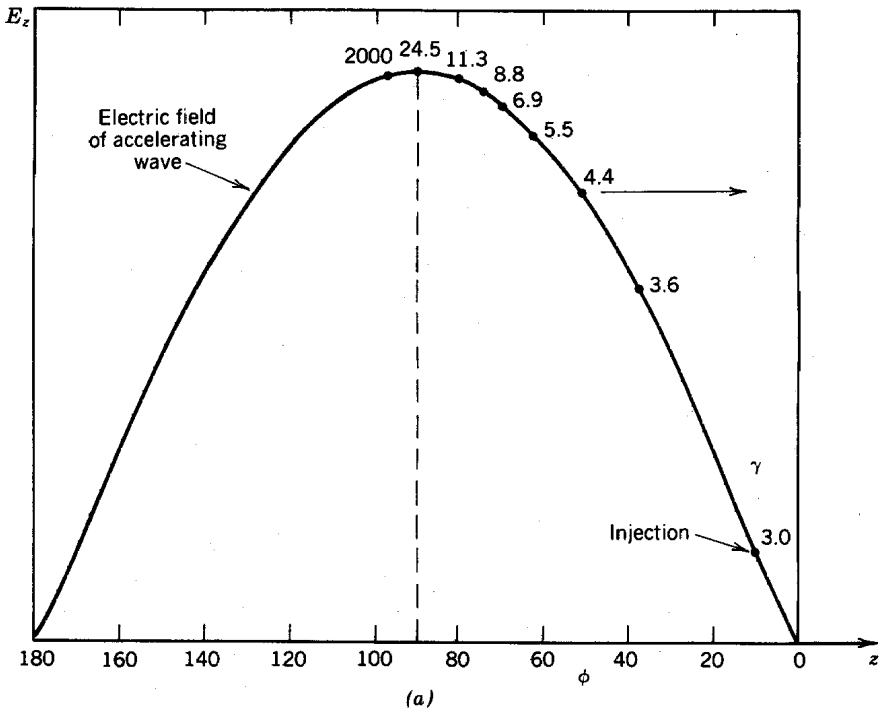

Figure 13.13 Electron acceleration in high-gradient linear accelerator, $f = 3$ GHz, $E_0 = 5$ MV/m. (*a*) Electron phase and relative accelerating field versus γ. (*b*) Kinetic energy versus ϕ.

value.

The dynamics of relativistic electron capture is illustrated in Figure 13.13. Figure 13.13a shows the relative position of electrons in the accelerating wave as a function of energy in a 1 GeV accelerator. Figure 13.13b graphs energy versus phase. Note that most of the acceleration takes place near the final asymptotic value of phase, φ_f. The output beam energy is

$$T \cong E_o \sin\varphi_f L, \tag{13.77}$$

where L is the total length of the accelerator. A choice of $\varphi_f = 90°$ gives the highest accelerating gradient.

In the beam rest frame, the accelerator appears to be moving close to the speed of light. The length of the accelerator is shortened by Lorentz contraction. It is informative to calculate the apparent accelerator length in the beam frame. Let dz be an element of axial length in the accelerator frame and dz' be the length of the element measured in the beam frame. According to Equation (2.24), the length elements are related by $dz' = dz/\gamma$, or

$$dz' = (m_e c^2/E)\, dz, \tag{13.78}$$

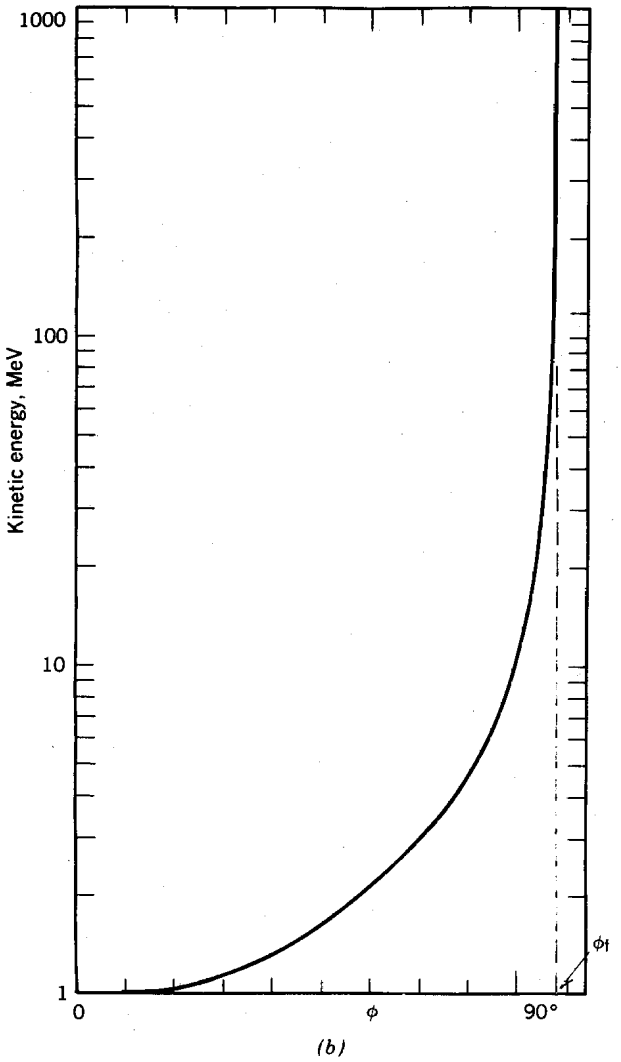

(b)

Figure 13.13 (*Continued*).

where E is the total energy of the electrons. We have seen that the accelerating gradient is almost constant for electrons captured in the rf waveform. The total energy is approximated by

$$E \cong m_e c^2 + T_o + eE_o \sin\varphi_f \, z. \tag{13.79}$$

Combining Eqs. (13.78) and (13.79),

$$dz' = dz/(1 + T_o/m_e c^2 + eE_o \sin\varphi_f \, z/m_e c^2). \tag{13.80}$$

Integrating Eq. (13.80) from $z = 0$ to $z = L$ gives

$$L' = (m_e c^2/eE_o \sin\varphi_f)\ \ln\left[(1 + T_o/m_e c^2 + eE_o \sin\varphi_f L/m_e c^2)/(1 + T_o/m_e c^2)\right]$$
$$= L\ (m_e c^2/T_f)\ \ln(E_f/E_i). \tag{13.81}$$

As an example, consider electron motion with the acceleration history illustrated in Figure 13.13. The peak accelerating field is 5 MV/m, f = 3 GHz, and electrons are injected with kinetic energy 1 MeV. The final phase is near 90° for particles with injection phase angles near 0°. These particles are accelerated mainly at the peak field; the accelerator must have a length L = 200 m to generate a 1 GeV beam. Substituting in Eq. (13.81), the apparent accelerator length in the beam frame is only 0.7 m.

Equation (13.81) can also be applied to induction linear electron accelerators if the quantity $E_o \sin\varphi_f$ is replaced by the average accelerating gradient of the machine. Consider, for instance, an induction accelerator with a 50 MeV output beam energy. The injection energy is usually high in such machines; 2.5 MeV is typical. Gradients are lower than rf accelerators because of limits on isolation core packing and breakdown on vacuum insulators in the cavity. An average gradient of 1 MV/m implies a total length L = 50 m. Substituting into Eq. (13.81), the apparent length is L' = 1.5 m.

The short effective length explains the absence of phase oscillations in relativistic rf linacs. As viewed in the beam frame, the accelerator is passed before there is time for any relative longitudinal motion. The short effective length has an important implication for the design of low-current linear accelerators. The accelerator appears so short that it is unnecessary to add transverse focusing elements for beam confinement; the beam is simply aimed straight through. Radial defocusing of particles (see Chapter 14) is reduced greatly at high γ.

Induction linear electron accelerators are used for high-current pulsed beams. Transverse focusing is required in these machines to prevent space charge expansion of the beam and to reduce the severity of resonant transverse instabilities. Nonetheless, space charge effects and the growth of instabilities are reduced when electrons have high γ. In particular, the radial force from beam space charge decreases as $1/\gamma^2$. This is the main reason that the injector of an electron linear accelerator is designed to operate at high voltage.

We have seen in Section 13.5 that cavity voltage waveforms have a strong effect on the current pulse shape in an induction accelerator for ions. To demonstrate that this is not true for relativistic particles, consider an electron beam in an accelerator with average energy $\gamma m_e c^2$. Assume that there is a spread of energy parametrized by $\pm\Delta\gamma$ resulting from variations in cavity voltage waveforms. We shall demonstrate the effect of energy spread by determining how far a beam pulse travels before there is a significant increase in pulselength. The beam bunch length in the accelerator frame is denoted as L. The total spread in axial velocity is

$$\Delta v_z \cong c\beta^+ - c\beta^-, \tag{13.82}$$

where

$$\beta^{+} = \sqrt{1 - 1/(\gamma+\Delta\gamma)^2}, \tag{13.83}$$

and

$$\beta^{-} = \sqrt{1 - 1/(\gamma-\Delta\gamma)^2}, \tag{13.84}$$

Applying the binomial theorem, the axial velocity spread is

$$\Delta v_z = 2c\ (\Delta\gamma/\gamma^3). \tag{13.85}$$

Let Δt be the time it takes for the beam to double its length:

$$\Delta t \cong (L/2)/(\Delta v_z/2) = (L/c)\ (\gamma^3/\Delta\gamma). \tag{13.86}$$

The beam travels a distance $D = c\Delta t$ during this time interval. Substituting from Eq. (13.85), we find that

$$D \cong \gamma^2 L/(\Delta\gamma/\gamma). \tag{13.87}$$

As an example, consider a 50-ns pulse of 10-MeV electrons with large energy spread, $\Delta\gamma/\gamma = 0.5$. The beam pulse is 15 m long. Equation (13.87) implies that the distance traveled during expansion is 12 km, much longer than any existing or proposed induction accelerator. The implication is that electron beam pulses can be propagated through and synchronized with an induction accelerator even with very poor voltage waveforms. On the other hand, voltage shaping is important if the output beam must have a small energy spread.